Title
Enhancing Paper-Based Diagnostics through Quantitative Experimentation, Modeling, and Design

Author
Mosley, Garrett

Publication Date
2016

Peer reviewed|Thesis/dissertation

UNIVERSITY OF CALIFORNIA

Los Angeles

Enhancing Paper-Based Diagnostics through Quantitative Experimentation, Modeling, and Design

A dissertation submitted in partial satisfaction of the requirements for the degree Doctor of Philosophy in Bioengineering

by

Garrett Lee Mosley

2016

ABSTRACT OF THE DISSERTATION

Enhancing Paper-Based Diagnostics through

Quantitative Experimentation, Modeling, and Design

by

Garrett Lee Mosley

Doctor of Philosophy in Bioengineering

University of California, Los Angeles, 2016

Professor Daniel T. Kamei, Chair

Infectious diseases are a significant problem, accounting for 1 in every 4 deaths worldwide. The field of bioengineering is constantly innovating and advancing diagnostic technology; however, more often than not, these innovations are accessible only to communities with privileged resources. This has led to a growing focus on point-of-care (POC) diagnostics. Due to their ease of use, speed, and low cost, POC diagnostics can effectively test patients in resource-poor settings. One of the most well known POC technologies is the lateral-flow immunoassay (LFA). Most easily recognized for its use in pregnancy tests, LFA is a paper-based diagnostic that produces visually interpreted results using a colorimetric indicator decorated with antibodies specific to the target. Recently, we

have seen rapid advancement in the fields of paper fluidics and paper diagnostics, which can have a tremendous impact on the future of LFA technology. In light of this, we focused our work in 3 distinct directions, which involves development of quantitative experimental methodologies, mathematical modeling, and improving the ease-of-use of the advanced LFA technology.

Development of new paper-based devices would benefit significantly from being able to quantitatively assess the effects of engineering the device on important LFA parameters. For example, it would be useful to know the effects of manipulating the gold nanoprobes and test strips on the forward ($k_{f,s}$) and reverse ($k_{r,s}$) rate constants for the probe binding to and dissociating from the test line, respectively. We discuss our novel approach for determining these rate constants and the volumetric flow rate by using mathematical modeling and radioactive iodine-125 (^{125}I). Moreover, we demonstrate how radioactivity and paper strips can also be used to determine the volume of fluid in and before the test line, the concentration of gold nanoprobes, and the number of antibodies per gold nanoprobe.

As the field of paper-based diagnostics continues to rapidly expand, it becomes more important to incorporate modeling into their design. A model can be used to determine the effects of LFA parameters on desired outputs, such as the amount of probe bound to the test line. Such predictions become increasingly important as systems become more complicated, and the effects of changing different operating conditions become less intuitive due to the many physical, chemical, and biological processes that are simultaneously occurring. Moreover, a mathematical model allows the engineer to quantitatively predict the influence of well-defined changes in certain parameters. We have

derived a simple model that could be used in combination with our novel estimation methods for LFA parameters to predict the amount of probe binding to the test line, an important performance indicator of LFA. We will discuss the derivation of the model, and demonstrate the model's ability to predict empirical results.

Our lab's recent innovations have improved LFA sensitivity by utilizing aqueous two-phase systems (ATPSs) to thermodynamically concentrate the target molecule prior to detection. In the third direction, we describe a diagnostic design that dehydrates the ATPS components within the paper, creating a non-dilutive, one-step diagnostic process. We investigate the importance of ATPS component dehydration order and demonstrate an improvement in the limit of detection for *Chlamydia trachomatis* LFA using our dehydrated ATPS diagnostic design.

The dissertation of Garrett Lee Mosley is approved.

Dean Ho

Wenyuan Shi

Benjamin M. Wu

Daniel T. Kamei, Committee Chair

University of California, Los Angeles

2016

This work is dedicated to my family and friends, who have always shown me unconditional love and support.

Table of Contents

ACKNOWLEDGMENTS

The past 6 years have been an incredible journey during which I have experienced tremendous personal growth and development throughout the trials and tribulations of graduate school. However, this would not have been possible without the many individuals who gave me their support and guidance along the way.

The first step on my path towards earning my PhD was getting through the first quarter of classes and passing my comprehensive and preliminary exams. While all the classes were challenging, one in particular, Dr. Kamei's 201, was particularly challenging for me considering that my educational background in mathematics was not sufficient to prepare me for the course material. However, I was determined to pass the class because I wanted to join Dr. Kamei's lab, as well as wanted to prove to myself that I belonged in an engineering PhD program. This required a tremendous amount time and effort on my part, however, it is doubtful that I would have made it through if it weren't for the support that I had from the members of the study group that I was a part of. I had quickly made friends with Brian, Mark, and Walter, and throughout those first few months of graduate school, we spent nearly every single day together. Each one of them would take the time to explain solutions and concepts, which was not an easy task considering how foreign the class material was to me. I am very grateful for all of their help, and believe that I may have not made it this far if it wasn't for their support.

Throughout my early years in the Kamei lab, I received a lot of training on various lab techniques by the older graduate students. Ricky showed me a majority of the LFA techniques which I used for most of my thesis. Ricky is incredibly intelligent and very good

at conveying the concepts behind each technique, rather than just going through the protocol steps. Ricky also played a large role in helping me become well balanced in the way I run experiments. I had a tendency to obsess over details which would result in slow progress. While this approach is useful at times, he showed me that other times you just need to get into the lab and run things, and that random exploratory experiments can sometimes result in new and interesting findings. My other graduate student mentor was Dennis, who initially trained me when I first entered the lab. Dennis was very much on the opposite end of the spectrum of Ricky with respect to my lab technique training. Dennis was extremely detailed and rigorous in his methods. This helped me become very detailed oriented and rigorous early on in my PhD. Even though he mostly taught me drug delivery research techniques, which did not end up in my thesis, his process and approach to experimental design and protocols has always stuck with me. I am very grateful to both Ricky and Dennis for providing me with different toolsets and approaches to research and experimental design.

Throughout these past years in the Kamei lab, I have become very close with all of the Kamei lab graduate students. Foad, Dennis, Mike, Ricky, Tracy, Kristine, David, Sherine, Brad, and Andre have all made my graduate school experience very memorable. Whenever I hear from graduate students in other labs about the drama and issues that they deal with, it always reminds me how lucky I am to be part of a lab where the students share such strong bonds with each other. If one of us ever needed help, whether it was for something small like covering an office hour or something big like a family emergency, we would always rally to help the person in need. Everyone was there for each other, and it always felt more like a big family than a typical lab environment.

Typical of most research projects, the ones that I worked on were difficult and had many issues that needed resolving in the process of collecting data. Throughout this process I had a tremendous amount of invaluable help from some of the undergraduate students within our lab. My early work on oral drug delivery for the treatment of inflammatory bowel disease unfortunately did not make it into my thesis work, but I am still very grateful for all the help from Sam and Kevin while we were working on that project. It required a lot of effort and working odd hours, but they always remained optimistic and put their best efforts into their work. For my work on diagnostics, I had help from Amy, Phuong, Eumene, and Vincent. Amy in particular had helped me throughout most of the ARROW project, and spent a lot of time and effort with me in seeing it become successful. I am very grateful to all of the undergrads who have helped, and I feel that they have become very strong and independent researchers.

I would like to thank all of my friends for their support over the years, whether it was for graduate school or otherwise. They are, without a doubt, the most eclectic and goofiest 'band of brothers', but also the most loyal friends that I could have ever hoped to have.

I am very thankful that I was able to go through a majority of graduate school with Cynthia by my side. We endured the ups and downs of the PhD life together, and were always there to support one another when things got tough. I am also very thankful of her understanding during the year after she graduated and I was finishing up my work. Late nights and weekends in the lab didn't leave much time for talking or any time for visiting her up in San Francisco, however she never complained and always was accommodating

of my situation, and gave me the support I needed to get through the last stretch of my PhD work.

Of course, I am very thankful for the love and support that my family has always shown me. My younger brother Connor and I have always been a ‘dynamic duo’, and have been on many adventures together. My older sister Jami has always been my ‘protector’ ever since I was young, whether it was protecting me from my adventurous self or from getting in trouble. My step-mom Lauri, has always shown me support no matter how aggravating I may have been at times. Lastly, I am very thankful for my parents, and for the values they instilled in me. Getting through graduate school required substantial work ethic and determination, and I believe that came from having my parents as role models to look up to my whole life. They also fostered my creativity and my relentless curiosity ever since I was young. Both of those traits are what led me to go into research and science, and I have them to thank for how far I have come.

Lastly, I am very grateful for my mentor Dr. Daniel Kamei. The past 6 years have been about much more than just earning a degree and publishing research. They have been about growing and developing professional skills that will help me regardless of my future career, and I have Dr. Kamei to thank for how far I have progressed since entering the Bioengineering program at UCLA. There is no one more devoted to mentoring and emotionally invested in the development of their mentees than Dr. Kamei. He has helped me become the best possible researcher and scientist that I can be, and words cannot adequately express my gratitude for all that he has done.

Work performed in Chapters 2 and 3 were supported by a grant from the UCLA School of Dentistry.

Work performed in Chapter 4 was supported by a grant from the UCLA School of Dentistry, and by the National Institutes of Health under Small Business Innovation Research award number 20152317.

VITA

2010	B.A., Biochemistry California Lutheran University Thousand Oaks, California
2010	B.S., Psychology California Lutheran University Thousand Oaks, California
2011-2015	Teaching Assistant Department of Bioengineering University of California Los Angeles, California
2014	M.S., Bioengineering University of California, Los Angeles Los Angeles, California

PUBLICATIONS AND PRESENTATIONS

G. L. Mosley, P. Nguyen, B. M. Wu, and D. T. Kamei, "Development of Quantitative Radioactive Methodologies on Paper to Determine Important Lateral-Flow Immunoassay Parameters", In Revision.

G. L. Mosley, S. K. L. Cheng, and D. T. Kamei, "Developing a Targeted Oral Drug Carrier Using a Layer-by-Layer Chitosan and Alginate Enteric Coating", BMES Annual Meeting, **Oct 2014**.

G. L. Mosley, S. K. L. Cheng, and D. T. Kamei, "Demonstrating Compatibility of a Chitosan-Alginate Enteric Coating for Targeted Oral Drug Delivery of Nanoparticles", 15th Annual UC Systemwide Bioengineering Symposium, **June 2014**.

G. L. Mosley, S. K. L. Cheng, D. S. Quinlan, C. T. Liu, P. M. Nafisi, D. Das, G. Fang, and D. T. Kamei, "Protection of Colonic Disease Therapeutics During Transit Through the Gastrointestinal Tract", UCLA Engineering – 2014 Tech Forum, **Feb 2014**.

G. L. Mosley, S. K. L. Cheng, D. S. Quinlan, C. T. Liu, P. M. Nafisi, D. Das, G. Fang, and D. T. Kamei, "Layer-by-layer Chitosan-alginate Coating of Polymeric

Nanoparticles for Colon Specific Drug Delivery", Society for Laboratory Automation and Screening 3rd Annual Conference and Exhibition, **Jan 2014**.

G. L. Mosley, C. D. Yamanishi, and D. T. Kamei, "Mathematical Modeling of Vesicle Drug Delivery Systems I: Vesicle Formation and Stability Along with Drug Loading and Release", *Journal of Laboratory Automation*, **2013**, 18(1), 34-45.

G. L. Mosley, S. K. L. Cheng, D. S. Quinlan, C. T. Liu, P. M. Nafisi, D. Das, G. Fang, and D. T. Kamei, "Coating Polymeric Nanoparticles with Chitosan-Alginate as an Enteric Coating for Colon Specific Drug Delivery", BMES Annual Meeting, **Sept 2013**.

G. L. Mosley, S. K. L. Cheng, D. S. Quinlan, C. T. Liu, P. M. Nafisi, D. Das, G. Fang, and D. T. Kamei, "Development of an Enteric Coating Process for Polymeric Nanoparticles using Chitosan and Alginate", UCLA-USC-Caltech Nanotechnology & Nanomedicine Symposium, **Oct 2013**.

G. L. Mosley, S. K. L. Cheng, D. S. Quinlan, C. T. Liu, P. M. Nafisi, D. Das, G. Fang, and D. T. Kamei, "Delaying Drug Release in Acidic Environments using Chitosat-Alginate for Colon Specific Drug Delivery", 13th Annual UC Systemwide Bioengineering Symposium, **June 2013**.

PATENTS

D. T. Kamei, Y. T. Chiu, B. M. Wu, **G. L. Mosley**. "Methods and Devices for Analyte Collection, Extraction, Concentration, and Detection for Clinical Applications". (provisional patent), **Sept 2015**.

D. T. Kamei, Y. T. Chiu, B. M. Wu, **G. L. Mosley**. "Method and Device for Integrating Analyte Extraction, Concentration, and Detection". (non-provisional patent pending), **Mar 2014**.

D. T. Kamei, **G. L. Mosley**, D. S. Quinlan, C. T. Liu, P. M. Nafisi, D. Das, and G. Fang. "Nanoparticles for the Treatment of Inflammatory Bowel Disease". (provisional patent), **Nov 2012**.

1 Motivation and Background

1.1 Point-of-care (POC) Diagnostics

Infectious diseases currently account for over 25% of the total annual deaths worldwide[1]. One of the cornerstones to significantly reducing the impact of infectious diseases is through frequent surveillance and screening[1,2]. The field of bioengineering is constantly innovating and advancing diagnostic technology; however, more often than not, these innovations are only accessible in communities with privileged resources[2,3]. Cutting-edge diagnostic equipment is often located within high-end hospitals or centralized laboratory locations due to the cost and/or complexity of the equipment. This creates a dilemma in that the advanced diagnostic equipment capable of accurately testing patients is not accessible to a vast majority of the people who need it.

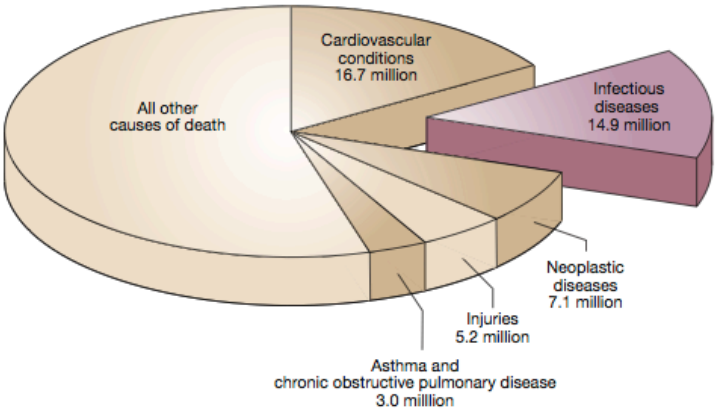

Infectious diseases	Annual deaths (million)
Respiratory infections	3.96
HIV/AIDS	2.77
Diarrhoeal diseases	1.80
Tuberculosis	1.56
Vaccine-preventable childhood diseases	1.12
Malaria	1.27
STDs (other than HIV)	0.18
Meningitis	0.17
Hepatitis B and C	0.16
Tropical parasitic diseases	0.13
Dengue	0.02
Other infectious diseases	1.76

Figure 1-1. Causes of death worldwide with details on infectious disease-related deaths. Figure is reprinted from Morens *et al*[1], with permission.

This has led to a growing focus on point-of-care (POC) diagnostics. While the definition of POC diagnostics can vary slightly, there are several essential properties:

i. Requires minimal or no training

ii. Is a fully automated or self-contained test

iii. Uses unprocessed or minimally processed specimens

iv. Does not require power

v. Is cost efficient

vi. Gives reliable results

Diagnostics that meet these criteria would enable the widespread testing and frequent screening required to deliver an effective strategy to circumvent infectious diseases.

1.2 Lateral-Flow Immunoassay (LFA)

One of the most common POC diagnostic technologies is the LFA, which is a paper-based device. The results for LFA are visually interpreted and dependent on binding interactions between a colorimetric probe, the target analyte, and immobilized molecules on the paper diagnostic. LFA meets many of the POC criteria making them very good candidates as potential infectious disease diagnostics.

However, one caveat for using LFA technology is that the limit of detection is relatively high compared to laboratory-based tests. For example, enzyme-linked immunosorbant assays (ELISAs) typically have a 10-100 fold lower limit of detection when diagnosing infectious diseases[4]. When LFA is used to detect target molecules that are in abundance, such as the human chorionic gonadotropin (hCG) hormone in LFA

pregnancy tests, a high limit of detection does not significantly impact the results of the diagnostic. However, when used to detect the presence of infectious disease pathogens, a high limit of detection can significantly lower the sensitivity of the assay, resulting a large percentage of false negative results. For example, commercially available LFA tests used to diagnose chlamydia have a sensitivity of less than 50%, meaning that more than half of all the patients infected with chlamydia will receive results indicating that they are not infected[5].

LFA tests are comprised of 4 basic components as shown in **Fig. 1-2**. The sample pad is where the sample solution is introduced to the diagnostic, which serves to start the wicking process and often to filter out sample particulates, such as red blood cells. The conjugate pad contains the dehydrated colorimetric indicator. When the sample solution reaches this point, it will resolubilize the colorimetric indicator, and binding between the target analyte and the antibodies on the colorimetric indicator will occur. The nitrocellulose membrane is where the test and control line proteins have been immobilized. This is the part of the diagnostic that the user will see in order to interpret the results. The last component is the absorbent pad, which acts as a sink to provide continuous fluid flow.

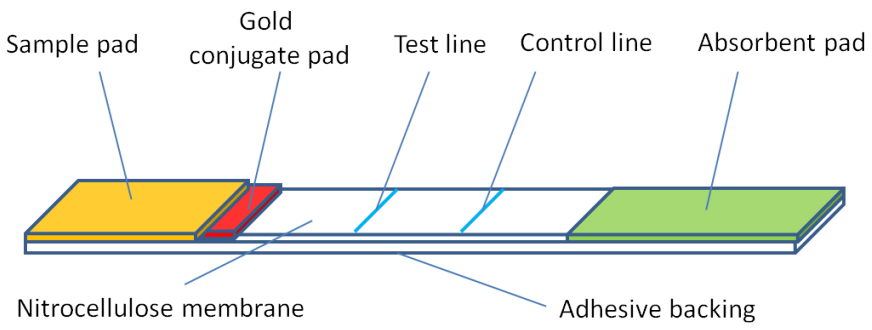

Figure 1-2. Diagram of a typical LFA device.

1.3 LFA detection mechanisms

There are two major classes of LFA tests, the sandwich assay and the competition assay. The sandwich assay is designed to test for the presence of larger targets that have multiple binding sites, such as bacteria or viruses. When testing a sample solution containing the target pathogen, the solution will mix with the colorimetric probe, and the probe will bind to the target molecules using the antibodies decorated on its surface. The solution will flow along the nitrocellulose membrane, where the pathogen and probe complex will bind to the test line, which contains immobilized antibodies that are specific for the target pathogen. This results in the presence of a test line indicating a positive result. When testing a sample solution that does not contain the target pathogen, the colorimetric probe will pass over the test line without binding, resulting in the absence of a test line which indicates a negative test. In either scenario, the colorimetric probe will bind to the control line which contains secondary antibodies that are specific to the antibodies on the probe. The presence of the control line indicates that the diagnostic has been successfully performed as the liquid has flowed entirely up the strip.

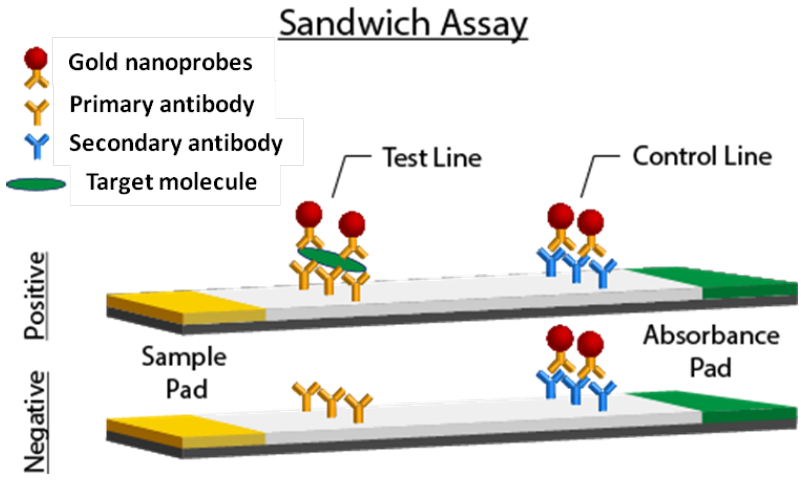

Figure 1-3. Diagram of the sandwich assay.

The other class of LFA tests is the competition assay, which is designed to test for the presence of smaller targets that typically have only 1 binding site, such as protein biomarkers or small molecules. The major difference between a competition and sandwich LFA is that a competition LFA has immobilized target molecules on the test line as opposed to immobilized antibodies that bind to the target. When testing a sample solution containing the target analyte, the solution will mix with the colorimetric probe, and the target molecules will completely saturate the binding sites of the antibodies decorating the surfaces of the probe. As the sample solution flows along the membrane, the probe will pass over the test line without binding to the immobilized target. This results in the absence of a test line, which indicates a positive result. When testing a sample solution that does not contain the target analyte or that has insufficient target analyte, the colorimetric probe will bind to the test line with one of the available antibody binding sites. This results in the presence of a test line, indicating a negative test. Again, in either scenario, the probe will bind to the control line indicating that the test was successfully run.

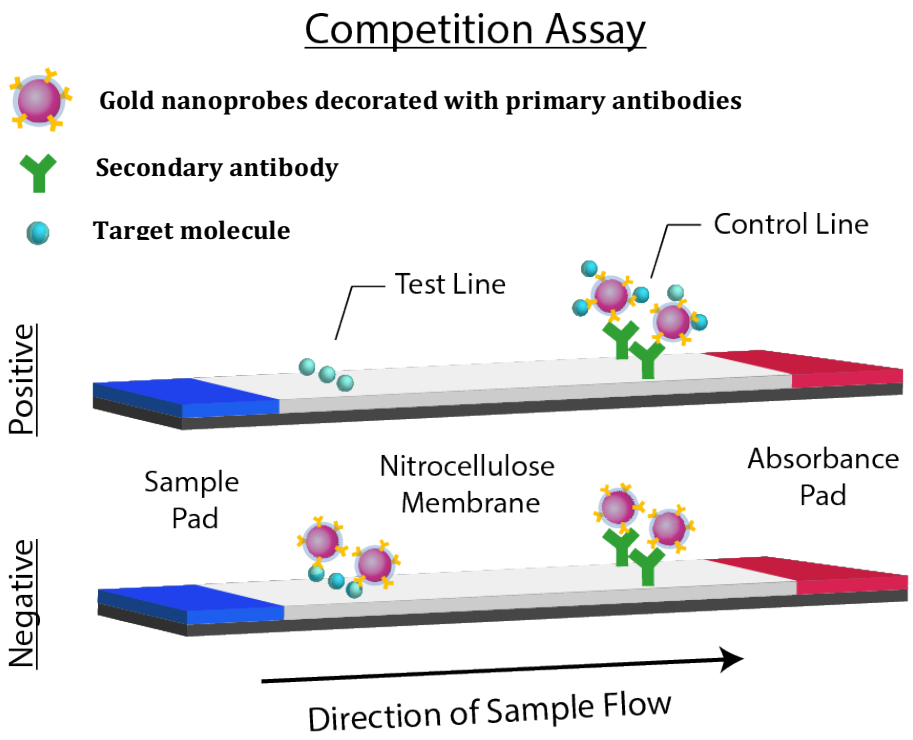

Figure 1-4. Diagram of the competition assay.

1.4 Gold nanoprobes (GNPs)

An important component in any LFA test is the colorimetric indicator. This is comprised of a core material conjugated with a binding moiety, most often antibodies that specifically bind to the target analyte. There are a variety of different materials used for the core; however, it is most common to use gold nanoparticles. Gold nanoparticles have been used in a wide range of diagnostic applications, including optical biosensing[6], detection of DNA[7], and cancer diagnostics[8]. Gold nanoparticles have several benefits that make them suitable for use in LFA diagnostics. Gold nanoparticles give off a strong intense red color (for particles less than 100 nm in diameter) due to the interaction of incident light with a

collective oscillation of free electrons in the particles, a phenomenon known as localized surface plasmon resonance. A strong color is important considering that the results of the LFA test are visually interpreted. Another benefit is that gold nanoparticles are very suitable for functionalization. The gold surface readily accepts dative bonds from amine or thiol groups on proteins without the need for a chemical linker.

There are variety of different methods for producing gold nanoparticles[9–11]; however, they are all based off of the process of reducing chloroauric acid ($H[AuCl_4]$) in solution. This reduction then results in a disproportionation reaction which produces neutral gold atoms. The neutral gold atoms act as nucleation sites, around which additional Au^+ is reduced. In this work, we predominantly used dextran-coated gold nanoprobes (DGNPs). For this class of nanoprobes, the dextran acts as the reducing agent in solution. It also serves to provide a polymer coating layer for the particles once they are formed. This polymer coating helps provide colloidal stability in high ionic strength suspensions.

The most common technique for characterizing the size of GNPs is transmission electron microscopy, which provides a precise image of the gold core[12]. Other methods, such as atomic force microscopy, small-angle X-ray scattering[13], and laser desorption-ionization mass spectrometry[14], are also used. There are other methods of determining the size and concentration that require less preparation and time, such as UV-visible spectra absorption[15] and dynamic light scattering[16].

1.5 Kinetics of ligand binding

Let's consider the following binding event where a ligand L binds to a free receptor R to form the complex C.

$$L + R \underset{k_r}{\overset{k_f}{\rightleftharpoons}} C \tag{1}$$

The association rate is equal to the product of the ligand and free receptor concentrations times a constant, which is called the forward rate constant k_f. The dissociation rate is proportional to the concentration of the complex. Net binding leads to the formation of the complex C and to a corresponding decrease of L and R. The representative differential equations are as follows:

$$\frac{dL}{dt} = -k_f[L][R] + k_r[C] \tag{2}$$

$$\frac{dR}{dt} = -k_f[L][R] + k_r[C] \tag{3}$$

$$\frac{dC}{dt} = k_f[L][R] - k_r[C] \tag{4}$$

When all rate constants and all initial concentrations are known, the concentrations and rate of concentration change can be determine for any given time t.

Equilibrium is reached for reversible reactions when the dissociation rate is equal to the association rate:

$$k_f[L][R] = k_r[C] \tag{5}$$

Equation (5) can be rearranged to obtain **Eq. (6)** for the equilibrium dissociation constant K_D.

$$K_D \equiv \frac{[L]_{eq}[R]_{eq}}{[C]_{eq}} = \frac{k_r}{k_f} \tag{6}$$

The K_D can be viewed as the equilibrium ligand concentration where half of the binding sites are occupied, since setting $[L]_{eq}$ to K_D yields $[R]_{eq}/[C]_{eq}$ equal to 1.

Bound ligand and free ligand concentrations must add up to the total ligand concentration L_o. The same must hold for all components of bound and free receptors, which add up to the total receptor concentration R_o:

$$R_o = [R] + \frac{[L][R]}{K_D} \tag{7}$$

$$L_o = [L] + \frac{[L][R]}{K_D} \tag{8}$$

Equations (7) and **(8)** are two equations with the two unknowns [L] and [R], and they represent mole balances on the two types of molecules. If there were many types of molecules, more balances would be necessary, which would make the equilibrium condition more complex.

1.6 Aqueous two-phase systems (ATPSs)

A large portion of this work revolves around the concept of utilizing aqueous two-phase systems (ATPSs) to improve the detection limit of LFA. Our lab has demonstrated the ability of ATPSs to pre-concentrate target biomolecules prior to detection with LFA. We have shown that this is possible in solution with viruses[17], DNA[18], and protein targets[19,20]. We have also demonstrated the ability of the phase separation and target concentration to occur during flow through the paper diagnostics itself, drastically reducing the overall time to result and complexity of the test[21,22].

An ATPS is an aqueous solution that separates into two distinct phases, both of which are predominantly comprised of water[23]. The reason for immiscibility can vary depending on the type of ATPS. These systems have many advantages for their use in

bioseparations processes. Namely, they provide mild conditions for the biomolecules, the processes are scalable and predictable, and partitioning of the biomolecules occurs rapidly[24,25]. Properties of the target molecule will affect its own partitioning within the ATPS. These properties include a combination of relative hydrophobicity, electrical potential, size, biospecific affinity, and conformation dependency[26–28].

The work in this thesis involving ATPSs has exclusively involved the polyethylene glycol (PEG)-potassium phosphate ATPS. However, there are many other types of ATPSs, including micellar, polymer-polymer, polymer-micellar, and other polymer-salt ATPSs. The mechanism of phase separation for the PEG-salt system can be described in general as the presence of potassium phosphate causing the PEG to like itself more than water to be able to form PEG-rich domains. Specifically, the salt ions disrupt the hydration shell surrounding the PEG, which makes PEG interact less favorably with water. The removal of the hydration shell also allows the individual PEG molecules to come into contact with each other and experience greater attractive van der Waals interactions[29]. As the concentration of salt increases for a given PEG concentration, this disruption will increase, and therefore, the PEG-PEG interactions will increase and PEG-water interactions will decrease.

In order for phase separation to occur, the solution components must cross a threshold of PEG and salt concentrations. This can be represented as the binodal curve on a phase diagram (**Fig. 1-5**) which plots the concentrations of PEG and salt on the y- and x-axes, respectively. This phase diagram also contains tie-lines. Several pieces of information can be extracted from a given tie line. The point located within the two-phase region represents the concentrations of PEG and salt for the entire solution volume, i.e., they are

the initial concentrations for PEG and salt when the system is one phase. The points at which the tie-line intersects the binodal curve, close to the y-axis and x-axis, represent the component concentrations within the PEG-rich and salt-rich phases, respectively. Finally, the ratio of the distance between the point in the two-phase region and intersecting points is equal to the ratio of the volumes of the PEG-rich and salt-rich phases after macroscopic phase separation is complete. More specifically:

$$\frac{length_{center-left}}{length_{center-right}} = \frac{volume_{Salt}}{volume_{PEG}} \tag{9}$$

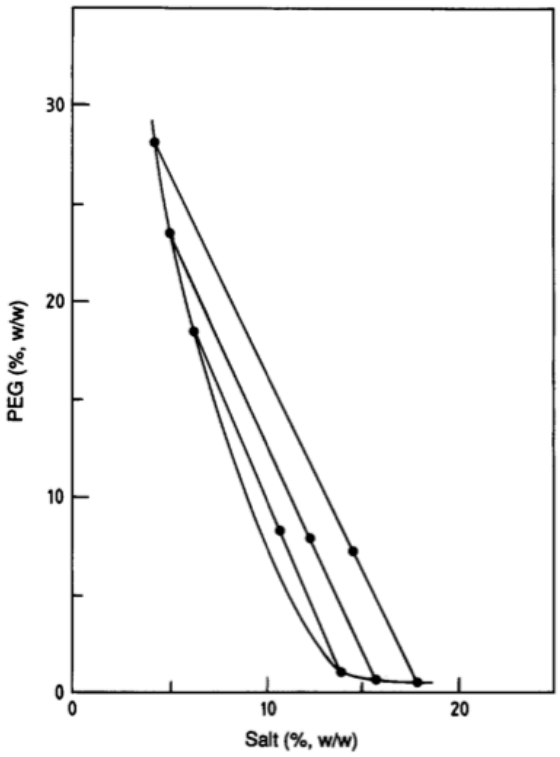

Figure 1-5. Phase diagram of the polyethylene glycol (PEG)-potassium phosphate system. Figure is reprinted from Walter *et al*[30], with permission.

2 Novel Methodology for Determining Important LFA Parameters

2.1 Overview

The lateral-flow immunoassay (LFA) is a well-established diagnostic technology that has recently seen significant advancements due in part to the rapidly expanding fields of paper diagnostics and paper-fluidics. As LFA-based diagnostics become more complex, it becomes increasingly important to quantitatively determine important parameters during the design and evaluation process. However, current experimental methods for determining these parameters have certain limitations when applied to LFA systems. In this work, we describe our novel methods of combining paper and radioactive measurements to determine nanoprobe molarity, the number of antibodies per nanoprobe, the forward and reverse rate constants for nanoprobe binding to immobilized target on the LFA test line, the volumetric flow rate, and the fluid volume within the membrane test line. Using a model LFA system that detects for the presence of the protein transferrin (Tf), we demonstrate the application of our methods, which involve quantitative experimentation and mathematical modeling. We also compare the results of our rate constant experiments with traditional experiments to demonstrate how our methods more appropriately capture the influence of the LFA environment on the binding interaction. Our novel experimental approaches can therefore more efficiently guide the research process for LFA design, leading to more rapid advancement of the field of paper-based diagnostics.

2.2 Motivation and Background

The lateral-flow immunoassay (LFA) is a well-established paper-based technology for detecting biological agents and has a broad range of academic and commercial applications.[31] Due to the unique combination of specificity, speed, simplicity, and low cost, LFA has seen extensive use in many areas, including medical diagnostics, food safety, and defense against bio-warfare agents.[32–35] Even though LFA is a mature technology, it has recently seen significant progress in part due to the rapidly expanding fields of paper-fluidics and paper diagnostics. Some recent key innovations in these fields include work with two-dimensional paper networks,[36–44] microfluidic paper-based analytical devices (μPADs),[45–49] and equipment-free thermodynamic target concentration.[17–22,50] These innovations improve the applicability, robustness, and accuracy of LFA, but at the same time, increase the complexity of the technology.

Development of new and more complex paper-based devices would benefit significantly from being able to quantitatively assess the effects of varying important LFA parameters on device performance. For example, it would be useful to know the effects of manipulating the colorimetric nanoprobes on the forward ($k_{f,s}$) and reverse ($k_{r,s}$) rate constants for the probe binding to and dissociating from the test line, respectively. Engineering paper-based devices such that $k_{f,s}$ is increased and $k_{r,s}$ is decreased would lead to better performance of the diagnostic as conditions would be optimal for probe binding to the strip. The current standard for determining these rate constants is through the use of surface plasmon resonance (SPR)[51,52]; however, the value determined from SPR does not capture the intricacies of the LFA system that may affect binding properties. For example,

it does not capture the effects of the microenvironment of the probe, the interactions between the probe and the LFA membrane, or the effects of the sample solution components.

Another important LFA parameter is the colorimetric probe molarity. It is important to know and maintain a consistent probe molarity when comparing different diagnostic designs. Current methods for quantifying probe molarity have several issues, such as requiring initial calibration with custom-made standard nanoparticle solutions, limited applicability with respect to probe size and material, and the inability to discern bare nanoparticles from ones conjugated with antibodies.[53]

For these reasons, we developed novel experimental methodologies that were specifically designed to benefit LFA research. To do this, the forward and reverse rate constants for binding were obtained using an experimental setup that exactly mimics the LFA environment. Further experimentation demonstrated how these values more appropriately captured the effects of the LFA system by comparing them to values determined from traditional methods. We also developed a novel method that could determine probe molarity regardless of probe composition or structure. From this experimental data, the number of antibodies per probe (A:P) could also be calculated. Finally, the volumetric flow rate (Q) and test line fluid volume (ν) were evaluated. Knowing the effects of changing these parameters would be useful during LFA design as there is always a balance between having a shorter LFA time for user convenience and a longer LFA time to give the probes more time to bind to the test line, and these times are related to ν/Q.

In this work, our novel approaches that combine radioactive iodine-125 (^{125}I) labeling, mathematical modeling, and LFA assembly are discussed. We demonstrate application of these methodologies using a model LFA system which detects the presence or absence of the protein transferrin (Tf). To our knowledge, no one has ever combined radioactivity and LFA to attain any of these important quantitative values.

2.3 Materials and Methods

2.3.1 Preparation of competition LFA tests for detection of transferrin (Tf)

A competition LFA was utilized in this study. Tf was immobilized on a nitrocellulose membrane (Sartorius, Goettingen, Germany) to form the test line. This process was accomplished by dispensing a solution of 25% w/v sucrose and varying concentrations of Tf at a controlled rate using a syringe pump across the nitrocellulose membrane. All materials were purchased from Sigma-Aldrich unless otherwise noted. In a competition LFA test, the colorimetric probe binds to the test line when no target is present, displaying a red line to indicate a negative test. As the concentration of target in the sample of interest increases, less probe binds to the test line until the target concentration is sufficient to prevent any visible binding, indicating a positive test. The nitrocellulose membrane was assembled with a sample pad (Whatman, Pittsburgh, PA) and an absorbent pad (Whatman, Pittsburgh, PA) using an adhesive backing (Whatman, Pittsburgh, PA), which is common practice for LFA. Many of the experiments required measuring the radioactivity of the test line and subtracting out the background radioactivity signal. To accomplish this, the back of the LFA test was marked to indicate a 0.7 cm length which

encompassed the test line. This length of paper was cut out and measured to represent the test line radioactivity. A separate 0.7 cm length located upstream of this position was also marked and measured to serve as the background radioactivity signal.

2.3.2 Preparation of antibody-decorated dextran-coated gold nanoprobes (DGNPs)

LFA tests require a colorimetric indicator, typically in the form of a nanoparticle conjugated to a binding moiety. For these experiments, we used dextran-coated gold nanoparticles which were synthesized according to Min and coworkers with slight modifications.[54] Briefly, 6 g of dextran (Mw 15,000–25,000) from *Leuconostoc spp*. were dissolved in 80 mL of filtered UltraPure sterile water (Rockland Immunochemicals Inc., Gilbertsville, PA). The solution was stirred and heated to a boil, after which 1080 μL of a 1% w/v gold(III) chloride hydrate solution were added. The color of the reaction mixture turned reddish-violet and was stirred and boiled for about 20 min. The newly formed dextran-coated gold nanoparticles were centrifuged to remove free dextran and resuspended in 70 mL of water. To form functionalized DGNPs, the pH of the dextran-coated gold nanoparticle solution was adjusted to 9.0 using 1.5 M NaOH. For every 1 mL of dextran-coated gold nanoparticle solution, 8 μg of anti-Tf antibodies (Bethyl Laboratories, Montgomery, TX) were added. The reaction mixture was placed on a shaker for 30 min to facilitate the formation of dative bonds between the antibodies and the dextran-coated gold nanoparticles. Free antibodies were removed by centrifugation. The pellet was resuspended in 100 μL of 0.1 M sodium borate buffer at pH 9.0, and these antibody-decorated dextran-coated gold nanoprobes will be referred to as DGNPs.

2.3.3 Radiolabeled antibodies and transferrin

The radioactive ^{125}I was conjugated to the tyrosine residues of the goat anti-Tf antibody (Bethyl Laboratories, Montgomery, TX) and Tf (Sigma, St. Louis, MO). Briefly, $Na^{125}I$ (MP Biomedicals, Irvine, CA) was activated by IODO-BEADS (Pierce Biotechnology, Rockford, IL). Subsequently, the activated ^{125}I was reacted with 100 μg of protein for 15 min. The radiolabeled antibodies were purified from free ^{125}I using a Sephadex G10 size-exclusion column. The specific activity and concentration of the radiolabeled antibodies were determined by a phosphotungstic acid (PTA) assay.

2.3.4 Determining $k_{r,s}$ for DGNP (probe) binding to an immobilized Tf on the test line (surface target)

LFA test strips were placed into an open centrifuge tube containing 70 μL of a suspension with a high concentration (65 nM) of DGNPs (conjugated with radiolabeled anti-Tf antibodies) in order the saturate the test line with DGNPs. The DGNPs were in a suspension of gold buffer and phosphate-buffered saline (PBS). Gold buffer is commonly used in LFA tests to promote nanoparticle flow, and our gold buffer was comprised of bovine serum albumin (BSA), polysorbate 20 (TWEEN 20), sodium azide, and polyethylene glycol (PEG) 8,000 MW in tris(hydroxymethyl)aminomethane (Tris) base buffer. After 20 minutes, the test strips were switched to a 125 μM non-radiolabeled Tf solution in PBS. This high concentration of unlabeled Tf was used to prevent any dissociated DGNPs from rebinding to the test line as the unlabeled Tf would outcompete the Tf on the test line for binding to the anti-Tf antibodies on the dissociated DGNPs. At

varying time points, the test strips were removed from solution, and the test lines and background segments were cut out and measured for radioactivity. It was necessary to replace the absorbent pads and refill the PBS solution to maintain a steady flow of solution. A 0.7 cm length of the test strip which contained the test line was cut out and placed into a 5 mL, 75 x 12 mm, polypropylene tube (Sarstedt, Numbrecht, Germany). A separate 0.7 cm length of test strip, located upstream of the prior 0.7 cm segment and not containing the test line, was also cut out and placed into a separate tube. The radioactivity for both segments were measured in counts per minute (CPM) using a Cobra Auto-Gamma counter. The upstream segment was used to represent the background signal that was subtracted from the measurement. The radioactivity CPM values were then converted into a quantity of probe-bound antibodies associated with the test line using the specific activity of the antibodies from the PTA assay.

2.3.5 Determining $k_{f,s}$ for DGNP (probe) binding to an immobilized Tf on the test line (surface target)

LFA test strips were placed into an open centrifuge tube with 70 µL of a suspension containing DGNPs (conjugated with radiolabeled anti-Tf antibodies) and gold buffer in PBS. At varying time points, the test strips were removed and the radioactivity associated with the probe-bound antibodies on the test line was measured, similar to the process described for determining $k_{r,s}$ in the previous section.

2.3.6 Determining $k_{r,b}$ for Tf (bulk target) binding to an antibody on DGNP (bulk probe)

400 µL of a 100 µg/mL radiolabeled Tf solution in PBS were mixed with 10 µL of a non-radioactive DGNP suspension. The resulting mixture was allowed to incubate for 2 hours to maximize binding. Each suspension was then spun at 18k rcf for 1 hour. The supernatant was then removed, and the pellet containing the DGNPs was resuspended with 800 µL of a 10 mg non-radiolabeled Tf/mL solution. This high concentration of unlabeled Tf was used to prevent any dissociated antibodies on the DGNPs from rebinding to the radiolabeled Tf molecules as the unlabeled Tf would outcompete the radiolabeled Tf for binding to the anti-Tf antibodies on the dissociated DGNPs. At varying time points, each suspension was then spun again at 18k rcf for 30 minutes to separate the free from the bound radiolabeled Tf. The supernatant was removed, and the pellet was resuspended. The radioactivity of this resuspended suspension was measured using a gamma counter. The radioactivity CPM values were then converted into a Tf quantity using the specific activity of Tf obtained from the PTA assay. The amount of Tf in the pellet corresponded to the amount of Tf bound to the antibodies on the DGNPs, and this number was converted to molarity based on the known volume of the suspension before forming the first pellet.

2.3.7 Determining $k_{f,b}$ for Tf (bulk target) binding to an antibody on DGNP (bulk probe)

400 µL of radiolabeled Tf in PBS were mixed with 10 µL of a non-radioactive DGNP suspension. At varying time points, the suspension was spun at 18k rcf for 5 minutes. Supernatant was discarded, and the pellet was resuspended. The radioactivity

associated with the pellet was measured using a gamma counter, and this value was converted into a Tf quantity using the specific activity of Tf from the PTA assay. This value corresponded to Tf bound to antibodies on the DGNPs, which was converted to molarity based on the known volume of the suspension before forming the first pellet.

2.3.8 Determining the Tf concentration on the test line ($T_{s,0}$), DGNP molarity, and the number of antibodies per probe (A:P)

Tf LFA membranes were made with several different Tf concentrations (0.4, 0.2, 0.1, 0.05, 0.025 mg/mL) and with several different test line volumes (1, 0.8, 0.6, and 0.4 μL). LFA test strips were placed into an open centrifuge tube with 200 μL of solution containing a high concentration of radiolabeled anti-Tf antibody. LFA test strips were separately placed into an open centrifuge tube with 200 μL of suspensions containing DGNPs conjugated with radiolabeled anti-Tf antibody. Experiments were performed to determine the concentration of radiolabeled antibody and DGNPs required to saturate the immobilized Tf on the test line of the membrane. The radioactivity on the test line was then measured using a procedure similar to one described earlier (see *Determining $k_{r,s}$ for DGNP (probe) binding to an immobilized Tf on the test line (surface target)*). Radiolabeled anti-Tf antibody solutions and DGNP suspensions were also run on test strips with no immobilized Tf, which were used to subtract out any signal due to nonspecific binding. The radioactivity measurement for the experiment that saturated the test line with radiolabeled DGNPs was labeled as P_{max}, while the radioactivity measurement for the experiment that saturated the test line with radiolabeled antibodies was used to determine the moles of surface immobilized target molecules available for binding, $T_{s,0}$. $T_{s,0}$ can be

calculated by converting the CPM values into the moles of Tf immobilized on the test line by dividing the CPM by the specific activity of the radiolabeled antibodies. As described in the *Results and Discussion* section, the probe molarity can be calculated using the P_{max} and $T_{s,0}$ values, while the number of antibodies per probe A:P can be calculated using P_{max}, $T_{s,0}$, and the specific activity of the antibody.

2.3.9 Determining volumetric flow rate (Q) in the strip

The volumetric flow rate was experimentally determined by placing LFA test strips into solutions of radiolabeled Tf and measuring the radioactivity of the remaining solution at different time points. Since the initial radioactivity and the concentration of radiolabeled Tf in the tube are known, measuring the decrease in radioactivity and dividing by the concentration yielded the average volumetric flow rate.

2.3.10 Determining the fluid volume in the test line (v)

The fluid volume in the test line was experimentally determined by first placing blank LFA test strips, i.e., membranes without immobilized test lines, into a solution of radiolabeled Tf. After the solution completely flowed across the nitrocellulose membrane, a known area of test strip was cut out. The radioactivity in this known area was measured, and after dividing by the radioactivity per volume of the Tf solution, the volume in the known area (vol/cm^2) was determined. The fluid volume in a test line was then determined by first measuring the area of the test line and then multiplying by the fluid volume/cm^2.

2.4 Results and Discussion

2.4.1 Determining the probe molarity and the number of antibodies per probe (A:P) for the DGNP suspension

2.4.1.1 Determining the concentration of probes

Current methods for determining nanoparticle molarity for LFA research suffer from several limitations. A review paper by Gao and coworkers critically summarized these methods.[53] A majority of the methods rely on electromagnetic waves interacting with the probes. This interaction is extremely sensitive to changes or variability in probe composition and structure, which is the source of many of the limitations. We therefore took a different approach and developed a method that relies on the binding interaction of the probe as the basis for determining the molarity. Since binding interactions are a universal component of LFA probes, our novel method can determine the probe molarity regardless of the probe size or composition, as well as discern between bare nanoparticles and antibody conjugated probes.

To demonstrate the efficacy of our methods, we used the model target protein Tf and DGNPs decorated with anti-Tf antibodies. The experimental process required initially flowing a high concentration of radiolabeled antibody along an LFA test strip in order to saturate the immobilized target on the test line. This value yielded the number of Tf molecules immobilized on the test line that were available for binding, which was estimated to be the total moles of immobilized surface target on the test line, $T_{s,0}$. Specifically, the CPM measured from the experiment was divided by the specific activity

(CPM Antibody/Mol Antibody) determined by the PTA assay to obtain the moles of Tf on the test line assuming a 1:1 binding stoichiometry between the immobilized Tf and the antibody. We had first considered approximating the moles of immobilized Tf molecules per test line ($T_{s,0}$) by using the volume of the printed test line and the concentration of the Tf solution used for target immobilization, but felt that this approximation would overestimate the available number of Tf molecules, considering that a portion of immobilized targets usually are not in the proper binding orientation and another portion are not completely immobilized and will re-solubilize and flow out of the detection zone.

Subsequently, in a different study, the test lines of identical LFA strips were saturated with DGNPs that were conjugated with radiolabeled antibody. The measured radioactivity of these test lines were denoted P_{max} for the radioactivity associated with the maximum moles of probes bound. Since the binding sites in the two experiments (antibody only and the probe with antibody experiments) were completely saturated, we assumed that the number of antibodies that were used to evaluate $T_{s,0}$ was equal to the number of probes bound to get P_{max}. The radioactivity corresponding to P_{max} was then divided by $T_{s,0}$ to get a value for the (CPM Probe/Mole Probe), which will be referred to as the P_{max}:$T_{s,0}$ ratio. The P_{max}:$T_{s,0}$ ratio can be used as the specific activity to calculate the molarity of the original probe solution.

However, this process assumes that the probe does not bind multiple immobilized targets and that it does not sterically block another probe from binding to a Tf molecule on the test line. Both of these scenarios would mean that the estimate for $T_{s,0}$ is greater than the actual moles of probe that bind. Accordingly, since $T_{s,0}$ is in the denominator of the P_{max}:$T_{s,0}$ ratio, the true (CPM Probe/Mole Probe) value would be greater than the P_{max}:$T_{s,0}$

ratio estimate for this parameter. Since the measured radioactivity of the probe solution is divided by the P_{max}:$T_{s,0}$ ratio to attain the moles of probe, the concentration of probes would be overestimated. To address this problem, the experimental process was designed so that the P_{max}:$T_{s,0}$ ratio was determined at a condition where steric hindrance and multivalency were negligible.

To identify this condition, a series of LFA test strips were printed with varying concentrations of immobilized Tf on the test line. The idea is that, as the concentration of immobilized Tf decreases, the problems associated with steric hindrance and multivalency decrease due to the increased distance between the surface Tf molecules. To identify the immobilized Tf concentration at which multivalency and steric hindrance becomes negligible, test lines of varying sizes (0.6 μL to 1 μL) were used for each immobilized Tf concentration. Accordingly, for each membrane concentration condition, the P_{max}:$T_{s,0}$ ratio could be estimated by finding the slope of the linear regression for the different test line volumes. While it is possible to determine the P_{max}:$T_{s,0}$ ratio from a single test line size, it was important to demonstrate that the ratio was only a function of immobilized target concentration and not the total quantity. As steric hindrance and multivalency becomes less significant, the P_{max}:$T_{s,0}$ ratio will increase as there will be more probes bound per $T_{s,0}$ value, i.e., the measured P_{max}:$T_{s,0}$ ratio will increase. Once steric hindrance and multivalency become negligible, the P_{max}:$T_{s,0}$ (slope) will stop significantly changing in response to decreasing the immobilized Tf concentration. These slopes were considered to be the true P_{max}:$T_{s,0}$ ratios, and were used for subsequent calculations of the probe molarity and antibody per probe values.

The data (**Fig. 2-1** & **Table 2-1**) demonstrates that the slopes of the P_{max}:$T_{s,0}$ increase as the membrane Tf concentration decreases. Note that the legend on **Fig. 2-1** groups the data by the initial concentration of the Tf solution used during the Tf immobilization process (i.e., membrane printing). Statistical analysis of the slopes shows that the slope of the 0.025 mg/mL condition is significantly different from all of the other slopes except the 0.05 mg/mL condition. This suggests that the effects of steric hindrance and multivalency become negligible at these initial Tf concentrations used for printing the membranes. Therefore, the P_{max}:$T_{s,0}$ ratio from the 0.025 mg/mL condition was used in subsequent calculations. The probe stock solution was measured to be 3.53×10^{11} CPM/L, which was divided by the P_{max}:$T_{s,0}$ ratio to yield a probe concentration of 2.28×10^{-7} mol/L or M.

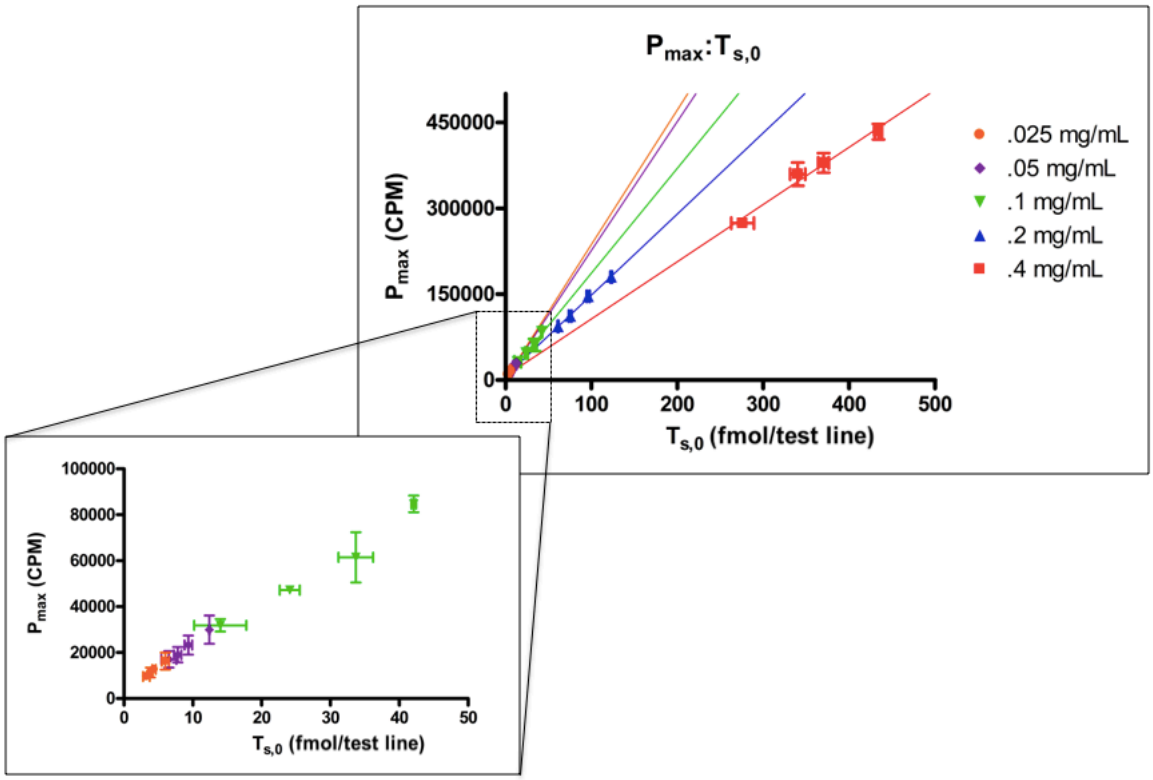

Figure 2-1. Determining P_{max}:$T_{s,0}$ Ratio. Correlation of the radioactivity of the probe bound to the test line at saturation (P_{max}) to the fmol of surface immobilized target available for binding on the test line ($T_{s,0}$). The legend describes the Tf concentrations of the solutions that were used to immobilize Tf on the test line during the membrane printing process. For each of these concentrations, different points were obtained by varying the test line volumes. The lines represent the linear regression of the data points with identical immobilized Tf concentrations. The error bars represent the standard error of the mean.

Table 2-1. Linear Regression Data of the P_{max}:$T_{s,0}$ Slopes. Relevant metrics from the linear regression of the data in Fig. 1. The right most column represents the results from a one-tailed *t* test that examined the significance in the difference between the slope of the 0.025 mg/mL condition and each of the other conditions.

Tf Printed on Membrane (mg/mL)	P_{max}:$T_{s,0}$ (CPM/mol x10^{18})	Standard Error (CPM/mol x10^{17})	R^2	Significant Difference in Slopes (P value)
0.025	2.34	± 0.93	.997	N/A
0.05	2.25	± 1.22	.995	No (.276)
0.1	1.82	± 2.03	.976	Yes (.028)
0.2	1.39	± 0.61	.996	Yes (<.001)
0.4	0.99	± 1.09	.976	Yes (<.001)

2.4.1.2 Determining the number of antibodies per probe

Using the data from the molarity experiment, the number of antibodies per probe (A:P ratio) could be calculated without further experimentation. To obtain this value, the concentration of antibody in a probe solution was determined by dividing the measured radioactivity by the specific activity of the antibody (CPM Antibody/Mole Antibody) used during the conjugation process. The concentration of probe was then determined using the previously mentioned P_{max}:$T_{s,0}$ ratio, and a ratio was then taken between the concentration of antibody and the concentration of probe. In this case, the ratio was found to be 3.93 or approximately 4 antibodies per probe.

Our novel method of determining probe molarity and the A:P ratio can be performed on any LFA compatible probe regardless of the structure, composition, or polydispersity. The measurement is also not confounded by the presence of bare nanoparticles, a common by-product during probe conjugation. It is useful to be able to accurately determine these parameters in order to quantitatively compare different probe manufacturing processes. It is also important to maintain constant probe molarity and A:P ratio when comparing different LFA diagnostic designs. Finally, it is necessary to know the probe molarity and moles of immobilized target $T_{s,0}$ when calculating the forward and reverse binding rate constants, as described below.

2.4.2 Determining kr,s and kf,s for probe dissociating from and binding to the Tf on the test line

2.4.2.1 Mathematical model

In order to determine the forward and reverse rate constants for binding, we first consider the situation where a probe species with n number of antibodies binds to immobilized target on the surface, where P_b is the molar concentration of the probe (i.e., DGNP) in the bulk solution, T_s is the concentration of the immobilized target (i.e., Tf) on the surface in units of (moles/test line), $P_{s[symbol]}$ is the concentration of the complexes formed between the bulk probe and the surface target in units of (moles/test line). Note that the symbol within the brackets represents the distinct antibody binding site that is bound to the surface target, n is the number of antibodies per probe, and $k_{f,s}$ and $k_{r,s}$ are the forward and reverse binding rate constants for the interaction between an individual antibody binding site and a surface target, respectively.

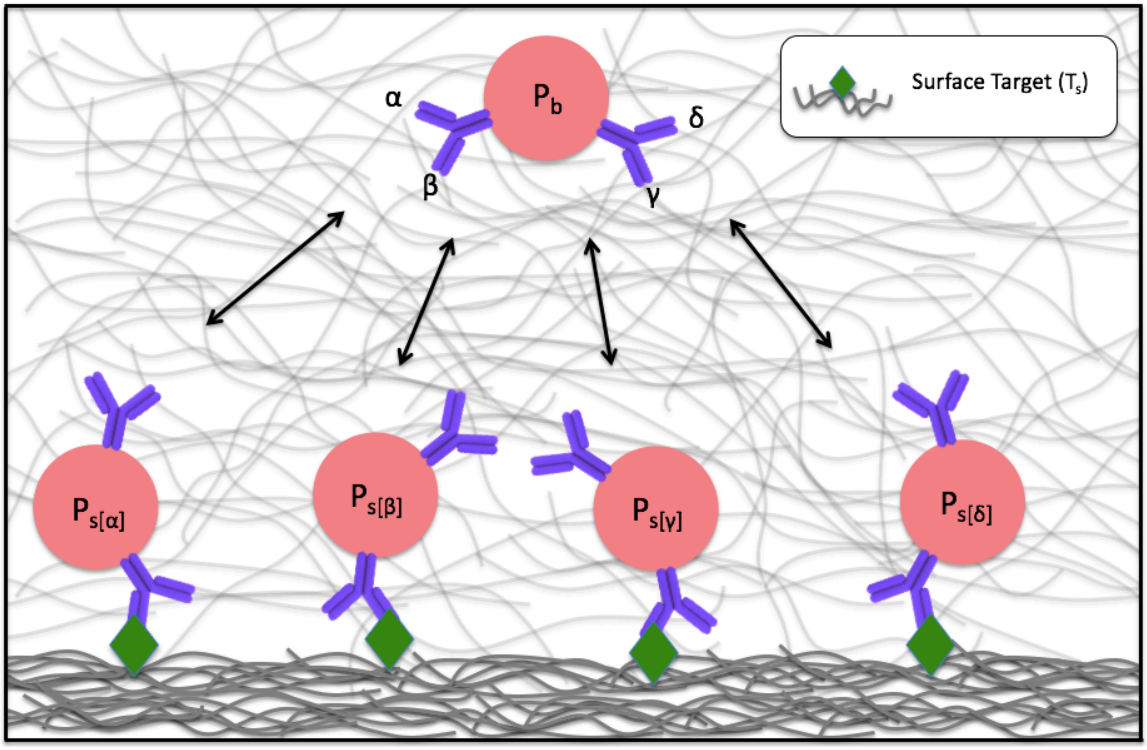

Figure 2-2. Schematic of bulk probe binding to immobilized target on the nitrocellulose membrane. The schematic depicts the binding between a bulk probe (P_b) with 4 antibody binding sites (i.e., n=2) to surface target (T_s), demonstrating the 4 different binding permutations ($P_{s[\alpha]}$, $P_{s[\beta]}$, $P_{s[\gamma]}$, $P_{s[\varepsilon]}$) for this example. Each binding interaction is governed by the rate constants $k_{r,s}$ and $k_{f,s}$. Note that this schematic depicts probes with 4 antibody binding sites for the purpose of clarity, however the probes used during the experimental procedures had 8 antibody binding sites due to there being 4 conjugated antibodies and each antibody having 2 binding sites.

In this binding interaction, we do not consider the effects of multivalency or steric blocking of surface targets by bound probe since the experiments were performed at surface target concentrations where these effects were demonstrated to be negligible as discussed in the previous section.

The binding interactions between the surface target and each of the distinct antibody binding sites can be mathematically described as follows:

$$\frac{dP_{s[symbol]}}{dt} = k_{f,s}P_bT_s - k_{r,s}P_{s[symbol]} \tag{10}$$

In our analysis, we assume that each antibody site has the same binding affinity. This allows us to treat each complex concentration ($P_{s[symbol]}$) as being equal. The entire concentration of complexes in units of (moles/test line) can then be represented as the product of an individual complex concentration and the number of distinct binding permutations:

$$P_s = 2nP_{s[symbol]} \tag{11}$$

where P_s is the total concentration of the complexes, and the coefficient of 2 appears as there are 2 binding sites per antibody. The rate of change of the entire complex concentration can then be obtained by taking the derivative of **Eq. (11)** with respect to time and substituting in **Eq. (10)** to yield:

$$\frac{dP_s}{dt} = 2n\left(k_{f,s}P_bT_s - k_{r,s}P_{s[symbol]}\right) \tag{12}$$

which simplifies to:

$$\frac{dP_s}{dt} = 2nk_{f,s}P_bT_s - k_{r,s}P_s \tag{13}$$

Equation (13) can be used to mathematically determine binding rate constants from experimental data that measures the quantity of complex formation.

The current standard of quantifying complex formation, and therefore, determining the rate constant value, is by surface plasmon resonance (SPR). Unfortunately, this method does not capture the intricacies of LFA systems that may affect binding properties. Some specific examples include the steric repulsion between a polymer coating on the probe and the nitrocellulose membrane surface, or the pH of the sample solution changing the conformation of the binding proteins. In order to capture these interactions, we designed a

novel experimental method that measures binding directly in the LFA test strip. Antibodies were radiolabeled prior to conjugation to the probe which enabled quantification of complex formation by measuring the radioactivity of the test line during the experiments. The process of radiolabeling has minimal impact on the system, and therefore, has negligible affect on the binding interactions. Radioactive decay is also an extremely robust method for quantification in that it is not affected by environmental factors such as pH, ionic strength, temperature, or quenching. This allows the experiment to be performed in a solution that exactly mimics the application of the LFA.

Considering that the experimental procedure directly measures the quantity of probe-bound antibodies associated with the test line, **Eq. (13)** can be modified to represent the experimental measurements by multiplying the complex concentration by the number of antibodies per probe n, which gives us:

$$\frac{d(nP_s)}{dt} = 2n^2 k_{f,s} P_b T_s - n k_{r,s} P_s \tag{14}$$

Equation (14) can then be used with our specific experimental designs to determine the binding rate constants.

2.4.2.2 Determining $k_{r,s}$ for DGNP (probe) binding to an immobilized Tf on the test line (surface target)

To determine the reverse binding rate constant $k_{r,s}$, a high quantity of radiolabeled probe was first allowed to bind to the test line. After near saturation, a solution with a high concentration of non-radiolabeled bulk Tf was flowed across the strip. Under these conditions, any dissociated DGNPs were not able to rebind to the test line as the unlabeled

Tf would outcompete the Tf on the test line for binding to the anti-Tf antibodies on the dissociated DGNPs. **Equation (14)** therefore simplifies for this experiment to the following expression:

$$\frac{d\left(nP_s\right)}{dt} = -nk_{r,s}P_s \tag{15}$$

This equation can be analytically solved and the initial condition $nP_s(0)=nP_{s,0}$ can be applied to yield the following solution:

$$nP_s = nP_{s,0}e^{-k_{r,s}t} \tag{16}$$

where $nP_{s,0}$ is the initial concentration of probe-bound antibody associated with the test line. As shown in **Fig. 2-3**, an exponential decay was observed for the number of complexes as a function of time. Non-linear regression of the data with an exponential decay using GraphPad yielded the following equation (R^2=0.94):

$$Y = 4.17\cdot10^{-14}\,e^{-\left(3.75\cdot10^{-4}\right)t} + 7.62\cdot10^{-14} \tag{17}$$

Equation (17) has a constant offset of $7.62\text{x}10^{-14}$ due to irreversible nonspecific binding to the paper. This does not alter evaluation of the rate constant since $k_{r,s}$ is in the argument of the exponential. Comparing the arguments of the exponential between **Eqs. (16)** and **(17)**, yields a value of $3.75\text{x}10^{-4}$ s^{-1} for $k_{r,s}$.

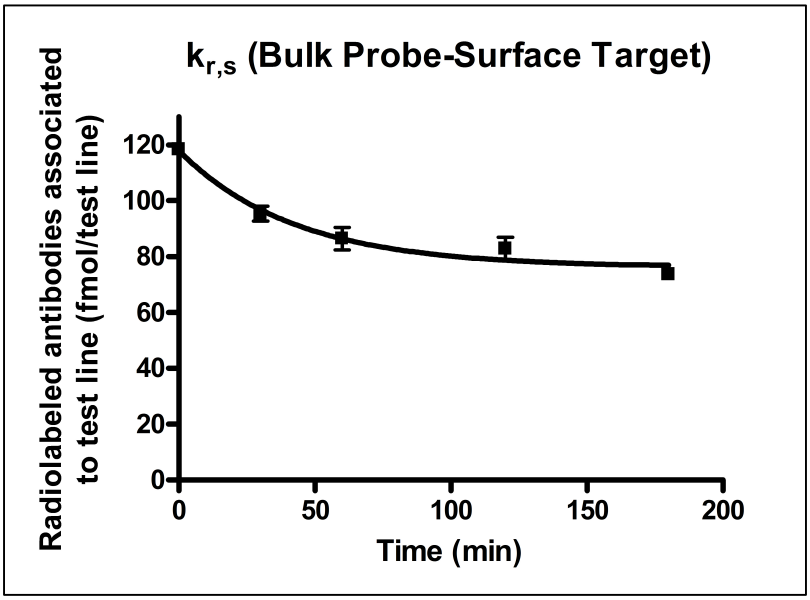

Figure 2-3. Determining $k_{r,s}$ for DGNP (probe) dissociating from the Tf on the test line (surface target). Remaining radiolabeled DGNPs that are bound to the test line at varying points in time. Time points were taken after the test lines were nearly saturated with DGNPs and the test strips had been switched to the solution containing excess non-radiolabeled Tf. The trend line was determined using non-linear regression in the form of an exponential decay with GraphPad. Error bars represent the standard error of the mean.

2.4.2.3 Determining $k_{f,s}$ for DGNP (probe) binding to an immobilized Tf on the test line (surface target)

To experimentally determine $k_{f,s}$, a solution of radiolabeled probe was flowed over the test strip and the amount of probe bound to the test line was measured at varying points in time. Under these conditions, **Eq. (14)** applies. However, we also discovered that the concentration of the bulk probe (P_b) does not significantly vary as the solution flows over the test line. As shown in **Table 2-2** the percentage of total probe that bound to the test line varied from 4.3% to 5.1% over the three different initial bulk probe concentrations tested. Since this percentage was low, we assumed that the concentration of bulk probe remained

constant as the solution flowed over the test line and that it was approximately equal to the initial concentration of bulk probe.

Table 2-2. Validating constant probe assumption. Quantification of the percentrage of DGNPs that bound to the test line for varying concentrations of probe.

DGNP Concentration (nM)	Total DGNPs (fmol)	Bound DGNPs (fmol)	Bound DGNPs (%)
1.29	90.5	3.89	4.3
5.03	352	18.3	5.2
9.91	694	35.4	5.1

Accordingly, the bulk probe concentration in **Eq. (14)** was set equal to a constant at the value corresponding to the initial concentration of bulk probe, which is denoted $P_{b,0}$. The available surface target concentration was also rewritten in terms of the complex concentration, where $T_s=T_{s,0}-P_s$, and $T_{s,0}$ is the total concentration of target immobilized on the test line in units of (moles/test line), which was experimentally determined using methods described earlier. **Equation (14)** therefore is given by:

$$\frac{d\left(nP_s\right)}{dt} = 2n^2 k_{f,s} P_{b,0}\left(T_{s,0} - P_s\right) - nk_{r,s}P_s \tag{18}$$

This equation can also be solved analytically, and the initial condition $P_s(0)=0$ can be applied. We know that $P_s(0)=0$ as there are no complexes formed initially as the experiment begins with no probe bound to the test line. With this initial condition, the solution to **Eq. (18)** is the following:

$$nP_s = \frac{2n^2 k_{f,s} P_{b,0} T_{s,0}}{2nk_{f,s}P_{b,0} + k_{r,s}}\left(1 - e^{-\left(2nk_{f,s}P_{b,0}+k_{r,s}\right)t}\right) \tag{19}$$

As shown in **Fig. 2-4**, an exponential increase was observed for the number of complexes as a function of time. Non-linear regression of the data with a one-phase exponential association using GraphPad yielded the following equation (R^2=0.88):

$$Y = 8.38 \cdot 10^{-14}\left(1 - e^{-\left(9.47 \cdot 10^{-4}\right)t}\right) \tag{20}$$

Accordingly, there are 2 methods to solve for $k_{f,s}$. The first method involves using the argument of the exponential from the non-linear regression (3.79×10^{-3}), and setting it equal to the argument of the exponential in **Eq. (19)**:

$$9.47 \cdot 10^{-4} = 2nk_{f,s}P_{b,0} + k_{r,s} \tag{21}$$

This method required knowledge of $k_{r,s}$ and $P_{b,0}$. The value of $k_{r,s}$ was experimentally determined in the previous section, and the value of the initial bulk probe concentration $P_{b,0}$ was found to be 9.85×10^{-8} M using methods described earlier. With these values, $k_{f,s}$ was determined with the first method to be 7.26×10^{2} $s^{-1}M^{-1}$.

On the other hand, the second method involved first setting the pre-exponential value in **Eq. (20)** (8.38×10^{-14}) equal to the pre-exponential expression in **Eq. (19)**:

$$8.38 \cdot 10^{-14} = \frac{2n^2k_{f,s}P_{b,0}T_{s,0}}{2nk_{f,s}P_{b,0} + k_{r,s}} \tag{22}$$

This was further simplified by substituting **Eq. (21)** in for the denominator in **Eq. (22)**, and rearranging to yield:

$$7.94 \cdot 10^{-17} = 2n^2k_{f,s}P_{b,0}T_{s,0} \tag{23}$$

This method required knowledge of $P_{b,0}$ and $T_{s,0}$. As previously mentioned, the molar concentration of $P_{b,0}$ was determined to be 9.85×10^{-8} M. The total concentration of receptor printed on the test line $T_{s,0}$ was also determined using methods described earlier and found

to be equal to $4.40x10^{-14}$ (moles/test line). With these values, the value of $k_{f,s}$ was determined with the second method to be $5.72x10^{2}$ $s^{-1}M^{-1}$, which was close to the value determined with the second method. The average value of these two methods, $6.50x10^{2}$ $s^{-1}M^{-1}$, was used as the value of $k_{f,s}$.

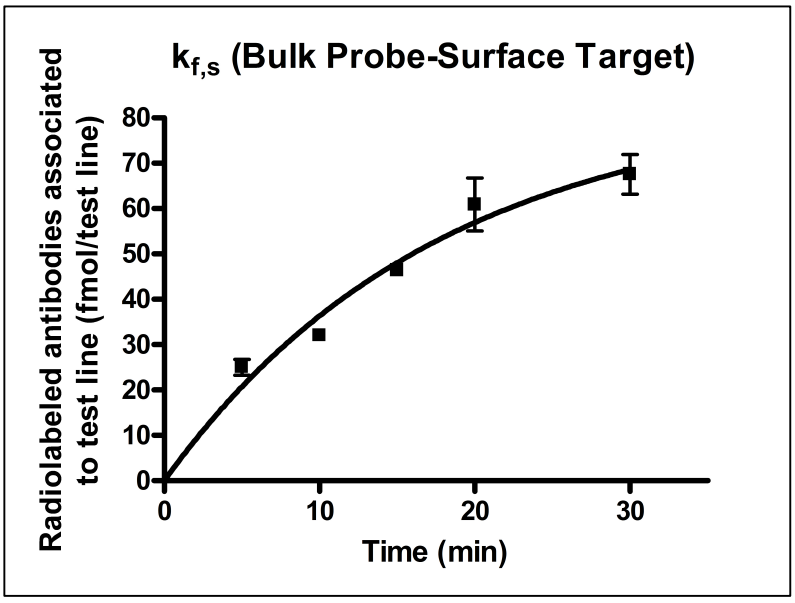

Figure 2-4. Determining $k_{f,s}$ for DGNP (probe) binding to the Tf on the test line (surface target). Radiolabeled DGNPs that are bound to the test line at varying points in time. Time point 0 represents when the DGNP suspension first reached the test line. The trend line was determined using non-linear regression in the form of a one-phase exponential association in GraphPad. Error bars represent the standard error of the mean.

2.4.2.4 Comparison of novel paper-based experimental results to traditional methods

An important aspect of our methods for determining the rate constants $k_{f,s}$ and $k_{r,s}$ is that they capture the interactions between the probe and the nitrocellulose membrane of the LFA test strip. To demonstrate this significance, these values were compared to the forward rate constant ($k_{f,b}$) and reverse rate constant ($k_{r,b}$) determined from more traditional

methods that examine the binding interaction in a non-native environment (i.e., the experiment is not performed within a nitrocellulose membrane with immobilized target).

Let us first consider binding of free target molecules in the bulk solution to individual antibody binding sites on probes in the bulk solution, where the probe has n number of antibodies on its surface. We treat each antibody binding site as being distinguishable so that there are separate probe concentrations for each binding permutation represented by $P_{b[symbols]}$ where the symbols within the brackets denote the unique sites that are occupied. For example, $P_{b[\alpha,\beta]}$ represents the concentration of probe with binding sites α and β occupied by target molecules. **Figure 2-5** illustrates an example scenario where the probe has 4 available binding sites. Note that we model the two binding sites of each antibody by treating each binding site as an independent interaction and assuming no cooperativity in binding (a standard assumption with antibody binding).

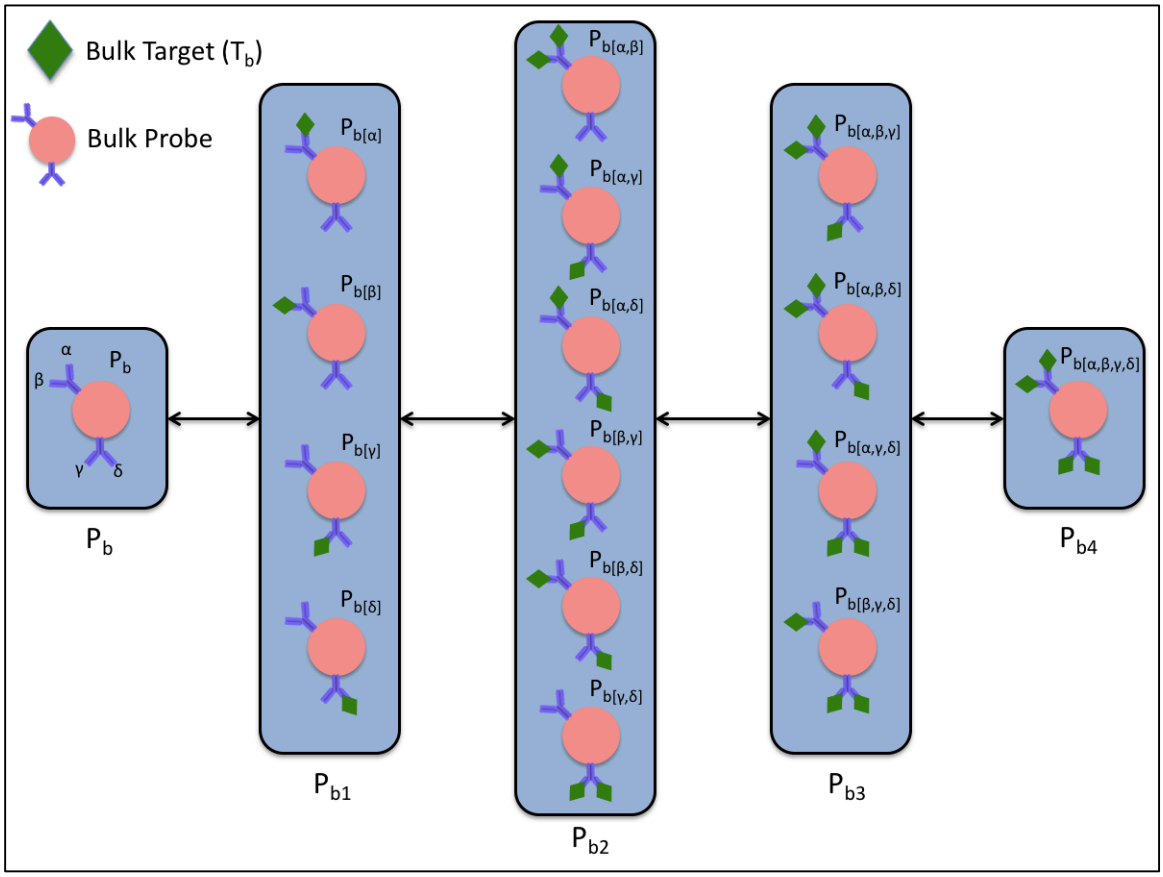

Figure 2-5. Schematic of bulk probe binding to bulk target. The schematic depicts the binding between a bulk probe (P_b) with 4 antibody binding sites (i.e., n=2 antibodies bound) to bulk target (T_b). Each antibody binding site is distinguishable by location, thus demonstrating the 16 possible binding permutations ($P_{b[symbols]}$) for this example. Each binding interaction is governed by the rate constants $k_{r,b}$ and $k_{f,b}$. The summation of the probe species with a given number of bound targets is represented as P_{bj}, where j is the number of bound targets. Note that this schematic depicts probes with 4 antibody binding sites for the purpose of clarity; however, the probes used during the experimental procedures had 8 antibody binding sites.

Each transition from one unique bound state to another can be described by expressions of rates of formation (**Eq. (24)**) and disappearance (**Eq. (25)**):

$$k_{f,b} P_{b[symbols]} T_b \tag{24}$$

$$k_{r,b} P_{b[symbols]} \tag{25}$$

where $P_{b[symbols]}$ is the molar concentration of the unique probe species that is undergoing the transition, T_b is the molar concentration of target in the bulk suspension, and $k_{f,b}$ and $k_{r,b}$ are the forward and reverse binding rate constants, respectively.

We assume each antibody site has equal binding affinity for the target. This allows us to treat each unique probe species with a given amount of bound target as having equal concentrations, which will be denoted as $P_{b[j]}$ where j is the total number of target molecules bound to the antibody sites, and j ranges from 0 to 2n. For example, $P_{b[\alpha,\beta,\gamma,]}$, $P_{b[\alpha,\beta,\delta]}$, $P_{b[\alpha,\gamma,\delta]}$, and $P_{b[\beta,\gamma,\delta]}$ have equal concentration values, and each of these concentrations is represented as $P_{b[3]}$. The rate of change of any given unique probe species $P_{b[j]}$ is a summation of the rates of formation and disappearance for its transitions between the other unique probe species, which can be mathematically represented as follows:

$$\frac{dP_{b[j]}}{dt} = jk_{f,b}P_{b[j-1]}T_b - jk_{r,b}P_{b[j]} - (2n-j)k_{f,b}P_{b[j]}T_b + (2n-j)k_{r,b}P_{b[j+1]} \tag{26}$$

where j is the number of bound antibody sites, (2n-j) is the number of available antibody sites after j sites are bound, n is the total number of antibodies per probe, $P_{b[j]}$, $P_{b[j-1]}$, and $P_{b[j+1]}$ are the molar concentrations of unique probe species with j, j-1, and j+1 number of targets bound, respectively, and T_b is the molar concentration of target in the bulk solution.

Considering that the concentration of each unique probe species $P_{b[j]}$ is equal to each other for a given number of bound targets j (e.g., $P_{b[\alpha,\beta,\gamma,]} = P_{b[\alpha,\beta,\delta]} = P_{b[\alpha,\gamma,\delta]} = P_{b[\beta,\gamma,\delta]} = P_{b[3]}$), the summation of all the $P_{b[j]}$ values for a given j can be mathematically described by multiplying by the number of binding permutations:

$$P_{bj} = \frac{(2n)!}{(2n-j)!\,j!} \cdot P_{b[j]} \tag{27}$$

where P_{bj} is the sum of all $P_{b[j]}$ species concentrations for a given j value, i.e., the cumulative concentration for each j value. The total number of permutations is equal to the total number of bound states with the same energy, i.e., the degeneracy, and it is equal to the binomial coefficient of 2n choose j. Using **Eq. (27)**, several equations can be developed for the unique probe species $P_{b[j]}$, $P_{b[j-1]}$, and $P_{b[j+1]}$ to describe them in terms of their corresponding cumulative concentrations P_{bj}, P_{bj-1}, and P_{bj+1}, respectively:

$$P_{b[j]} = \frac{P_{bj}}{\left(\frac{(2n)!}{(2n-j)!\,j!}\right)} \tag{28}$$

$$P_{b[j-1]} = \frac{P_{bj-1}}{\left(\frac{(2n)!}{(2n-(j-1))!(j-1)!}\right)} \tag{29}$$

$$P_{b[j+1]} = \frac{P_{bj+1}}{\left(\frac{(2n)!}{(2n-(j+1))!(j+1)!}\right)} \tag{30}$$

Equation (26) can now be written in terms of the cumulative concentrations by substituting in **Eqs. (28)**, **(29)**, and **(30)** to yield:

$$\frac{dP_{b[j]}}{dt} = jk_{f,b}T_b \frac{P_{bj-1}}{\frac{(2n)!}{(2n-(j-1))!(j-1)!}} - jk_{r,b}\frac{P_{bj}}{\frac{(2n)!}{(2n-j)!\,j!}}$$

$$-(2n-j)k_{f,b}T_b \frac{P_{bj}}{\frac{(2n)!}{(2n-j)!\,j!}} + (2n-j)k_{r,b}\frac{P_{bj+1}}{\frac{(2n)!}{(2n-(j+1))!(j+1)!}} \tag{31}$$

We can now derive the rate of change for the cumulative concentration of probe for a given number of bound targets j by taking the derivative of **Eq. (27)** with respect to time and substituting in **Eq. (31)**. After simplifying, the equation is given by:

$$\frac{dP_{bj}}{dt} = \left(2n-\left(j-1\right)\right)k_{f,b}T_bP_{bj-1} - jk_{r,b}P_{bj} - \left(2n-j\right)k_{f,b}T_bP_{bj} + \left(j+1\right)k_{r,b}P_{bj+1} \tag{32}$$

which holds true when (1≤j≤2n-1). The j=0 and j=2n expressions cannot be represented by the above equation as they represent completely unbound probe and completely bound probe, respectively. Specifically, the rates of change for bound target values of j=0 and j=2n can be written as:

$$\frac{dP_b}{dt} = -2nk_{f,b}T_bP_b + k_{r,b}P_{b1} \tag{33}$$

$$\frac{dP_{b2n}}{dt} = k_{f,b}T_bP_{b2n-1} - 2nk_{r,b}P_{b2n} \tag{34}$$

To experimentally determine the rate constants, radiolabeled Tf is used to quantify the change in molar concentration of total target bound to the antibody binding sites at varying points in time. This measurement can be described mathematically as a summation of the rates of change of the cumulative probe species concentrations from **Eqs. (32)**, **(33)** , and **(34)**, multiplied by their respective number of targets bound j:

$$\frac{d\left(\sum_{j=0}^{2n} jP_{bj}\right)}{dt} = 2n\left(k_{f,b}T_bP_{b2n-1} - 2nk_{r,b}P_{b2n}\right) + 0\left(-2nk_{f,b}T_bP_b + k_{r,b}P_{b1}\right) +$$

$$\sum_{j=1}^{2n-1}\left(j\left(\left(2n-\left(j-1\right)\right)k_{f,b}T_bP_{bj-1} - jk_{r,b}P_{bj} - \left(2n-j\right)k_{f,b}T_bP_{bj} + \left(j+1\right)k_{r,b}P_{bj+1}\right)\right) \tag{35}$$

Equation (35) can be simplified to:

$$\frac{d\left(\sum_{j=0}^{2n} jP_{bj}\right)}{dt} = k_{f,b}T_b\left(\sum_{j=0}^{2n} 2nP_{bj} - \sum_{j=0}^{2n} jP_{bj}\right) - k_{r,b}\left(\sum_{j=0}^{2n} jP_{bj}\right) \tag{36}$$

The first summation on the right-hand side of **Eq. (36)** represents the total molar concentration of antibody binding sites (available and bound) within the solution, which we will denote as A_0. The remaining summations in **Eq. (36)** represent the total molar concentration of bound antibody binding sites within the suspension, which we will denote as B. Making these notation substitutions, **Eq. (36)** is given by:

$$\frac{dB}{dt} = k_{f,b}T_b\left(A_0 - B\right) - k_{r,b}B \tag{37}$$

Equation (37) can be used to calculate the binding rate constants for our specific experimental designs.

2.4.2.5 Determining $k_{r,b}$ for Tf (bulk target) binding to an antibody on DGNP (bulk probe)

To experimentally determine $k_{r,b}$, a high concentration of radiolabeled Tf was initially incubated with the DGNPs. After near saturation, the DGNPs were transferred to a solution with a high concentration of non-radiolabeled Tf. Under these conditions, any dissociated radiolabeled Tf molecules were not able to rebind to the DGNPs as the unlabeled Tf would outcompete the radiolabeled Tf for binding to the available anti-Tf antibodies on the DGNPs. **Equation (37)** therefore simplifies for this experiment to the following expression:

$$\frac{dB}{dt} = -k_{r,b}B \tag{38}$$

where B represents antibody sites bound to radiolabeled (not unlabeled) target. This equation can be analytically solved, and the initial condition $B(0)=B_0$ can be applied to yield the following solution:

$$B = B_0 e^{-k_{r,b}t} \tag{39}$$

As shown in **Fig. 2-6**, an exponential decay was observed for the concentration of bound target as a function of time. Non-linear regression of the data with an exponential decay using GraphPad yielded the following equation (R^2=.98):

$$Y = 4.94 \cdot 10^{-9}\left(e^{-\left(2.17 \cdot 10^{-4}\right)t}\right) + 1.19 \cdot 10^{-9} \tag{40}$$

Equation Error! Reference source not found. has a constant offset of 1.19×10^{-9} due to irreversible nonspecific binding. This does not alter the evaluation of the rate constant since $k_{r,b}$ is in the argument of the exponential. Comparing the arguments of the exponential between **Eqs. (39)** and Error! Reference source not found. yields a value of 2.17×10^{-4} s^{-1} for $k_{r,b}$.

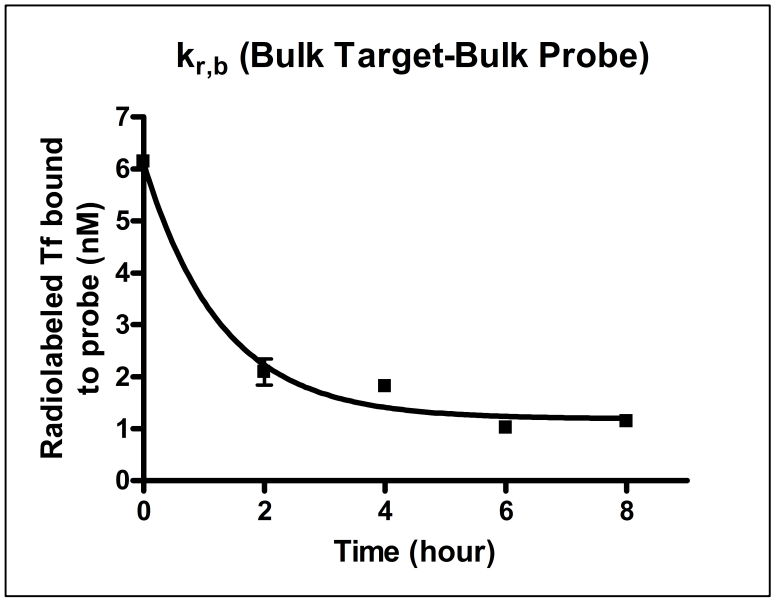

Figure 2-6. Determining $k_{r,b}$ for Tf (bulk target) dissociating from antibody on DGNP (probe). Remaining radiolabeled Tf molecules that are bound to the probe-bound antibody binding sites at varying points in time. Time points were taken after the antibody binding sites were nearly saturated with Tf and the DGNPs had been switched to the solution containing non-radiolabeled Tf. The trend line was determined using non-linear regression in the form of an exponential decay using GraphPad. Error bars represent the standard error of the mean.

2.4.2.6 Determining $k_{f,b}$ for Tf (bulk target) binding to an antibody on DGNP (bulk probe)

To experimentally determine $k_{f,b}$, time points were taken as soon as the radiolabeled bulk target was introduced to the probe solution. Under these conditions, **Eq. (37)** is applicable. In addition, we discovered that the concentration of the bulk target should not significantly vary during this experiment. As shown in **Table 2-3**, for a separate experimental study involving much longer incubation times, the percentage of total Tf molecules that bound to the antibodies on the DGNPs varied from 8.0% to 9.6% over the three different initial bulk target concentrations tested. Since this percentage was not too

significant, we assumed that the concentration of free bulk target remained constant during this experiment and that it was approximately equal to the initial concentration of Tf.

Table 2-3. Validating constant target assumption. Quantification of the percentage of radiolabeled Tf that bound to the antibody binding sites on the probe over varying initial concentrations of Tf.

Total Tf (nM)	Bound Tf (nM)	Bound Tf (%)
2.6	0.25	9.6%
3.8	0.33	8.7%
5.0	0.40	8.0%

Accordingly, the bulk Tf concentration in **Eq. (37)** was set equal to a constant at the value corresponding to the initial concentration of bulk Tf, which is denoted $T_{b,0}$. **Equation (37)** therefore becomes:

$$\frac{dB}{dt} = k_{f,b} T_{b,0} \left(A_0 - B \right) - k_{r,b} B \tag{41}$$

This equation was also solved analytically, and the initial condition B(0)=0 was applied. We know that B(0)=0 as the experiment begins with no Tf molecules bound to the antibodies on the DGNPs. With this initial condition, the solution to **Eq. (41)** is the following:

$$B = \frac{k_{f,b} T_{b,0} A_0}{k_{f,b} T_{b,0} + k_{r,b}} \left(1 - e^{-\left(k_{f,b} T_{b,0} + k_{r,b} \right) t} \right) \tag{42}$$

As shown in **Fig. 2-7**, an exponential increase was observed for the number of bound antibody sites as a function of time. Non-linear regression of the data with an exponential increase using GraphPad yielded the following equation (R^2=.80):

$$Y = 1.18 \cdot 10^{-8} \left(1 - e^{-\left(8.92 \cdot 10^{-4}\right)t}\right) \tag{43}$$

Accordingly, there are also 2 methods to solve for $k_{f,b}$. However, since $T_{b,0}$ is straightforward to calculate by using the specific activity from the PTA assay, we used a method analogous to the first method described earlier for solving $k_{f,s}$ to algebraically evaluate $k_{f,b}$. Specifically, the first method involves using the argument of the exponential from the non-linear regression (8.92×10^{-4}), and setting it equal to the argument of the exponential in **Eq. (42)**:

$$8.92 \cdot 10^{-4} = k_{f,b} T_{b,0} + k_{r,b} \tag{44}$$

This method required knowledge of $k_{r,b}$ and $T_{b,0}$. The value of $k_{r,b}$ was experimentally determined in the previous section, and the value of the initial ligand concentration $T_{b,0}$ was found to be 1.19×10^{-9} M. With these values, the value of $k_{f,b}$ was determined with the method to be 5.67×10^{5} $M^{-1}s^{-1}$.

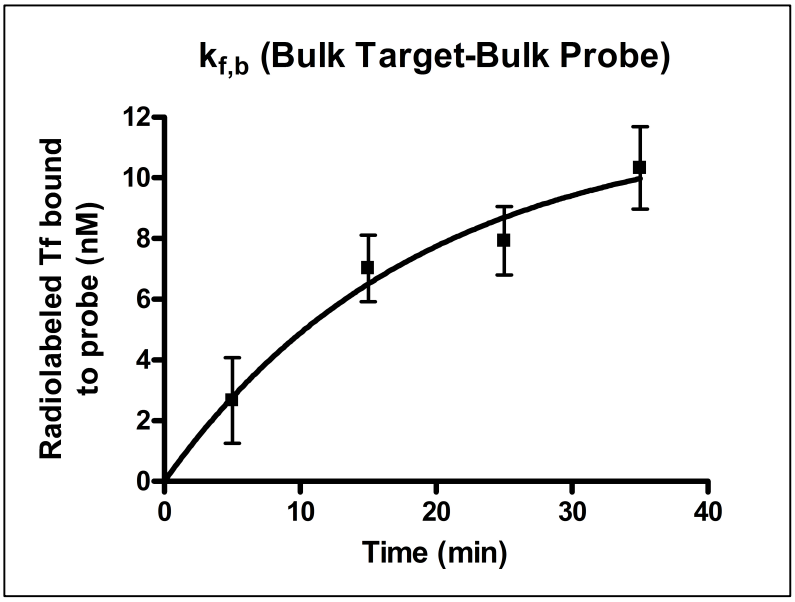

Figure 2-7. Determining $k_{f,b}$ for Tf (bulk target) binding to an antibody on DGNP (probe). Radiolabeled Tf molecules that are bound to the antibody binding sites on the probe at varying points in time. Time point 0 represents when the Tf was first mixed with the DGNP suspension. The trend line was determined using non-linear regression in the form of a one-phase exponential association using GraphPad. Error bars represent the standard error of the mean.

Comparison of the rate constant values reveals an interesting correlation between the two experimental methods. The reverse rate constants for the paper-based and traditional experiments are relatively similar, with values of 3.75×10^{-4} and 2.17×10^{-4} s^{-1}, respectively. However, the values for the forward rate constants differ by more than 2 orders of magnitude, with values of 6.50×10^{2} and 5.67×10^{5} $M^{-1}s^{-1}$ for the paper-based and traditional methods, respectively. This intuitively makes sense considering interactions between the probe and nitrocellulose membrane may hinder the accessibility of the antibody on the probe associating with the immobilized target, which is only accurately captured by the paper-based experiments. However, once bound, the process of unbinding is solely based on the protein-protein interactions, which is accurately captured by both experimental procedures.

This comparison demonstrates the usefulness of obtaining probe binding rate constants using our novel experimental methods performed within nitrocellulose membranes. These methods can more efficiently guide LFA research and diagnostic design. Using the model system as an example, we see that the best approach to improving diagnostic performance may not be through improving the antibody binding affinity, but rather to explore different paper and probe designs. Not only can our experimental procedure more accurately determine the binding rates constants for interactions between the probe and immobilized target, but it also can serve as the basis for further experimentation to elucidate mechanisms of poor binding.

2.4.3 Determining the volumetric flow rate (Q) and the fluid volume in the test line (v) for the LFA test strip

2.4.3.1 Determining volumetric flow rate (Q)

Using materials available from the previous experiments, the volumetric flow rate (Q) for the LFA test strip was straightforward to determine. Volumetric flow rate is not difficult to obtain from conventional methods, which involve measuring the mass of the fluid that has flowed onto the test strip. However, a modified method was used in this work that incorporated our radioactivity data. To determine volumetric flow rate, a solution of radiolabeled Tf was flowed along multiple test strips. At varying points in time, radioactivity measurements were taken of the solution remaining that had not flowed onto the test strip. This was used to calculate the volume that had flowed using the radioactivity per volume of the Tf solution. Linear regression of the data (R^2=.99) shown in **Fig. 2-8**

gives a slope of 4.4 μL/min. Note that the trend line intersects the y-axis at a value above 0. This corresponds to the initial submersion of the leading edge of the test strip into the solution which results in an almost instantaneous absorption of a small amount of fluid into the test strip.

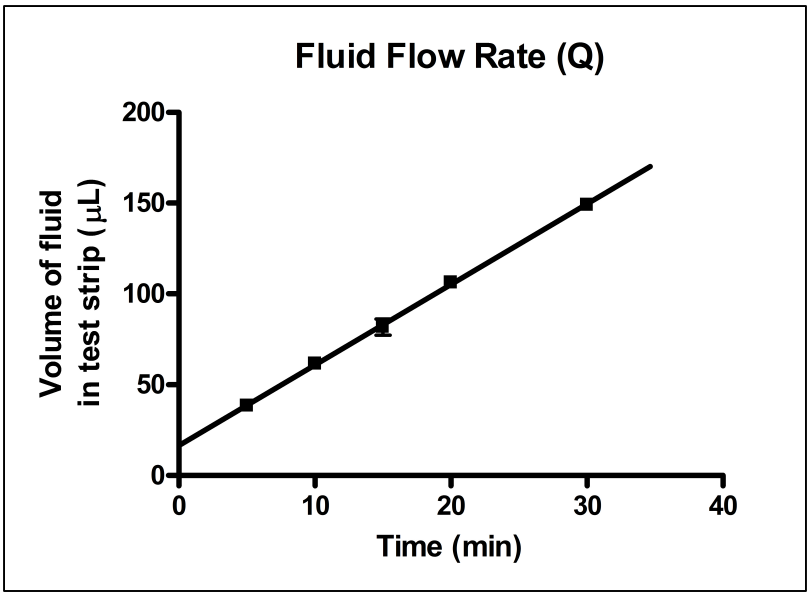

Figure 2-8. Determining fluid flow rate Q within the test strip. Volume of fluid that has flowed onto the test strip at varying points in time.

2.4.3.2 Determining fluid volume within the test line ν

Similar to determining the volumetric flow rate, the radioactivity per volume of the radiolabeled Tf solution was utilized to determine the fluid volume within the test line. To determine ν, a radiolabeled Tf solution was flowed along a bare nitrocellulose membrane (i.e., containing no immobilized protein). By measuring the radioactivity of known areas of membrane, the volume per area of membrane was calculated to be 8.2 μL/cm^2. The area

of the test line on the membrane was measured, and the volume per test line was determined to be $\nu = 0.25\ \mu L$.

2.5 Conclusions

As LFA diagnostics become increasingly complex, it is useful to accurately determine important LFA parameters in order to quantitatively compare different designs and to provide a deeper understanding of the diagnostic components. In this study, we have developed several novel experimental procedures that combine the use of paper and radioactivity, and demonstrated their application with a model LFA system. First, we developed a novel method for calculating the molarity of a colorimetric nanoprobe solution, which is robust enough to determine molarity regardless of the probe structure or composition, and is also not confounded by the presence of bare nanoparticles. These experiments were also used to calculate the number of antibodies per probe. Additionally, we developed a novel process to determine the forward and reverse rate constants for the interaction between a colorimetric probe and the immobilized target on an LFA test line. This procedure uses conditions that exactly mimic the LFA membrane environment, which more appropriately captures any effect that the LFA system has on binding. By comparing these rate constant values with those obtained from more traditional experiments, it was found that the interaction between the probe and the nitrocellulose membrane negatively affects the forward binding rate constant, demonstrating how our novel paper-based experiment can be used to elucidate mechanisms for poor binding and thus more informatively guide the LFA design process. Furthermore, the mathematical analysis

required for our methods was provided, and the assumptions made during the analysis were experimentally validated. Finally, it was demonstrated how the materials from the previous experiments can be used to determined the volumetric flow rate of an LFA test strip, as well as the fluid volume within the test line. The methods described in this work provide a basic toolset specifically designed to improve the efficiency of LFA research and to evaluate LFA-based diagnostics. However, these techniques may certainly have unique applications outside of LFA research, and may have significant potential in fields outside of LFA.

3 Mathematical Model for Predicting Probe Binding to the Test Line

3.1 Motivation and Background

As the field of paper-based diagnostics continues to rapidly expand, it becomes more important to incorporate modeling into their design. A model can be used to determine the effects of LFA parameters on desired outputs, such as the amount of probe bound to the test line. Such predictions become increasingly important as systems become more complicated, and the effects of changing different operating conditions become less intuitive due to the many physical, chemical, and biological processes that are simultaneously occurring. Moreover, a mathematical model allows the engineer to quantitatively predict the influence of well-defined changes in certain parameters. A recent review of the sate of LFA modeling describes the importance of reliable LFA models in order to develop quantitative LFA tests[55]. Although several theoretical[56,57] and computational[58–60] models for LFA exist, we decided to derive a simple model that could be used in combination with our novel estimation methods for LFA parameters (Chapter 2) to predict the amount of probe binding to the test line, an important performance indicator of LFA. This chapter discusses the derivation of the model, along with our methods to experimentally determine additional parameters required by the model.

3.2 Materials and Methods

3.2.1 Derivation of the mathematical model using principles of mass-action kinetics

Other research groups have developed relatively sophisticated mathematical and computational models of LFA[56–60]. For our purposes, we decided to develop a simplified 2 step model to predict the amount of DGNPs (probes) bound to the test line in response to varying initial concentrations of the target Tf. Such a correlation would be beneficial in helping design a competition LFA test as LFA parameters could be manipulated theoretically to determine their effects on the amount of DGNP bound to the test line. In this model, the 1st step captures the binding of the free Tf target to the antibodies on the probe, while the 2nd step captures the binding of the free antibodies on the probe to the immobilized free Tf target molecules on the test line.

3.2.1.1 Step 1: Binding of the free Tf target molecules to the antibodies on DGNPs (probes)

Step 1 is treated as taking place in a well-mixed solution for a time period that corresponds to the experimentally determined time that the probes spend with the target molecule before the solution reaches the test line. This time includes any incubation time before adding the test strip to the solution as well as the time it takes for the solution to flow along the strip to reach the test line. We model the system by writing a species balance for each bound state of the probe. Two key parameters in these species balances are (i) the rate constant $k_{f,b}$ for free Tf (ligand) binding to an antibody on DGNP (probe) and (ii) the rate constant $k_{r,b}$ for Tf (ligand) dissociating from an antibody on DGNP (probe). These rate constants were determined in Chapter 2. These $k_{f,b}$ and $k_{r,b}$ rate constants were incorporated into each species balance and multiplied by the number of free antibodies or bound antibodies per probe, respectively. For our system, we showed in Chapter 2 how we

can determine the concentrations of DGNP and the number of antibodies per DGNP. For our experiments in Chapter 2, we found that there were 3.93 total antibodies conjugated per probe on average, so we rounded up to 4 total antibodies conjugated per probe. We solved the following system of ordinary differential equations (ODEs) representing Step 1 for a given initial target concentration T_b and for a given incubation time:

$$\frac{dP_{b,0}}{dt} = k_{r,b}P_{b,1} - 8k_{f,b}P_{b,0}T_b \tag{45}$$

$$\frac{dP_{b,1}}{dt} = 2k_{r,b}P_{b,2} - 7k_{f,b}P_{b,1}T_b - k_{r,b}P_{b,1} + 8k_{f,b}P_{b,0}T_b \tag{46}$$

$$\frac{dP_{b,2}}{dt} = 3k_{r,b}P_{b,3} - 6k_{f,b}P_{b,2}T_b - 2k_{r,b}P_{b,2} + 7k_{f,b}P_{b,1}T_b \tag{47}$$

$$\frac{dP_{b,3}}{dt} = 4k_{r,b}P_{b,4} - 5k_{f,b}P_{b,3}T_b - 3k_{r,b}P_{b,3} + 6k_{f,b}P_{b,2}T_b \tag{48}$$

$$\frac{dP_{b,4}}{dt} = 5k_{r,b}P_{b,5} - 4k_{f,b}P_{b,4}T_b - 4k_{r,b}P_{b,4} + 5k_{f,b}P_{b,3}T_b \tag{49}$$

$$\frac{dP_{b,5}}{dt} = 6k_{r,b}P_{b,6} - 3k_{f,b}P_{b,5}T_b - 5k_{r,b}P_{b,5} + 4k_{f,b}P_{b,4}T_b \tag{50}$$

$$\frac{dP_{b,6}}{dt} = 7k_{r,b}P_{b,7} - 2k_{f,b}P_{b,6}T_b - 6k_{r,b}P_{b,6} + 3k_{f,b}P_{b,5}T_b \tag{51}$$

$$\frac{dP_{b,7}}{dt} = 8k_{r,b}P_{b,8} - k_{f,b}P_{b,7}T_b - 7k_{r,b}P_{b,7} + 2k_{f,b}P_{b,6}T_b \tag{52}$$

$$\frac{dP_{b,8}}{dt} = -8k_{r,b}P_{b,8} + k_{f,b}P_{b,7}T_b \tag{53}$$

$$T_b = T_{b,0} - P_{b,1} - P_{b,2} - P_{b,3} - P_{b,4} - P_{b,5} - P_{b,6} - P_{b,7} - P_{b,8} \tag{54}$$

where $P_{b,0}$, $P_{b,1}$, $P_{b,2}$, $P_{b,3}$, $P_{b,4}$, $P_{b,5}$, $P_{b,6}$, $P_{b,7}$, and $P_{b,8}$ represent probes with 0, 1, 2, 3, 4, 5, 6, 7, and 8 ligand molecules bound, respectively. T_b is the free Tf (ligand) concentration at any time t. The time spent in Step 1 is the sum of the incubation time and the time it takes to flow from the bulk solution to the test line. The solution of the ODEs also requires the initial Tf target concentration $T_{b,0}$ and the initial probe concentration $P_{b,0}(t=0)$. This system of ODEs was solved using ode23s in MATLAB for the appropriate period of time. The concentrations of the probes at varying points in time were used as the initial conditions for Step 2.

3.2.1.2 Step 2: Binding of the free antibodies on DGNPs (probes) to the free Tf molecules immobilized on the test line

Step 2 is also treated as taking place in a well-mixed solution. The time period for Step 2 corresponds to the time the solution spends in the test line region, which we determined as described at the end of this section. We again derived species balances, but in this case, for the complexes formed between a free Tf immobilized on the test line (T_s) and a free antibody on DGNP (probe). Two key parameters in these species balances are (i) the rate constant $k_{f,s}$ for free antibody on a DGNP (probe) binding to a free Tf molecule immobilized on the test line (receptor) and (ii) the rate constant $k_{r,s}$ for an antibody on a DGNP (probe) dissociating from a Tf molecule immobilized on the test line. These rate constants were determined in Chapter 2, and the ODEs are written below:

$$\frac{dP_{s,0}}{dt} = 8k_{f,s}P_{b,0}T_s - k_{r,s}P_{s,0} \tag{55}$$

$$\frac{dP_{s,1}}{dt} = 7k_{f,s}P_{b,1}T_s - k_{r,s}P_{s,1} \tag{56}$$

$$\frac{dP_{s,2}}{dt} = 6k_{f,s}P_{b,2}T_s - k_{r,s}P_{s,2} \tag{57}$$

$$\frac{dP_{s,3}}{dt} = 5k_{f,s}P_{b,3}T_s - k_{r,s}P_{s,3} \tag{58}$$

$$\frac{dP_{s,4}}{dt} = 4k_{f,s}P_{b,4}T_s - k_{r,s}P_{s,4} \tag{59}$$

$$\frac{dP_{s,5}}{dt} = 3k_{f,s}P_{b,5}T_s - k_{r,s}P_{s,5} \tag{60}$$

$$\frac{dP_{s,6}}{dt} = 2k_{f,s}P_{b,6}T_s - k_{r,s}P_{s,6} \tag{61}$$

$$\frac{dP_{s,7}}{dt} = k_{f,s}P_{b,7}T_s - k_{r,s}P_{s,7} \tag{62}$$

$$T_s = T_{s,0} - P_{s,0} - P_{s,1} - P_{s,2} - P_{s,3} - P_{s,4} - P_{s,5} - P_{s,6} - P_{s,7} \tag{63}$$

where T_s is the number of available Tf on the test line, $T_{s,0}$ is the initial number of Tf on the test line, and $P_{s,0}$, $P_{s,1}$, $P_{s,2}$, $P_{s,3}$, $P_{s,4}$, $P_{s,5}$, $P_{s,6}$, and $P_{s,7}$ represent the complexes formed between T_s and $P_{b,0}$, $P_{b,1}$, $P_{b,2}$, $P_{b,3}$, $P_{b,4}$, $P_{b,5}$, $P_{b,6}$, and $P_{b,7}$ respectively. Note that there is no complex formed with $P_{b,8}$ since that probe does not have any free antibody sites to bind

to a free Tf that is immobilized. This system of ODEs was solved using ode23s in MATLAB for the appropriate period of time. The complexes were then summed to yield the total number of bound complexes in Step 2, and this represented the total amount of bound DGNP (probe) on the test line:

$$P_{s,total} = P_{s,0} + P_{s,1} + P_{s,2} + P_{s,3} + P_{s,4} + P_{s,5} + P_{s,6} + P_{s,7} \tag{64}$$

The duration of time corresponding to Step 2 was determined by taking the volume of the test line divided by the volumetric flow rate found in Chapter 2. The fluid volume in the test line was experimentally determined by first placing blank LFA test strips, i.e., membranes without immobilized test lines, into a solution of radiolabeled Tf. After the solution completely flowed across the nitrocellulose membrane, a known area of test strip was cut out. The radioactivity in this known area was measured with the gamma counter, and after dividing by the concentration of radiolabeled Tf in the solution, the volume in the known area (vol/cm^2) was determined. The fluid volume in a test line was then determined by first measuring the area of the test line and then dividing by the fluid volume/cm^2 parameter that was just determined. The information about the fluid volume of the test line region was also necessary to convert the probe concentrations.

3.2.1.3 Integrating Step 1 and Step 2

Some of the previous LFA models described in literature make the assumption that the target and probe binding reaches equilibrium prior to reaching the test line. Since the duration of time associated with this binding is short, we relaxed this assumption. Conceptually, we treated the entire solution as a series of discrete volumes. Each discrete

volume would be exposed to the test line sequentially, and therefore, each subsequent discrete volume would have a longer time allotted for bulk target binding to the probe.

The way this was accomplished in MATLAB was to create a script for the entire model that contained a *for loop*. The *for loop* would first run the Step 1 files, which would produce the concentrations of each of the probe species, and then subsequently run the Step 2 files, which would use the probe species concentrations and generate the concentration of each of the complex species. Each subsequent iteration of the *for loop* would lengthen the incubation time in Step 1. At the end of each iteration of the *for loop*, the concentrations of the complexes would be stored and used as the initial conditions in Step 2 of the subsequent *for loop* iteration. The entire MATLAB script can be viewed in the Appendix.

3.2.2 Preparation of competition LFA tests for detection of transferrin (Tf)

A competition LFA was utilized in this study. Tf was immobilized on a nitrocellulose membrane (Sartorius, Goettingen, Germany) to form the test line. This process was accomplished by dispensing a solution of 25% w/v sucrose and varying concentrations of Tf at a controlled rate using a syringe pump across the nitrocellulose membrane. In a competition LFA test, the colorimetric probe binds to the test line when no target is present, displaying a red line to indicate a negative test. As the concentration of target in the sample of interest increases, less probe binds to the test line until the target concentration is sufficient to prevent any visible binding, indicating a positive test. The nitrocellulose membrane was assembled with a sample pad (Whatman, Pittsburgh, PA) and an absorbent pad (Whatman, Pittsburgh, PA) using an adhesive backing (Whatman, Pittsburgh, PA), which is common practice for LFA. Many of the experiments required

measuring the radioactivity of the test line and subtracting out the background radioactivity signal. To accomplish this, the back of the LFA test was marked to indicate a 0.7 cm length which encompassed the test line. This length of paper was cut out and measured to represent the test line radioactivity. A separate 0.7 cm length located upstream of this position was also marked and measured to serve as the background radioactivity signal. All materials were purchased from Sigma-Aldrich unless otherwise noted.

3.2.3 Preparation of antibody-decorated dextran-coated gold nanoprobes (DGNPs)

LFA tests require a colorimetric indicator, typically in the form of a nanoparticle conjugated to a binding moiety. For these experiments, we used dextran-coated gold nanoparticles which were synthesized according to Min and coworkers with slight modifications.[54] Briefly, 6 g of dextran (Mw 15,000–25,000) from *Leuconostoc spp*. were dissolved in 80 mL of filtered UltraPure sterile water (Rockland Immunochemicals Inc., Gilbertsville, PA). The solution was stirred and heated to a boil, after which 1080 μL of a 1% w/v gold(III) chloride hydrate solution were added. The color of the reaction mixture turned reddish-violet and was stirred and boiled for about 20 min. The newly formed dextran-coated gold nanoparticles were centrifuged to remove free dextran and resuspended in 70 mL of water. To form functionalized DGNPs, the pH of the dextran-coated gold nanoparticle solution was adjusted to 9.0 using 1.5 M NaOH. For every 1 mL of dextran-coated gold nanoparticle solution, 8 μg of anti-Tf antibodies (Bethyl Laboratories, Montgomery, TX) were added. The reaction mixture was placed on a shaker for 30 min to facilitate the formation of dative bonds between the antibodies and the dextran-coated gold nanoparticles. Free antibodies were removed by centrifugation. The

pellet was resuspended in 100 μL of 0.1 M sodium borate buffer at pH 9.0, and these antibody-decorated dextran-coated gold nanoprobes will be referred to as DGNPs.

3.2.4 Radiolabeled antibodies and transferrin

Iodine-125 (^{125}I) was used to radiolabel the tyrosine residues of the goat anti-Tf antibody (Bethyl Laboratories, Montgomery, TX) and Tf. Briefly, $Na^{125}I$ (MP Biomedicals, Irvine, CA) was activated by IODO-BEADS (Pierce Biotechnology, Rockford, IL). Subsequently, the activated ^{125}I was reacted with 100 ! g of protein for 15 min. The radiolabeled antibodies were purified from free ^{125}I using a Sephadex G10 size-exclusion column. The specific activity and concentration of the radiolabeled antibodies were determined by a phosphotungstic acid (PTA) assay.

3.2.5 Validation of the model

To validate the model, we ran LFA tests at varying concentrations of target Tf and quantified the binding of the DGNPs to the test line. The Tf concentrations ranged from 1.25×10^{-11} M to 1.25×10^{-6} M in logarithmic intervals. 5uL of DGNPs conjugated with radiolabeled anti-Tf antibodies were added to the solutions of Tf in PBS. The entire suspension was allowed to flow along the test strip. After 15 minutes, the test lines were cut out and the radioactivity was measured. The radioactivity value was translated into DGNP concentration as described previously. These tests were run in triplicate. Background signal was determined to be the radioactivity value of the 1.25×10^{-6} M Tf condition, and that mean value was subtracted from the mean values of the other Tf conditions.

3.3 Results and Discussion

3.3.1 Examination of Step 1 and Step 2 predictions of the model

Before we combined Step 1 and Step 2 of the model together, we ran each step of the model separately and observed changes in the probe and complex concentrations for Step 1 and Step 2 of the model, respectively. These simulations were performed to determine if the predictions were physically intuitive. For simplicity, we considered a probe with 2 antibodies conjugated to its surface in these simulations, and therefore, 5 different probe species and 4 different complex species were possible.

For Step 1 of the MATLAB model, we varied the values of the parameters ($k_{f,b}$, $k_{r,b}$, $P_{b,0}$, and $T_{b,0}$) over a wide range of values. **Figure 3-1** shows the concentration of each probe species as a function of time from one of the simulations. We see that the concentration profiles of each of the probe species behaved as expected. Some examples of this include: (i) the completely unbound probe species starting at the high initial concentration equal to $P_{b,0}$, while the other probe species starting at 0 concentration, (ii) the concentration of a probe species with n targets bound starting to increase only after a significant population of probe with n-1 targets bound has developed, and (iii) given enough time, the concentration of each probe species reaching equilibrium. We observed these trends over a wide range of $k_{f,b}$, $k_{r,b}$, $P_{b,0}$, and $T_{b,0}$ values (data not shown) indicating that Step 1 of the model could predict physically intuitive results.

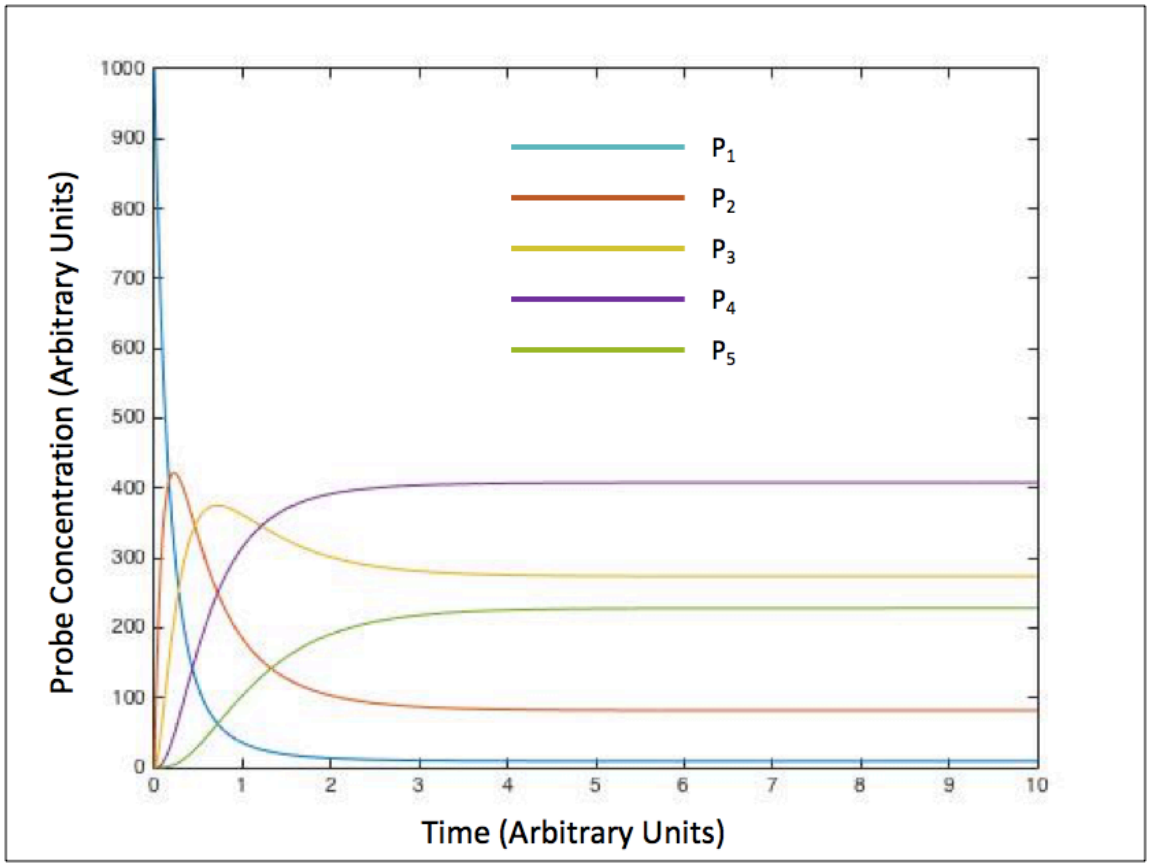

Figure 3-1. Results of Step 1 of the MATLAB model. The concentrations of each probe species with varying numbers of Tf bound were monitored over time using only the MATLAB scripts for Step 1 of the model. In this simulation, the probe was only modeled to have 2 antibodies and therefore a total of 4 antibody binding sites. P_1, P_2, P_3, P_4, and P_5, correspond to probe species with 0, 1, 2, 3, and 4 bulk targets bound to the antibody binding sites, respectively.

We similarly examined Step 2 of the MATLAB model independently of Step 1. To do this, we varied the initial concentrations of P_1 through P_5 and also varied $k_{f,s}$, $k_{r,s}$, and $T_{s,0}$. **Figure 3-2** shows the concentration of each complex species as a function of time from one of the simulations. The concentration profiles of the complexes behaved as expected. Some examples of this include: (i) all of the complex concentrations starting at 0, (ii) when probe concentrations were equal, complexes with more available antibody binding sites forming faster, and (iii) the cumulative concentration of complexes never

exceeding the initial amount of immobilized target T_{s0}. These trends were also observed over a wide range of parameter values, indicating that Step 2 of the model could predict physically intuitive results.

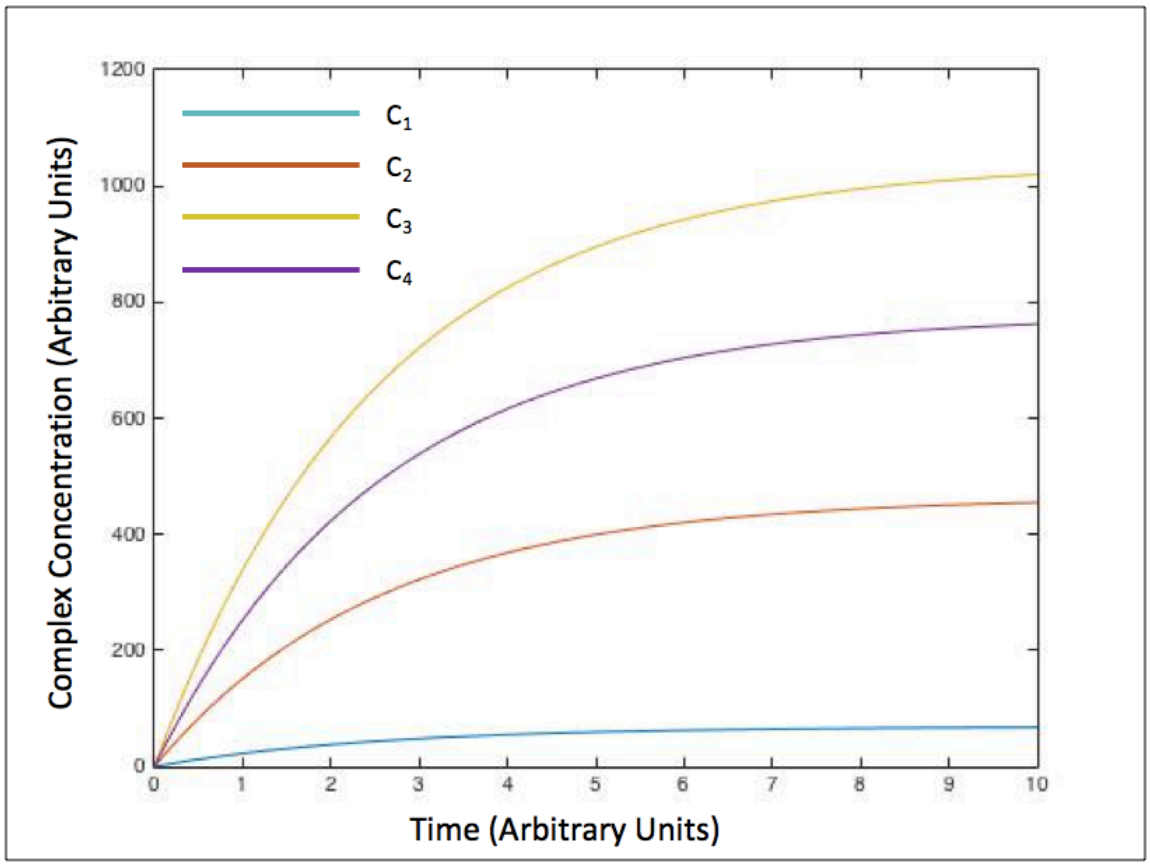

Figure 3-2. Results of Step 2 of the MATLAB model. The concentrations of each complex species with varying numbers of bulk Tf bound were monitored over time using only the MATLAB scripts for Step 2 of the model. In this simulation, the probe was only modeled to have 2 antibodies and therefore a total of 4 antibody binding sites. C_1, C_2, C_3, and C_4 correspond to complex species with 1, 2, 3, and 4 bulk targets bound to the antibody binding sites, respectively.

3.3.2 Validating the mathematical model with experimental data

Finally, we wanted to evaluate the ability of our mathematical model to accurately predict DGNP binding to an LFA test line in response to varying initial Tf target

concentrations. Since the experiments we were trying to predict were performed with probes conjugated to 4 antibodies, 8 total binding sites were considered. We used parameter values determined from the experiments described in Chapter 2. We ran the MATLAB model simulation at varying initial Tf concentrations ranging from 1.25 x 10^{-11} M to 1.25 x 10^{-6} M at evenly spaced intervals on a logarithmic scale. We then experimentally quantified the amount of DGNPs bound to the LFA test for the same range of Tf concentrations. The experimental results and mathematical model predictions are plotted in **Fig. 3-3**.

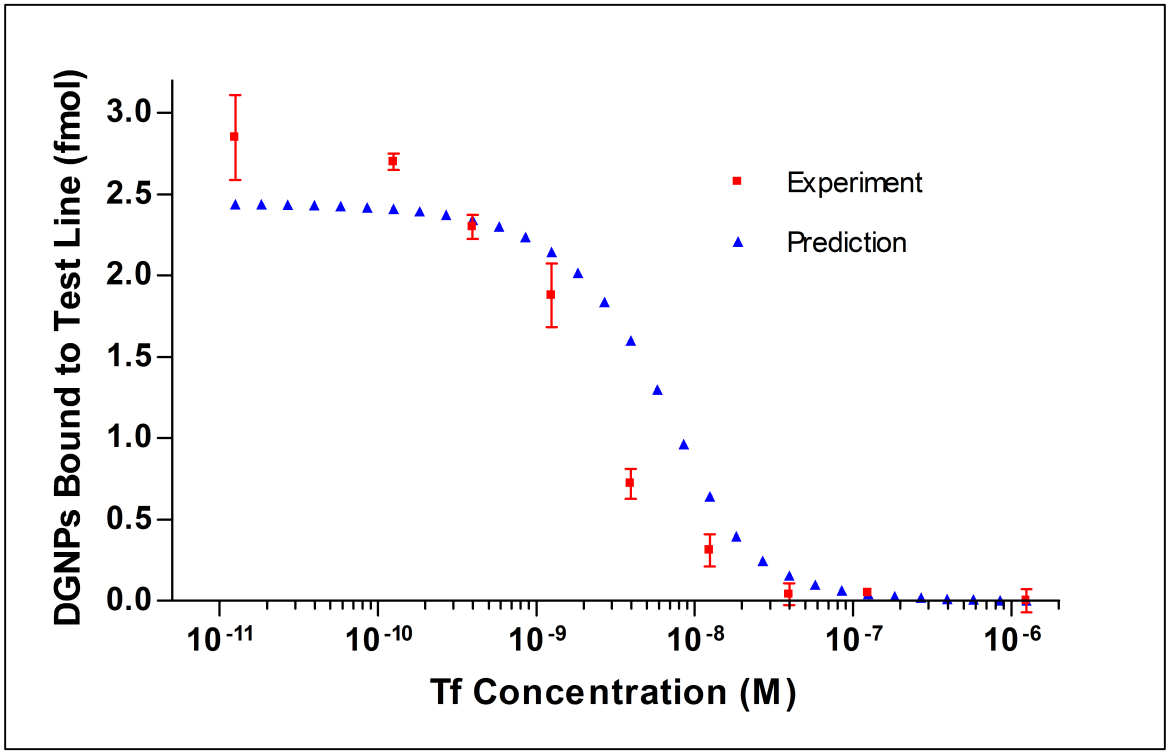

Figure 3-3. Validation of the complete model. Comparison between experiment and prediction for various initial Tf concentrations.

We see from **Fig. 3-3** that the model reasonably predicts the experimental results for DGNP binding. This is encouraging as the model incorporated many differential

equations and parameters. However, the inflection point of the model prediction is at a higher target concentration value than that based on the experimental data. This corresponds to predicting a higher (worse) limit of detection, which may be due to underestimating the volume of the test line region as that would lead to predicting less time allowed for binding of the DGNPs to the test line.

3.4 Conclusions

In conclusion, we have developed a 2 step mathematical model the predicts the amount of probe binding to an LFA test line in response to an initial target concentration. This model requires parameter inputs from our novel experimental methods described in Chapter 2, such as the $k_{f,b}$, $k_{r,b}$, $k_{f,s}$, $k_{r,s}$, probe molarity, and antibodies per probe. Our model is separated into 2 steps, where the first step captures the interaction between the target in the bulk solution and the individual antibody binding sites on the probe, and the second step captures the interaction between the probe and the immobilized target on the test line. We demonstrated that each step of the model could predict physically intuitive results for a wide range of parameter values. Finally, we demonstrated that our integrated model predicts experimental results with reasonable accuracy by comparing the predictions to empirical data using transferrin as a target molecule.

4. Elimination of Preparation Steps for Aqueous Two-Phase Systems Integrated with the Lateral-Flow Immunoassay

4.1 Overview

Chlamydia is one of the most common sexually transmitted infections, with over 1.4 million new cases reported in 2014 in the US alone. A promising method for attenuating the spread of chlamydia is through frequent screening of at-risk individuals. For this screening strategy to be effective, it is imperative to use point-of-care (POC) diagnostics that are rapid, accurate, cost-effective, and can be operated by untrained personnel. Paper diagnostics are a promising technology for this purpose, and have seen significant advancements in recent years in efforts to improve their sensitivity. Our lab has previously developed a method to thermodynamically concentrate target molecules to improve lateral-flow immunoassay (LFA) sensitivity by utilizing aqueous two-phase systems (ATPS). Unfortunately, this straightforward testing method still requires some training to perform, and therefore is limited in its application as a screening diagnostic. In this work, we describe a diagnostic design that eliminates all sample preparation steps while still accomplishing thermodynamic target concentration. This was accomplished by dehydrating the ATPS components directly into the paper diagnostic device to require only the sample to be applied. We visually demonstrated successful ATPS phase separation in order to confirm rapid and sufficient resolubilization of ATPS components. We further identified the importance of ordering the dehydrated potassium phosphate upstream of the

dehydrated polyethylene glycol. Finally, we demonstrated that our novel design improves the limit of detection for a *Chlamydia trachomatis* LFA by 10-fold. This significant advancement in our technology enables the test to be operated by untrained personnel, significantly expanding its applicability as a POC test.

4.2 Motivation and Background

Chlamydia is a sexually transmitted infection (STI) caused by the bacteria *Chlamydia trachomatis* which, if left untreated, can lead to pelvic inflammatory disease in women and cause permanent damage to the reproductive system.[61] The prevalence of chlamydia has been steadily rising in the United States since 1993, with over 1.4 million new chlamydia infections reported in 2014.[62] Although Chlamydia is relatively straightforward to treat, and shows no signs of emerging resistance to primary pharmacological treatment options,[63] it is still one of the most common STIs in the United States.[62] One approach for addressing the increasing prevalence of chlamydia is through low cost point-of-care (POC) screening of at-risk populations, which has shown promising results in theoretical models[64,65] and isolated trial studies.[66,67]

Unfortunately, current gold standard laboratory-based diagnostics, such as nucleic acid amplification tests (NAATs) or cell culture methods, are not suitable for POC screening. This is due to the high cost of equipment, the requirement for trained personnel, and the lengthy time to result. In contrast, paper-based diagnostics are a more suitable technology, which allow on-site diagnosis and treatment within the same visit, and can be administered by personnel without any training; two components that are necessary for

effective large scale screening. The most commonly used paper diagnostic is the lateral-flow immunoassay (LFA), a visually interpreted antibody-based diagnostic recognized for its widespread use in pregnancy tests.[31] Unfortunately, chlamydia LFA tests are currently not sensitive enough to be an effective diagnostic,[5] a caveat that most paper-based diagnostics for infectious diseases suffer from.[2]

Significant efforts have been made in recent years to improve the sensitivity of paper-based assays. Some key innovations include work with two-dimensional paper networks by the Yager lab[36–40,42–44] and microfluidic paper-based analytical devices by the Whitesides lab.[45,46,48,49] Previously, our lab has developed an equipment-free method to thermodynamically pre-concentrate target analytes prior to their application to LFA tests. In short, this is accomplished by utilizing aqueous two-phase systems (ATPS), which separate into two distinct liquid phases, where the target analyte partitions extremely into one of those phases, effectively concentrating the target. In the first iteration, our 3 step diagnostic process involved (i) mixing a large volume of target solution with ATPS components, (ii) waiting for macroscopic phase separation, and (iii) extracting and applying the concentrated target phase to the LFA test. With this method, we demonstrated an improvement in the limit of detection for both large viruses[17,50] and small protein targets.[19,20] Recently, we discovered that the phase separation process is expedited when the ATPS flows through paper, reducing the overall diagnostic time from hours down to minutes by eliminating the waiting and extraction steps. Using this phenomenon, our lab demonstrated the ability to simultaneously concentrate and detect protein biomarkers within paper[21,22]. However, this diagnostic process still required an initial ATPS component mixing step prior to application of the solution to an LFA strip.

In this work, we describe a single-step ATPS paper-based diagnostic assay and demonstrate its ability to improve the limit of detection for *C. trachomatis* by 10-fold. This was accomplished through the use of our novel ATPS rehydration and resolubilization optimized wick (ARROW). In this design, the sample solution is simply added to the device, and the solution directly resolubilizes the ATPS components during flow, resulting in phase separation and subsequent concentration of *C. trachomatis* within paper. To our knowledge, this is the first demonstration of dehydrating ATPS components onto paper, allowing only the sample to be added to achieve phase separation and concentration of the target.

4.3 Materials and Methods

4.3.1 Preparation of antibody-decorated dextran-coated gold nanoprobes (DGNPs)

Dextran-coated gold nanoparticles (DGNPs) were synthesized according to Min and coworkers with slight modifications[54]. Briefly, 750 mg of dextran (Mw 15,000–25,000) from *Leuconostoc spp*. were dissolved in 10 mL of UltraPure sterile water (Rockland Immunochemicals Inc., Gilbertsville, PA). The solution was stirred and heated to a boil, after which 135 μL of a 1% w/v gold(III) chloride hydrate solution were added. The color of the reaction mixture turned reddish-violet, and was stirred and boiled for about 20 min. To form functionalized DGNPs, 35 μL of 100 mM sodium borate buffer (pH 9) were added to 1 mL of a DGNP suspension, followed by 8 μL of 2 mg/mL anti *C. trachomatis* antibodies (CT-Ab) (Medix Biochemica, Espoo, Finland). The reaction mixture was placed on a shaker for 20 min to facilitate the formation of dative bonds

between the antibodies and the DGNPs. 100 μL of 10% w/v bovine serum albumin (BSA) were then added to the suspension and then placed on a shaker for 10 min. Free antibodies were removed by centrifugation and the pellet was resuspended in 100 μL of 100 mM sodium borate buffer (pH 9.0). All materials, chemicals, and reagents were purchased from Sigma-Aldrich (St. Louis, MO) unless otherwise specified.

4.3.2 LFA test for detection of *C. trachomatis*

LFA tests with a sandwich assay format were utilized for this study. First, a solution of 2 mg/mL anti *C. trachomatis* antibodies and 25% w/v sucrose was printed onto a nitrocellulose membrane (Sartorius, Goettingen, Germany) to form the test line. Secondary anti-IgG antibodies, which bind to the primary antibodies on the CT-Ab conjugated DGNPs, were printed downstream of the CT-Ab test line to form the control line. The membrane was then left in a desiccation chamber overnight to immobilize the antibodies. In this *C. trachomatis* sandwich LFA, the presence of *C. trachomatis* in sufficient quantities will produce a red test line, while an absence or insufficient quantity of *C. trachomatis* will result in no visible test line. The presence of a control line indicates that the CT-Ab conjugated DGNPs successfully flowed across the membrane.

4.3.3 Preparation of the ARROW

To dehydrate the ATPS and LFA components in paper, pieces of fiberglass (Whatman, Pittsburgh, PA) were cut into appropriate geometries and placed onto a Petri dish. Solutions of the ATPS or LFA components were made to the appropriate concentrations and pipetted onto the paper segments. The ATPS components used were

polyethylene glycol (PEG) 8000 and potassium phosphate salt (5:1 dibasic to monobasic ratio). To dehydrate the components, the paper segments were placed under very low pressure using a Labconco FreeZone 4.5 lyophilizer (Fisher Scientific, Hampton, NH) for 2 hours.

4.3.4 Scanning electron microscopy (SEM) images

Paper segments were cut and treated using the dehydration methods described above. Paper samples included segments dehydrated with 15% (w/w) potassium phosphate, 10% (w/w) PEG, or no additional components (i.e., blank fiberglass). The paper segments were individually placed onto a dry carbon tape-covered holder and sputtered with a metallic coating using a South Bay Technology Ion Beam Sputtering/Etching System (South Bay Technology, San Clemente, CA). Samples were imaged at 500x magnification at 10 kV using a ZEISS Supra 40VP SEM (ZEISS, Irvine, CA) at the Electron Imaging Center for NanoMachines and CNSI at UCLA.

4.3.5 Importance of the rehydration order of PEG and potassium phosphate

In order to visualize the phase separation of the ATPS paper, BSA conjugated DGNPs (BSA-DGNPs), which are red due to surface plasmon resonance,[68,69] and Brilliant Blue FCF dye (The Kroger Co., Cincinnati, OH) were both added to a solution of ATPS made in phosphate-buffered saline (PBS). The BSA-DGNPs partitioned extremely to the PEG-poor phase, while the Brilliant Blue dye partitioned to the PEG-rich phase. This allowed us to the use the suspension to identify the locations of PEG-poor phase

(burgundy/light purple in color), PEG-rich phase (light blue in color), and mixed domain regions (dark blue/dark purple in color) directly on the paper.

Experiments were performed with only a single sheet of the ARROW and without a tapered tip in order to better observe the phase separation behavior. In one condition, the potassium phosphate was dehydrated upstream of the PEG, and in the other condition the PEG was dehydrated upstream of the potassium phosphate. The concentration of the dehydrated components were 15% (w/w) potassium phosphate and 10% (w/w) PEG 800. Images were taken with a Canon EOS 1000D camera (Canon U.S.A., Inc., Lake Success, NY).

4.3.6 Dynamics of phase separation within the ARROW

To visualize phase separation, we set up the ARROW component of our diagnostic with dehydrated 15% (w/w) potassium phosphate and 10% (w/w) PEG 8000. This setup did not contain the LFA membrane or conjugate pad. The suspension containing the BSA-DGNPs and Brilliant Blue dye was allowed to flow along the strip until the fluid reached the end the paper. Images were captured at different time points using a Canon EOS 1000D camera.

4.3.7 Improved limit of detection for *C. trachomatis* using the integrated LFA and ARROW

LFA tests were run at varying *C. trachomatis* concentrations between 0.5 and 500 ng/μL, such that they were evenly spaced on a logarithmic scale, for the LFA only system and the integrated LFA and ARROW system. The sample solutions contained *C.*

trachomatis (EastCoast Bio, North Berwick, ME) diluted in PBS. The sample solution volumes were 70 and 600 μL per test for the control and dehydrated ATPS conditions, respectively. A smaller sample volume was used for the control because it did not have the ARROW component, and therefore, did not require as much sample volume to run the test. We did not include a blank paper wick to mimic the ARROW component in the control since comparing to the case without the wick was a more stringent comparison as *C. trachomatis* can be lost in a blank wick. The tests were allowed to run for 15 minutes before images were taken with a Canon EOS 1000D camera.

Images were analyzed using a customized MATLAB script described previously developed and described by our lab.[17]. Briefly, the program takes several calibration images of a positive test with visible control and test lines, and uses those to determine the length from the control line to the test line. It then analyzes the experimental images by determining the average pixel intensity on the test line and subtracting the average pixel intensity of the white membrane background. LFA images are cropped just inside the edges of the membrane before being analyzed. The pixel intensity was plotted using GraphPad Prism. Non-linear regression was performed using GraphPad Prism and was fit to a one-phase exponential association curve.

4.4 Results and Discussion

4.4.1 Integrated LFA and ARROW diagnostic design

Our dehydrated ATPS diagnostic device (**Fig. 4-1**) is comprised of two major components: the ARROW and the standard LFA. The ARROW consists of 5 fiberglass

paper sheets layered together. Considering that the function of the ATPS is to concentrate the target pathogen, it was necessary that the ARROW was able to wick up a large volume of sample solution. Each sheet is first pre-treated with BSA in order to prevent non-specific binding of *C. trachomatis* during sample solution flow. After pre-treatment, 20 μL of 15% (w/w) potassium phosphate is dehydrated in the upstream portion of each fiberglass sheet, while 30 μL of 10% (w/w) PEG 8000 is dehydrated in the downstream portion of each fiberglass sheet. It is important to leave blank space between the dehydrated PEG and the tip of the sheet to allow for PEG-poor phase collection, which contains the concentrated pathogen. The downstream tip of each sheet is tapered to form a point, which facilitates proper transition of the liquid into the conjugate pad.

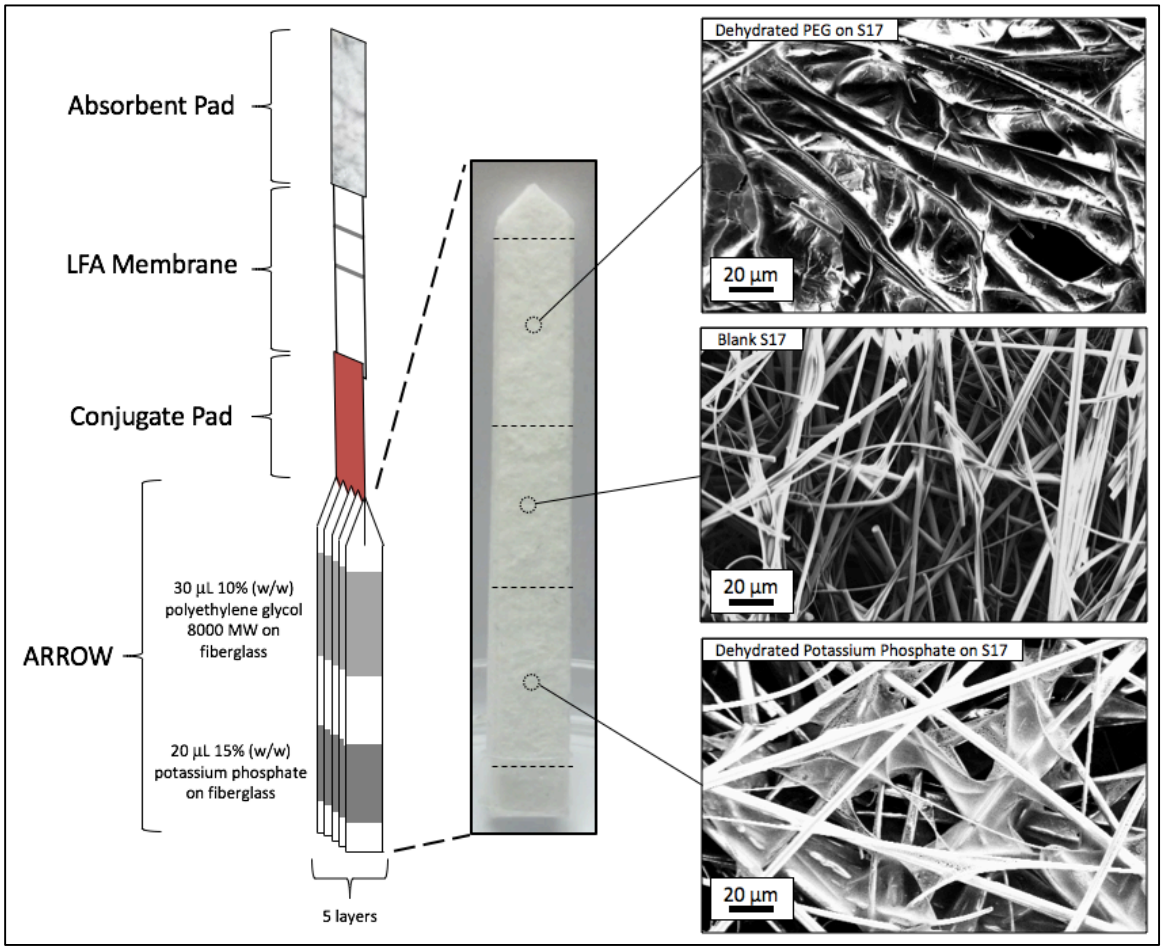

Figure 4-1. The integrated ARROW and LFA diagnostic design. (**Left**) Design layout of the integrated ARROW and LFA. (**Middle**) Image of the ARROW. (**Right**) SEM images of the dehydrated PEG on fiberglass, blank fiberglass, and dehydrated potassium phosphate on fiberglass. The top and bottom tips of the fiberglass paper sheet are also blank fiberglass.

The LFA portion of the diagnostic consisted of the conjugate pad containing the colorimetric indicator, connected to a nitrocellulose membrane with printed primary and secondary antibodies, and followed by an absorbance pad. The LFA portion interfaced with the ARROW by fitting a small upstream portion of the conjugate pad perpendicularly into a slit that had been cut in the ARROW.

SEM images (**Fig. 4-1**) of the blank fiberglass region of the fiberglass paper shows a porous fiber-based matrix structure. The dehydrated PEG and potassium phosphate

regions show a similar porous structure, with the addition of web-like connections, which we believe contain a majority of their respective ATPS components. These images demonstrate that the process of dehydration does not significantly deform the porous structure of the fiberglass paper, which is critical for proper wicking of the sample fluid.

4.4.2 Importance of the rehydration order of PEG and potassium phosphate

Our novel ARROW design introduces the unexplored concept of phase separation after sequential ATPS component resolubilization during fluid flow, which is in contrast to the traditional method of ATPS research that examines phase separation in a stagnant solution with an initial homogenous distribution of ATPS components. Therefore, we investigated the effect of the PEG and potassium phosphate rehydration order on the phase separation behavior within the paper. To do this, we utilized a suspension comprised of BSA-DGNPs and Brilliant Blue dye which allowed us to visualize the phase separation process as the suspension flowed through the paper, a technique previously utilized by our laboratory.[21] In short, the BSA-DGNPs partition into the PEG-poor phase indicated by the burgundy/light purple color, while the blue dye partitions into the PEG-rich phase indicated by the light blue color. Regions of macroscopically mixed domains contained both BSA-DGNPs and blue dye, indicated by the dark blue/dark purple color. During fiberglass paper preparation, we altered the location of the dehydrated ATPS components, such that one condition had the dehydrated potassium phosphate located upstream of the dehydrated PEG (denoted 'Salt → PEG'), while the other condition had the dehydrated PEG located upstream of the dehydrated potassium phosphate (denoted 'PEG → Salt').

From these results (**Fig. 4-2**), we note two interesting observations. First, the leading PEG-poor fluid had a significantly darker burgundy color in the 'Salt → PEG' condition compared to the 'PEG → Salt' condition, indicating that the 'Salt → PEG' condition contained more BSA-DGNPs in the leading fluid, and therefore, is more effective at concentrating large species. Second, the PEG-rich phase, the area identified by the dashed lines in **Fig. 4-2**, exhibited significantly more volumetric growth over time in the 'Salt → PEG' condition compared to the PEG-rich phase in the 'PEG → Salt' condition. This suggests that in the 'Salt → PEG' condition, the newly formed PEG-poor domains are able to get out of the mixed domain region and more efficiently pass through the trailing PEG-rich phase and collect into the leading PEG-poor phase. This results in the PEG-rich phase becoming larger as the mixed domains region becomes smaller. One possible reason for this phenomenon is the formation of PEG-poor channels within the PEG-rich phase that connect to the leading PEG-poor phase. Research in multiphase fluid flow within porous media has found that less viscous fluids will develop preferred channels when displacing more viscous fluids.[70]

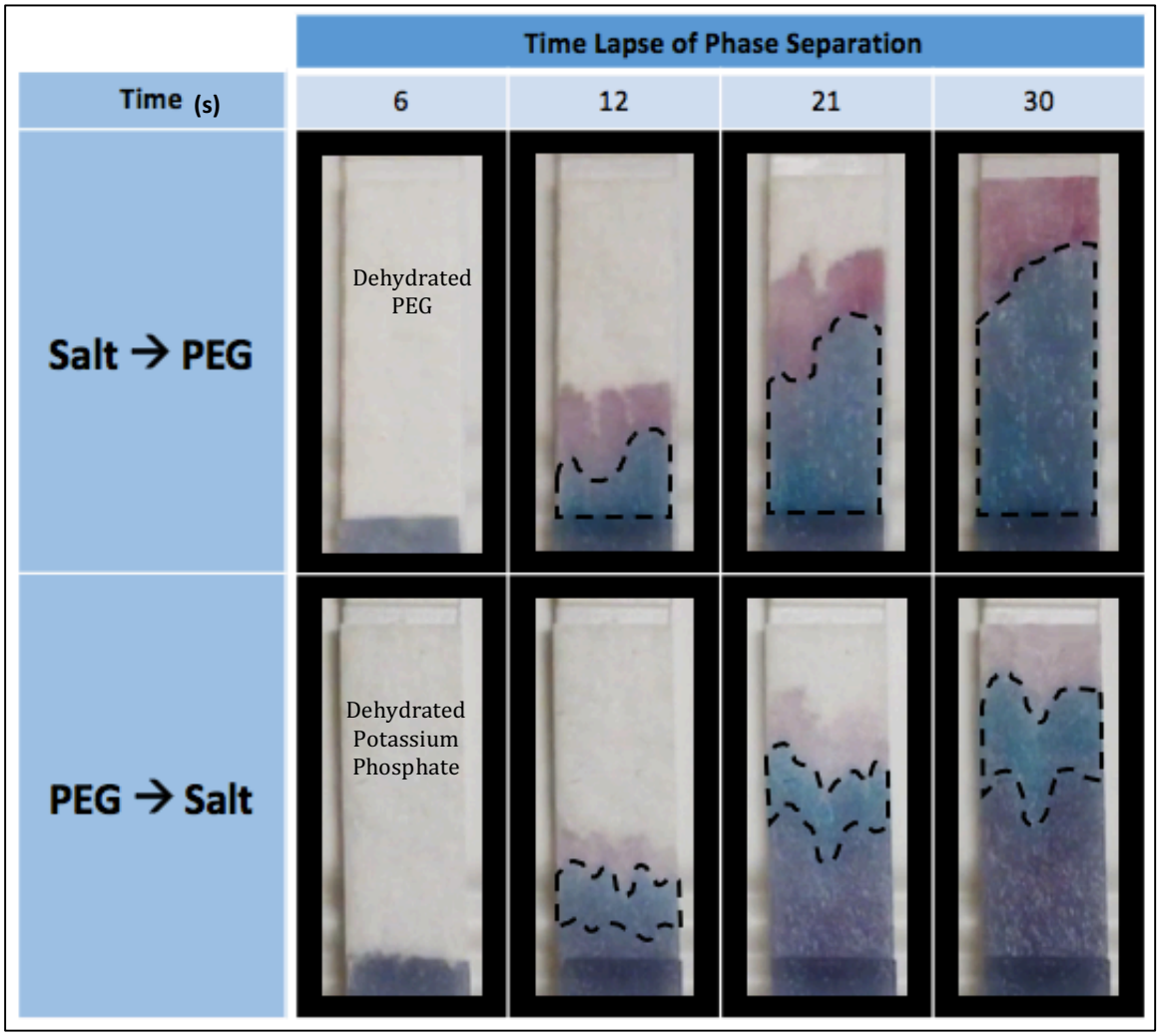

Figure 4-2. Demonstrating the importance of ATPS component rehydration order. Time-lapse visualization of phase separation within a single sheet of the ARROW design when the rehydration order of the PEG and potassium phosphate are switched. Close up images are shown of the downstream region where phase separation occurred, and therefore, the first image is at t=6s instead of t=0s. The dotted line (- - -) encompasses the region of the paper that predominantly contained the PEG-rich phase, identified by the light blue color. Visualization and identification of the PEG-rich phase, PEG-poor phase, and macroscopically mixed domain regions were accomplished by flowing a suspension of BSA-DGNPs and Brilliant Blue dye.

We hypothesize that switching the location of the ATPS components, such that PEG is resolubilized prior to potassium phosphate, reduces or prevents the formation of PEG-poor channels. When considering a sample solution flowing through the 'PEG →

Salt' condition at the point that the leading fluid transitions from the dehydrated PEG region to the dehydrated potassium phosphate region, the fluid contains a high concentration of resolubilized PEG and no potassium phosphate. As the fluid flows into the dehydrated potassium phosphate region, the concentration of potassium phosphate increases and phase separation occurs. If this situation is examined from the perspective of a traditional PEG and potassium phosphate phase diagram, initial phase separation in this leading fluid will occur at the region of high PEG and low potassium phosphate concentrations. This initial phase separation would result in a large PEG-rich phase volume and a small PEG-poor phase volume, as described by the lever rule. We hypothesize that the larger volume of the initial PEG-rich phase prevents PEG-poor channels from being formed and connecting to the leading PEG-poor phase. This would hinder subsequently formed PEG-poor domains from passing through and collecting into the leading fluid. This hypothesis is supported by our observations of the 'PEG → Salt' condition, notably: (i) the lower concentration of BSA-DGNPs in the leading PEG-poor phase, indicated by the lighter burgundy color and (ii) the presence of a macroscopically mixed domain region, located behind the PEG-rich phase, indicated by the dark purple color.

4.4.3 Dynamics of phase separation within the ARROW

It was important to demonstrate that our methods of dehydration allowed for rapid rehydration of the ATPS components during sample solution flow through the diagnostic. We also needed to determine if the quantities of dehydrated PEG and potassium phosphate were sufficient to cause phase separation. To do this, we utilized the previously described suspension comprised of BSA-DGNPs and Brilliant Blue dye.

As shown in **Fig. 4-3**, we observed successful phase separation using our ARROW setup. We noticed that phase separation occurs shortly after the suspension flowed into the dehydrated PEG region. We also noticed that the PEG-poor region collected into the leading fluid in front of the PEG-rich region, mimicking an important phenomena discovered in our previous work,[21] which is necessary considering that the PEG-poor region will contain the concentrated *C. trachomatis* and needs to be in the leading fluid when flowing through the conjugate pad. The process of flowing through the ARROW only takes approximately 30 seconds.

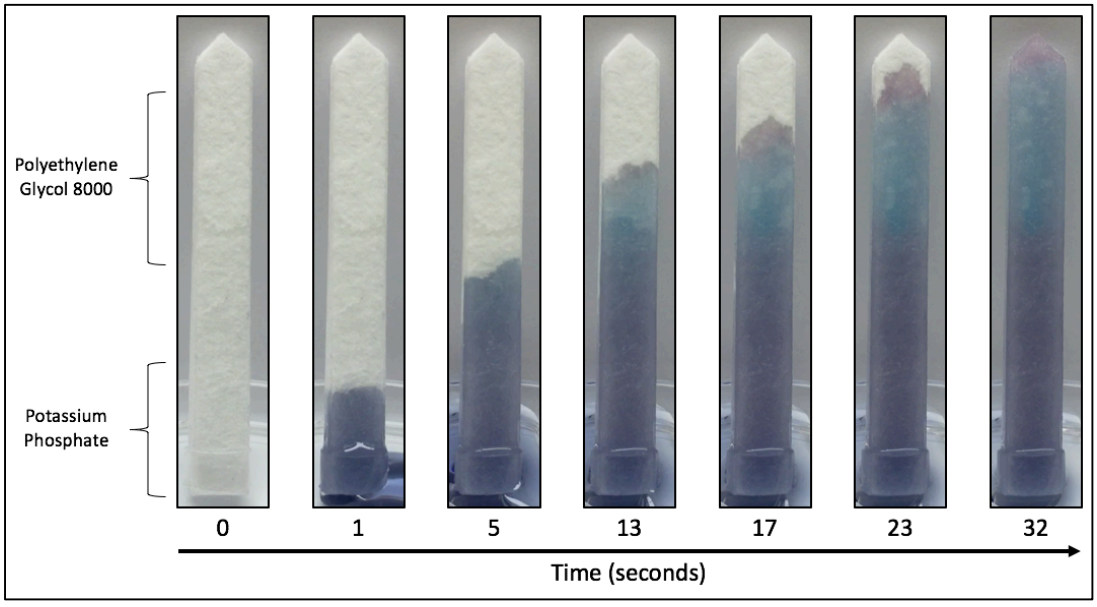

Figure 4-3. Dynamics of phase separation within the ARROW. Time-lapse images were taken of the ARROW during the process of fluid flow. The fluid consisted of a suspension of BSA-DGNPs and Brilliant Blue dye, which allowed for visualization of the phase separation.

Interestingly, we observed that the PEG-poor region in the leading fluid expanded as the fluid flowed through the dehydrated PEG region, which is best observed in the transition from time points 13 s to 23 s. During this time period we also observed that the

PEG-rich region expanded but maintained its initial location at the beginning of the dehydrated PEG region. These two observations together suggest that the dehydrated PEG and potassium phosphate quantities are sufficient to continue phase separation after initial phase separation in the leading fluid, and that the newly formed PEG-poor domains are flowing through the PEG-rich region to collect at the leading PEG-poor region.

4.4.4 Improved limit of detection for *C. trachomatis* using the integrated LFA and ARROW

Lastly, we demonstrated that our ARROW design effectively concentrated a *C. trachomatis* sample suspension, resulting in an improved limit of detection for LFA. To do this, we ran sample solutions of varying initial concentrations of *C. trachomatis* on LFA test strips, with and without the ARROW component. We see from the results of the LFA panel (**Fig. 4-4**) that the LFA only system started showing false negative results at around 15.8 ng/μL *C. trachomatis* while the integrated LFA and ARROW system started showing false negative results at around 1.58 ng/μL *C. trachomatis*. This visually demonstrates a 10-fold improvement in the limit of detection.

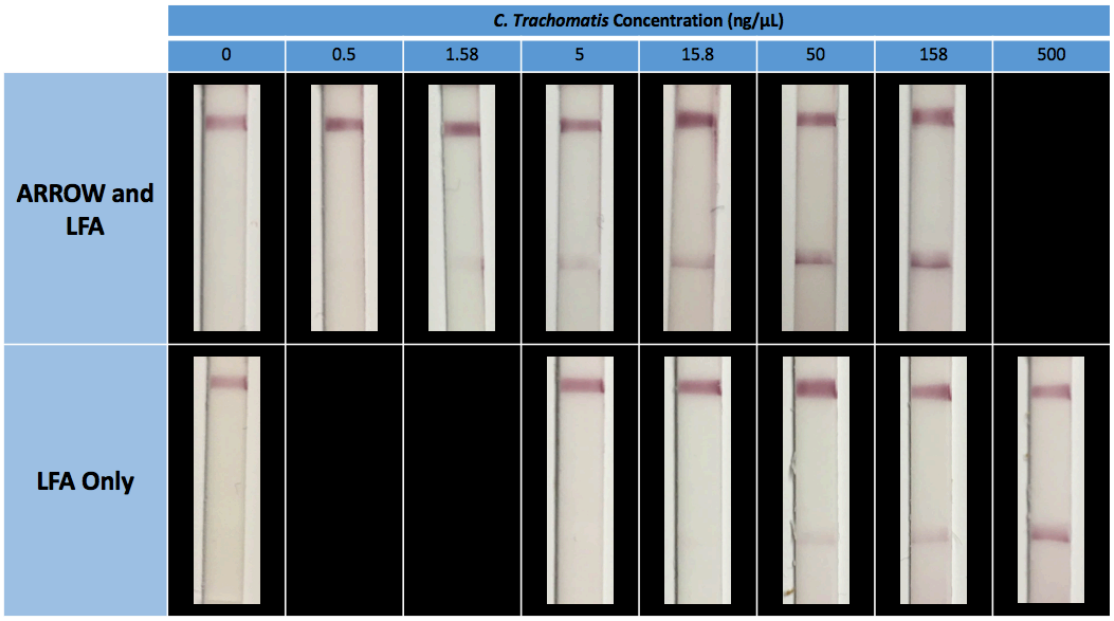

Figure 4-4. Improvement in the limit of detection of *C. trachomatis* LFA by incorporation of the ARROW. Comparison of LFA results at varying *C. trachomatis* concentrations, with and without the ARROW. Test lines are located on the bottom of the LFA strips while the control lines are located on the top of the LFA test strips. Negative control results are shown in the left most panels for 0 ng/µL *C. trachomatis*.

We also quantified the pixel contrast of the test lines on the LFA images using a customized MATLAB program developed and described by our laboratory (**Fig. 4-5**).[17] This allowed us to quantitatively assess the improvement in the limit of detection. For any given concentration of *C. trachomatis*, we see a significant increase in the test line intensity for the integrated ARROW and LFA system compared to the LFA only system. For example, at 50 ng/µL *C. trachomatis*, the LFA only condition had a pixel contrast intensity of 8.3 ±1.7, while the integrated ARROW and LFA had a pixel contrast intensity of 37.6 ±0.6. Furthermore, we also see confirmation of our panel results where the same test line intensity (8.3 pixel intensity) was observed at the limits of detection noted in the panels (15.8 ng/µL for LFA alone and 1.58 ng/µL for integrated ARROW and LFA).

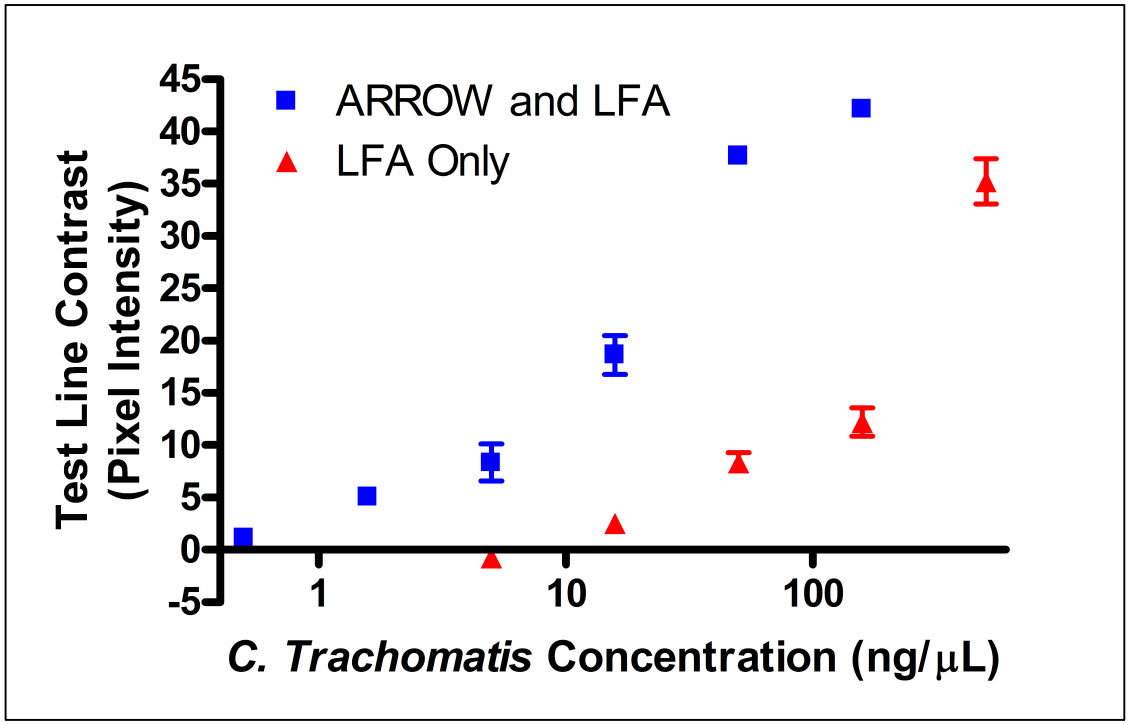

Figure 4-5. Quantification of test line intensities. Plot of the quantified LFA test line intensities for the ARROW and LFA system and the LFA only system.

4.5 Conclusions

In the current study, we presented our novel ARROW design, a paper diagnostic component that is capable of thermodynamic target concentration through dehydration of ATPS components. With this paper-based device, only the sample needs to be added to the diagnostic, removing sample preparation steps. We visually demonstrated ATPS phase separation within the ARROW, and observed an important phenomenon where the PEG-poor phase collects in the leading fluid ahead of the PEG-rich phase. Furthermore, we investigated the novel concept of sequential ATPS component rehydration and phase

separation during flow, which occurs within the ARROW. From this analysis, we found that it is important to dehydrate the potassium phosphate upstream of the PEG in order to achieve better target concentration. We hypothesized that this order is important to avoid creating an initial large PEG-rich phase which may hinder the collection of newly formed PEG-poor domains into the leading PEG-poor phase. Finally, we demonstrated that the ARROW improved the limit of detection for a *C. trachomatis* LFA test by 10-fold.

A chlamydia LFA diagnostic with improved sensitivity, that still maintains its low cost, rapid time to results, and ease of use, will significantly increase its applicability as a POC screening test. This has the potential to significantly reduce the increasing prevalence of chlamydia. Furthermore, the ARROW technology can be applied to a variety of different targets suitable for detection by LFA. Most LFA-based diagnostics for infectious diseases are not developed or not used due to poor sensitivity. Considering that the ARROW can improve LFA sensitivity without adding any additional steps to the user, our novel technology has the potential to create many viable infectious disease LFA tests, both for use by physicians and as over-the-counter tests.

5. Appendix

5.1 MATLAB Script for Mathematical Model of DGNP Binding to LFA Test Lines

5.1.1 Step 1: target binding to probe (function file)

```
function [ dPdt ] = ProbeMoL(t,P)
%UNTITLED3 Summary of this function goes here
%   Detailed explanation goes here

kfP = 5.67E5; %emperically determined kon value for Ligand-Probe
krP = 2.17E-4; %emperically determined koff value for Ligand-Probe
%Lo=1E-7; %inactivated for 'Whole_Model' which will store as 'mat' file
load('Lo_stored.mat')
%load('kfP_stored.mat')
%load('krP_stored.mat')

%L = (Lo-1*P(2)-2*P(3)-3*P(4)-4*P(5));
%note: the algrebraic function L(t) is inserted into each differential

dP1dt = -8*kfP*P(1)*(Lo-1*P(2)-2*P(3)-3*P(4)-4*P(5)-5*P(6)-6*P(7)-7*P(8)-8*P(9))+1*krP*P(2);
dP2dt = 8*kfP*P(1)*(Lo-1*P(2)-2*P(3)-3*P(4)-4*P(5)-5*P(6)-6*P(7)-7*P(8)-8*P(9))-1*krP*P(2) - 7*kfP*P(2)*(Lo-1*P(2)-2*P(3)-3*P(4)-4*P(5)-5*P(6)-6*P(7)-7*P(8)-8*P(9))+2*krP*P(3);
dP3dt = 7*kfP*P(2)*(Lo-1*P(2)-2*P(3)-3*P(4)-4*P(5)-5*P(6)-6*P(7)-7*P(8)-8*P(9))-2*krP*P(3) - 6*kfP*P(3)*(Lo-1*P(2)-2*P(3)-3*P(4)-4*P(5)-5*P(6)-6*P(7)-7*P(8)-8*P(9))+3*krP*P(4);
dP4dt = 6*kfP*P(3)*(Lo-1*P(2)-2*P(3)-3*P(4)-4*P(5)-5*P(6)-6*P(7)-7*P(8)-8*P(9))-3*krP*P(4) - 5*kfP*P(4)*(Lo-1*P(2)-2*P(3)-3*P(4)-4*P(5)-5*P(6)-6*P(7)-7*P(8)-8*P(9))+4*krP*P(5);
dP5dt = 5*kfP*P(4)*(Lo-1*P(2)-2*P(3)-3*P(4)-4*P(5)-5*P(6)-6*P(7)-7*P(8)-8*P(9))-4*krP*P(5) - 4*kfP*P(5)*(Lo-1*P(2)-2*P(3)-3*P(4)-4*P(5)-5*P(6)-6*P(7)-7*P(8)-8*P(9))+5*krP*P(6);
dP6dt = 4*kfP*P(5)*(Lo-1*P(2)-2*P(3)-3*P(4)-4*P(5)-5*P(6)-6*P(7)-7*P(8)-8*P(9))-5*krP*P(6) - 3*kfP*P(6)*(Lo-1*P(2)-2*P(3)-3*P(4)-4*P(5)-5*P(6)-6*P(7)-7*P(8)-8*P(9))+6*krP*P(7);
dP7dt = 3*kfP*P(6)*(Lo-1*P(2)-2*P(3)-3*P(4)-4*P(5)-5*P(6)-6*P(7)-7*P(8)-8*P(9))-6*krP*P(7) - 2*kfP*P(7)*(Lo-1*P(2)-2*P(3)-3*P(4)-4*P(5)-5*P(6)-6*P(7)-7*P(8)-8*P(9))+7*krP*P(8);
dP8dt = 2*kfP*P(7)*(Lo-1*P(2)-2*P(3)-3*P(4)-4*P(5)-5*P(6)-6*P(7)-7*P(8)-8*P(9))-7*krP*P(8) - 1*kfP*P(8)*(Lo-1*P(2)-2*P(3)-3*P(4)-4*P(5)-5*P(6)-6*P(7)-7*P(8)-8*P(9))+8*krP*P(9);
dP9dt = 1*kfP*P(8)*(Lo-1*P(2)-2*P(3)-3*P(4)-4*P(5)-5*P(6)-6*P(7)-7*P(8)-8*P(9))-8*krP*P(9);
dPdt = [dP1dt;dP2dt;dP3dt;dP4dt;dP5dt;dP6dt;dP7dt;dP8dt;dP9dt];

end
```

5.1.2 Step 1: target binding to Probe (script file)

```
Ptoto = 1.5E-9; %total initial probe concentration in Molarity. Emperically determined and calculated
Pinits = [Ptoto 0 0 0 0 0 0 0 0]; %Probe initial values
tstep = .1;
ttotal = 600; %this is the length of time that the entire test is run
tstop = (m*ttotal)/mpoints; %this shortens the time that the ODE23s has to solve for
tspan = 0:tstep:tstop; %this is the time range that ODE23s will solve the system for
[t,P]=ode23s('ProbeMoL',tspan,Pinits);

%plot(t,P) %skip plot command for "Whole_Model"

Pt = tstop; %time (seconds) at which to find specific Probe values
tv = Pt/tstep+1; %converting desired time point into apropriate time step

%defining and Probe values at a single time point
P1t = P(tv,1);
P2t = P(tv,2);
P3t = P(tv,3);
P4t = P(tv,4);
P5t = P(tv,5);
P6t = P(tv,6);
P7t = P(tv,7);
P8t = P(tv,8);
P9t = P(tv,9);

%saving Probe values in a 'mat' file to be recalled in 'Complex' function file
save ('Probe_Pt_constants','P1t','P2t','P3t','P4t','P5t','P6t','P7t','P8t');
```

5.1.3 Step 2: probe binding to test line (function file)

```
function [ dCdt ] = ComplexMoL(t,C)
%UNTITLED2 Summary of this function goes here
%   Detailed explanation goes here

kfC = 5.7E5; %emperically determined kon value for Probe-Receptor
krC = 3.75E-4; %emperically determined koff value for Probe-Receptor
Ro = 4E-13; %emperically determined initial bindable receptors per test line
v = 8E-7; %emperically determined total fluid volume (in L) within test line. 8.2uL/cm^2 * (test line area)

%Extracting Probe values from 'Probe_solver'
load('Probe_Pt_constants.mat')

load('m_loop_round.mat') %Extracting m loop round to set initial C?t values

if (m==1);
    C1t = 0;  %setting initial values to 0 for the first m loop of the ComplexMoL equations.
    C2t = 0;
    C3t = 0;
    C4t = 0;
    C5t = 0;
    C6t = 0;
    C7t = 0;
    C8t = 0;
end

if (m>1);
    load('Cinits_for_ComplexMol.mat');
end

%Ctot=(C(1)+C(2)+C(3)+C(4)+C(5)+C(6)+C(7)+C(8));
%note: the algebraic function Ctot(t) is inserted into each differential
%2.3 is correction factor for steric hinderance

dC1dt = (8)*kfC*(P1t-(C(1)-C1t)/(v))*(Ro-2.3*(C(1)+C(2)+C(3)+C(4)+C(5)+C(6)+C(7)+C(8)))-krC*C(1);
dC2dt = (7)*kfC*(P2t-(C(2)-C1t)/(v))*(Ro-2.3*(C(1)+C(2)+C(3)+C(4)+C(5)+C(6)+C(7)+C(8)))-krC*C(2);
dC3dt = (6)*kfC*(P3t-(C(3)-C1t)/(v))*(Ro-2.3*(C(1)+C(2)+C(3)+C(4)+C(5)+C(6)+C(7)+C(8)))-krC*C(3);
dC4dt = (5)*kfC*(P4t-(C(4)-C1t)/(v))*(Ro-2.3*(C(1)+C(2)+C(3)+C(4)+C(5)+C(6)+C(7)+C(8)))-krC*C(4);
dC5dt = (4)*kfC*(P5t-(C(5)-C1t)/(v))*(Ro-2.3*(C(1)+C(2)+C(3)+C(4)+C(5)+C(6)+C(7)+C(8)))-krC*C(5);
dC6dt = (3)*kfC*(P6t-(C(6)-C1t)/(v))*(Ro-2.3*(C(1)+C(2)+C(3)+C(4)+C(5)+C(6)+C(7)+C(8)))-krC*C(6);
dC7dt = (2)*kfC*(P7t-(C(7)-C1t)/(v))*(Ro-2.3*(C(1)+C(2)+C(3)+C(4)+C(5)+C(6)+C(7)+C(8)))-krC*C(7);
dC8dt = (1)*kfC*(P8t-(C(8)-C1t)/(v))*(Ro-2.3*(C(1)+C(2)+C(3)+C(4)+C(5)+C(6)+C(7)+C(8)))-krC*C(8);
dCdt = [dC1dt;dC2dt;dC3dt;dC4dt;dC5dt;dC6dt;dC7dt;dC8dt];


end
```

5.1.4 Step 2: probe binding to test line (script file)

```
%Cinits = [0 0 0 0 0 0 0 0]; %Complex initial values, disabled for MoL model
tstep = .1;
tspan = 0:tstep:5; %range of time to solve the equations for tank 2
[t,C]=ode23s('ComplexMoL',tspan,Cinits);

%plot(t,C) %skip plot command for "Whole_Model"

Ct = 4; %time (seconds) at which to find specific Probe values. Needs to less than the max in the tspan.
tv = Ct/tstep+1; %converting desired time point into appropriate time step.

%defining and Probe values at a single time point
C1t = C(tv,1);
C2t = C(tv,2);
C3t = C(tv,3);
C4t = C(tv,4);
C5t = C(tv,5);
C6t = C(tv,6);
C7t = C(tv,7);
C8t = C(tv,8);

Cinits = [C1t C2t C3t C4t C5t C6t C7t C8t]; %storing complex concentrations to be used in following cycle of m loop.

save ('Cinits_for_ComplexMol','C1t','C2t','C3t','C4t','C5t','C6t','C7t','C8t'); %storing for ComplexMol function when m loop is greater than 1

%Ctot=C1t+C2t+C3t+C4t+C5t+C6t+C7t+C8t; %disabled for MoL model

```

5.1.5 Integration of steps 1 and 2 (script file)

```
clear
clc

start_Conc = 1.25E-11; %starting ligand concentration to plot. Molarity
end_Conc = 1.25E-6; %ending ligand concentration to plot. Molarity
npoints = 31; %number of target concentration points to plot. 101 points takes ~20 seconds
mpoints = 600; %number of discrete volumes to exposed to test line (using Method of Lines)

LoSpan = logspace(log10(start_Conc),log10(end_Conc),npoints); %Ligand span of concentrations
TotalBound = [1:npoints];

for n = 1:npoints

    Lo = LoSpan(n); %indexing sequential Lo values from outside the for loop
    save ('Lo_stored','Lo'); %storing the Lo value in 'mat' file to be recalled in the Probe function

    Cinits = [0 0 0 0 0 0 0 0];  %reseting initial complex concentrations to 0 before m loop



    for m = 1:mpoints

        save ('m_loop_round', 'm'); %storing m loop round to plug into the ComplexMoL function

        run('D:\Matlab\Probe_solverMoL.m')
        run('D:\Matlab\Complex_solverMoL.m')

        clc
        n
        m

    end

    TotalBound(n)=C1t+C2t+C3t+C4t+C5t+C6t+C7t+C8t;


end
TotalBound;

semilogx(LoSpan,TotalBound)

beep;
```

5.2 SEM images of integrated LFA and ARROW components

5.2.1 Blank fiberglass paper

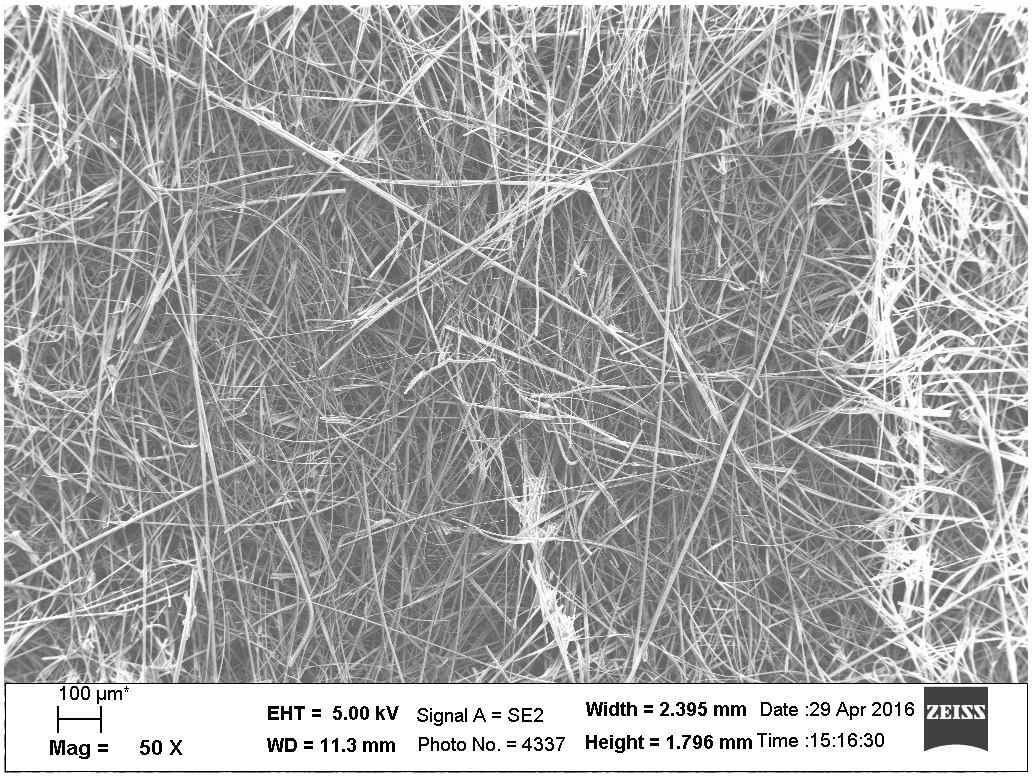

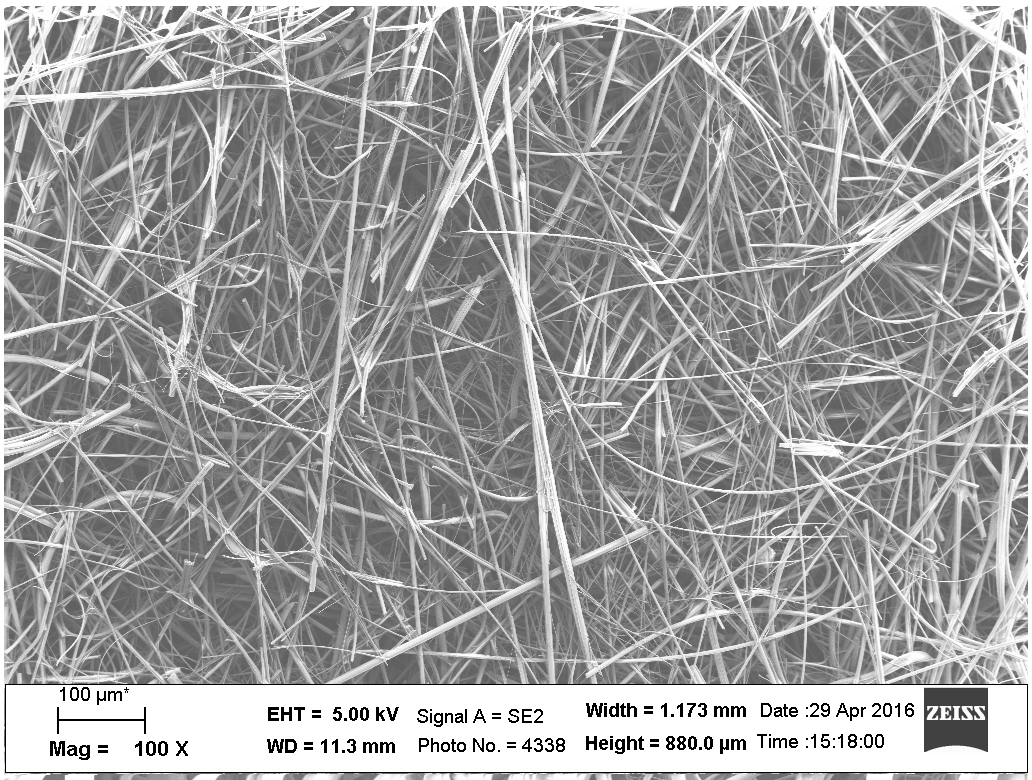
100 µm*
Mag = 100 X
EHT = 5.00 kV
WD = 11.3 mm
Signal A = SE2
Photo No. = 4338
Width = 1.173 mm
Height = 880.0 µm
Date :29 Apr 2016
Time :15:18:00
ZEISS

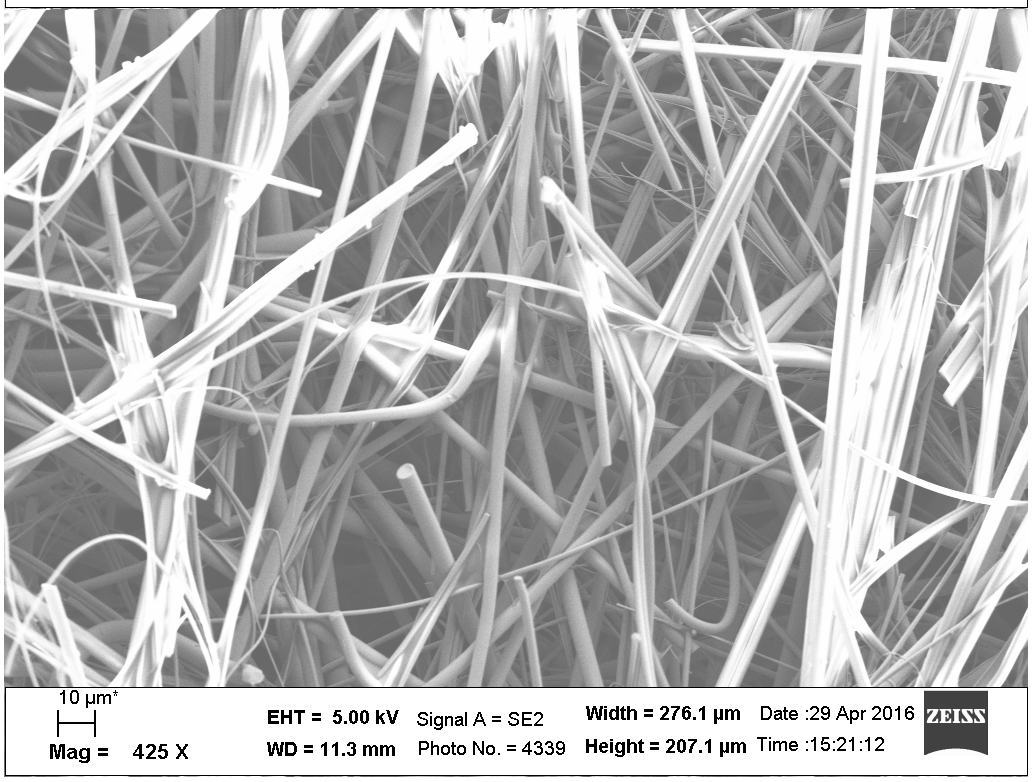
10 µm*
Mag = 425 X
EHT = 5.00 kV
WD = 11.3 mm
Signal A = SE2
Photo No. = 4339
Width = 276.1 µm
Height = 207.1 µm
Date :29 Apr 2016
Time :15:21:12
ZEISS

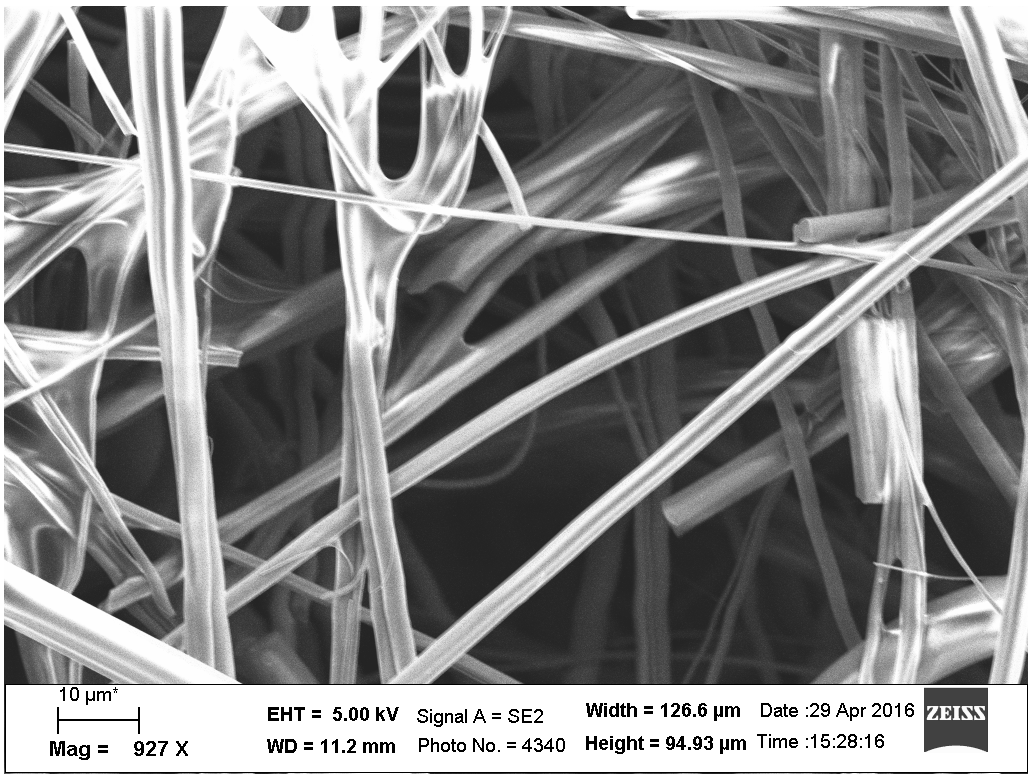

5.2.2 Dehydrated DGNPs on fiberglass paper

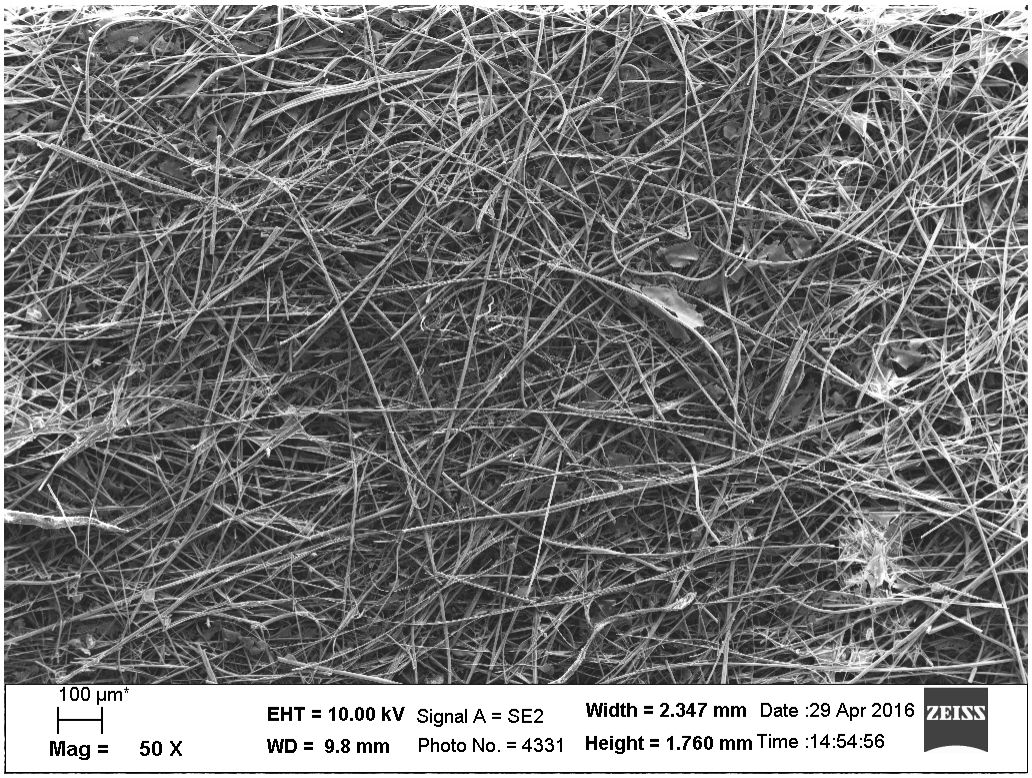

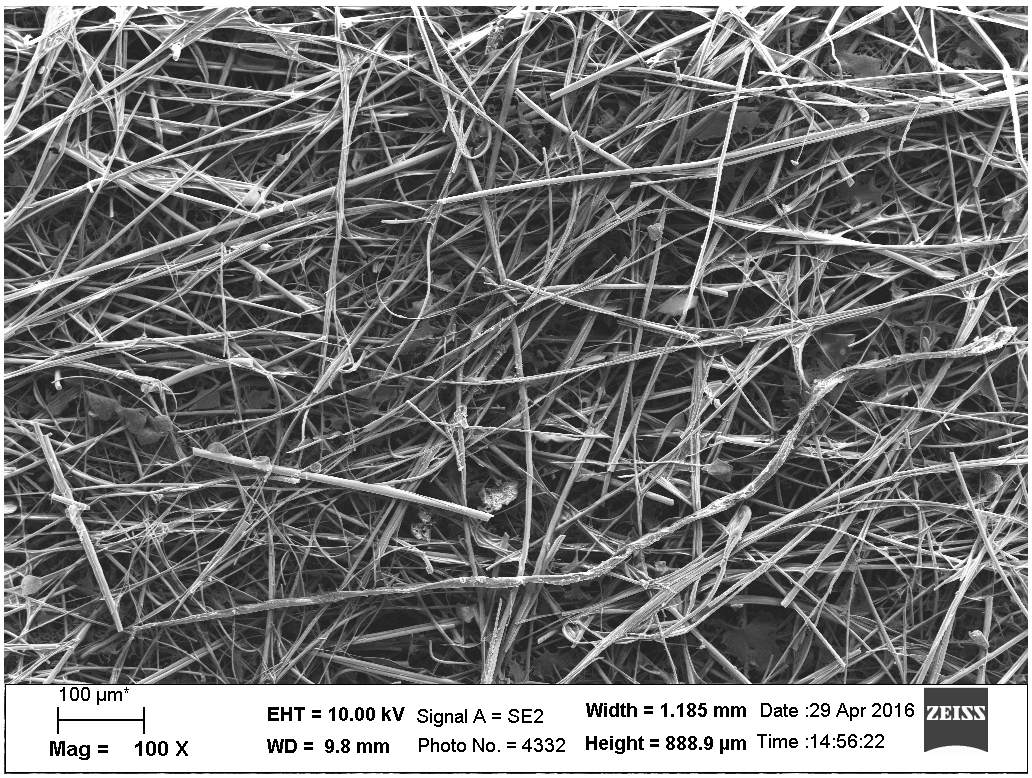
100 µm*
Mag = 100 X
EHT = 10.00 kV Signal A = SE2
WD = 9.8 mm Photo No. = 4332
Width = 1.185 mm Date :29 Apr 2016
Height = 888.9 µm Time :14:56:22
ZEISS

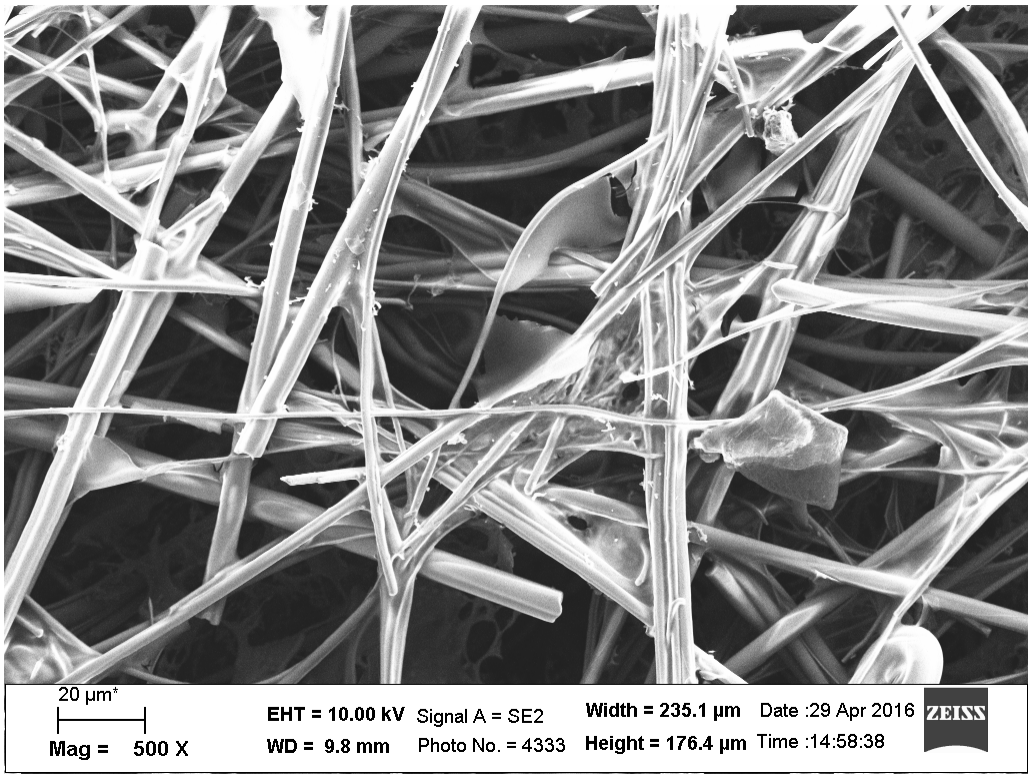
20 µm*
Mag = 500 X
EHT = 10.00 kV Signal A = SE2
WD = 9.8 mm Photo No. = 4333
Width = 235.1 µm Date :29 Apr 2016
Height = 176.4 µm Time :14:58:38
ZEISS

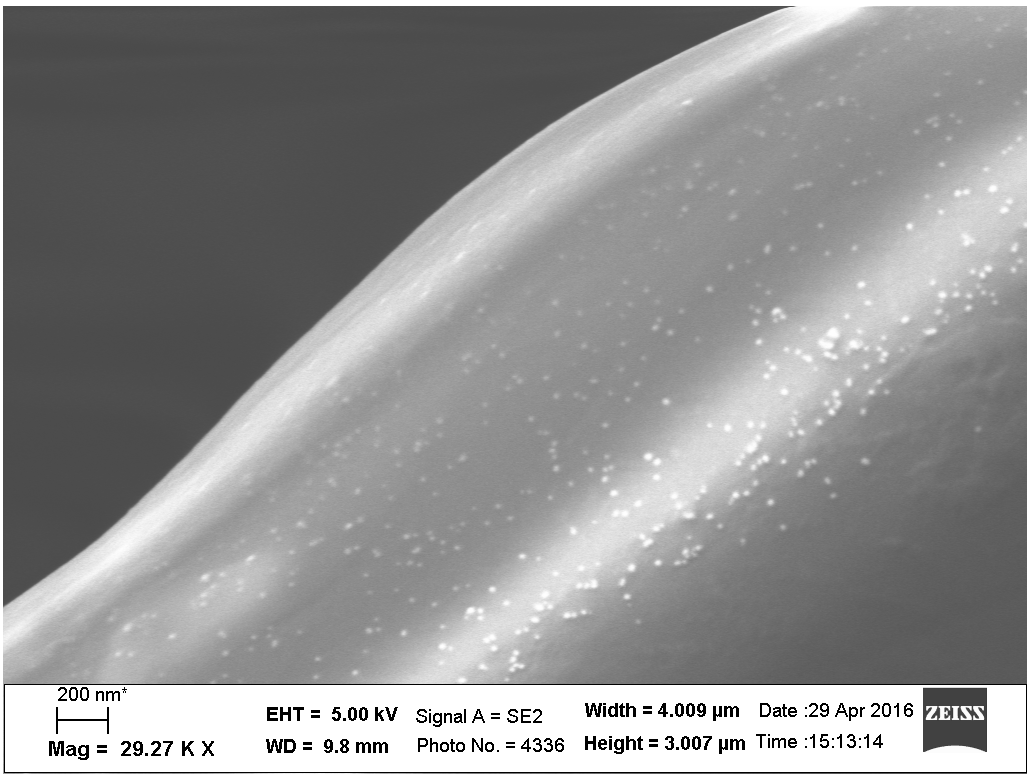
200 nm*
Mag = 29.27 K X
EHT = 5.00 kV
WD = 9.8 mm
Signal A = SE2
Photo No. = 4336
Width = 4.009 µm
Height = 3.007 µm
Date :29 Apr 2016
Time :15:13:14
ZEISS

5.2.3 Nitrocellulose membrane

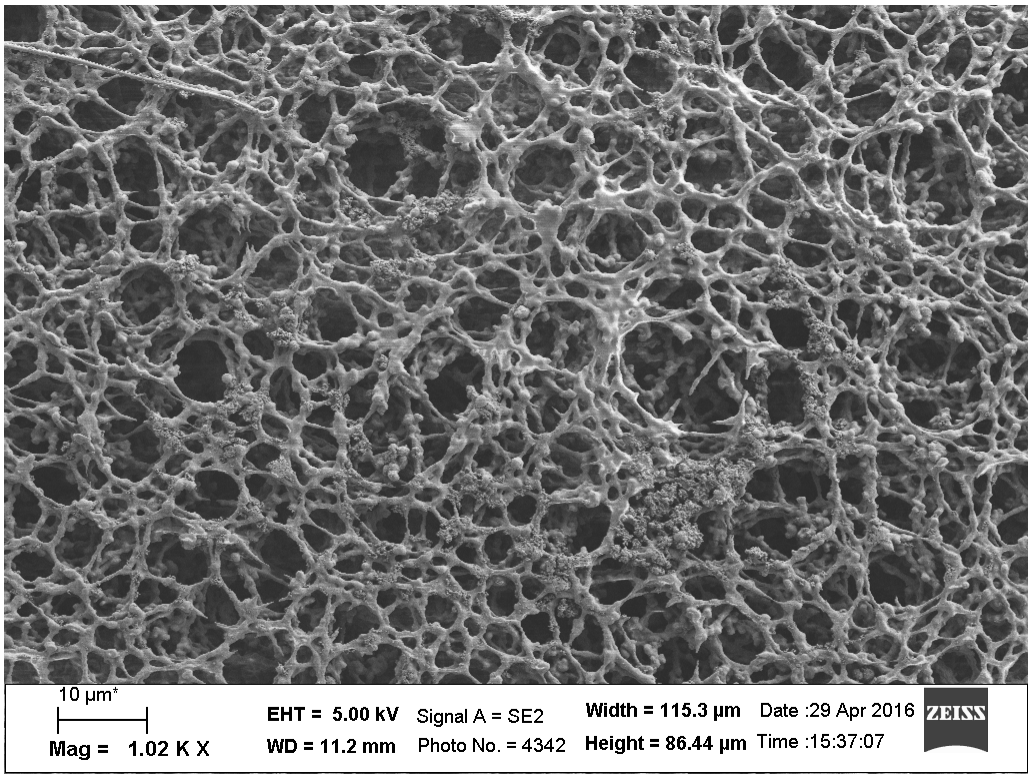

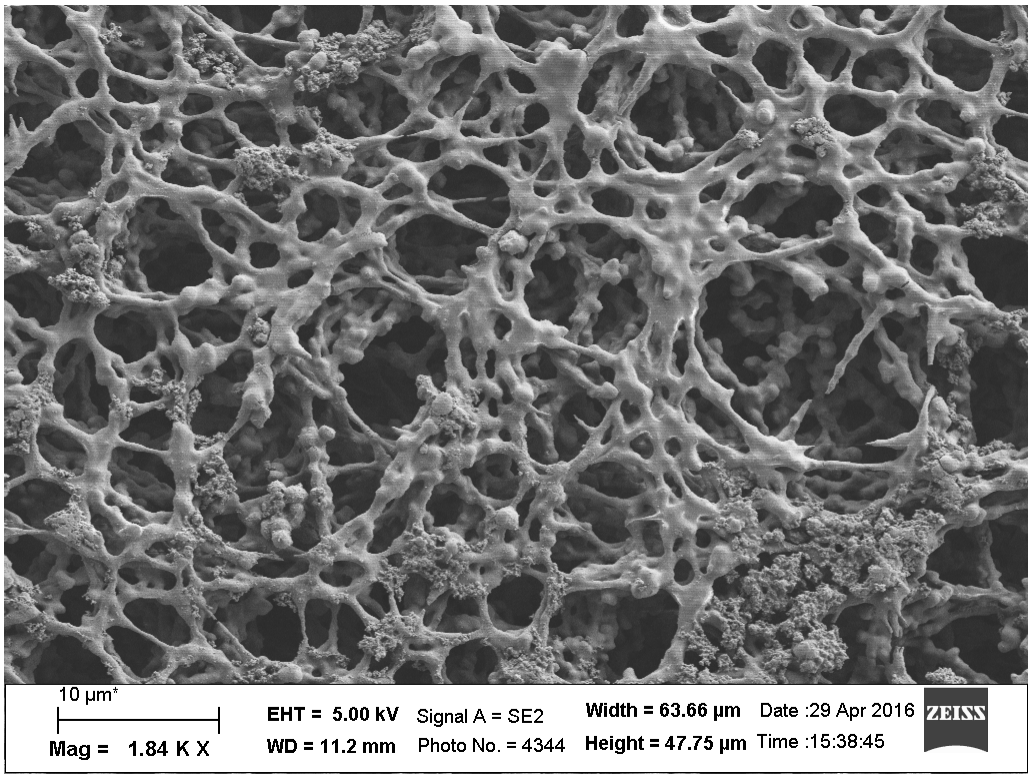

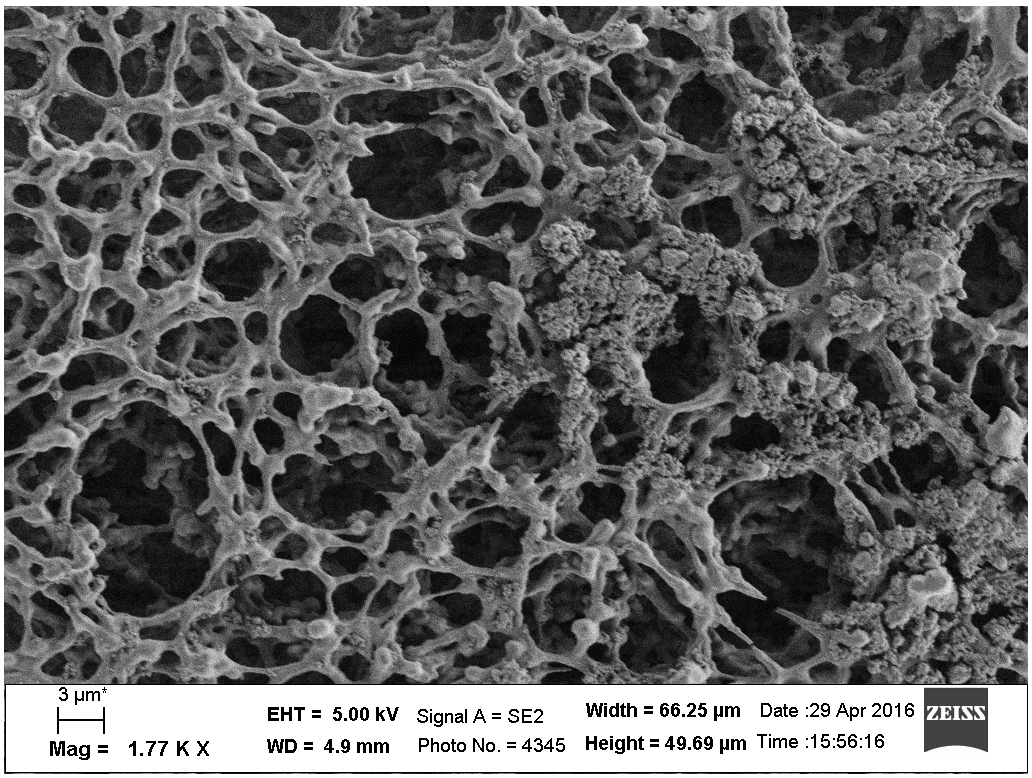
3 µm*
Mag = 1.77 K X
EHT = 5.00 kV
WD = 4.9 mm
Signal A = SE2
Photo No. = 4345
Width = 66.25 µm
Height = 49.69 µm
Date :29 Apr 2016
Time :15:56:16
ZEISS

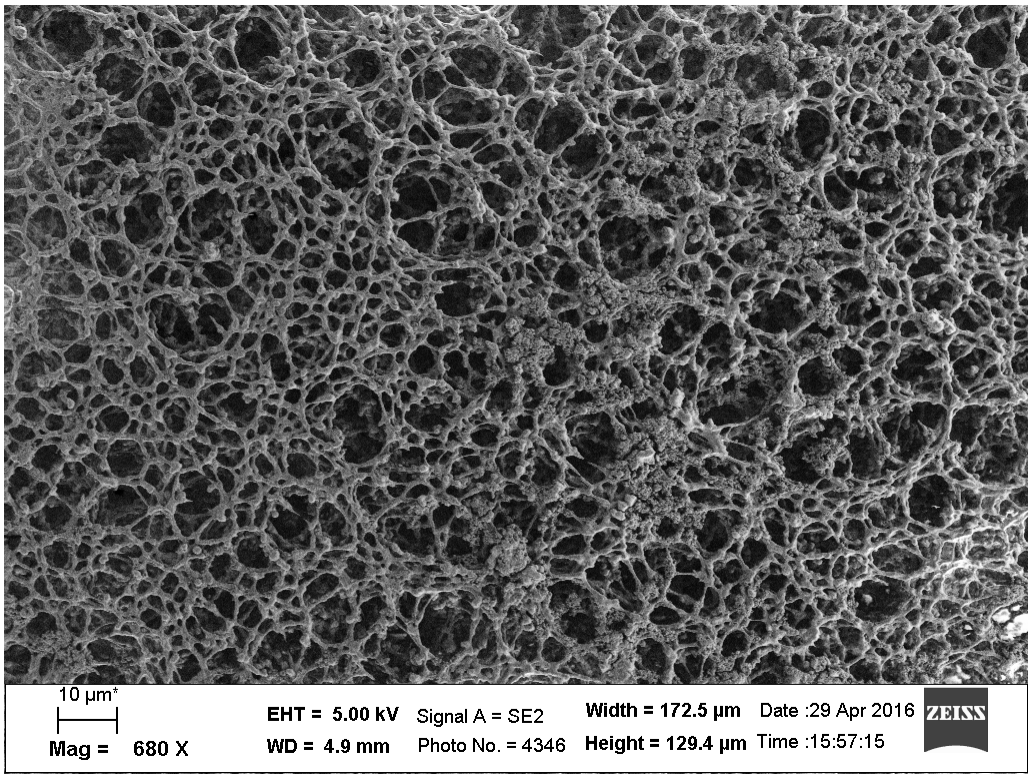
10 µm*
Mag = 680 X
EHT = 5.00 kV
WD = 4.9 mm
Signal A = SE2
Photo No. = 4346
Width = 172.5 µm
Height = 129.4 µm
Date :29 Apr 2016
Time :15:57:15
ZEISS

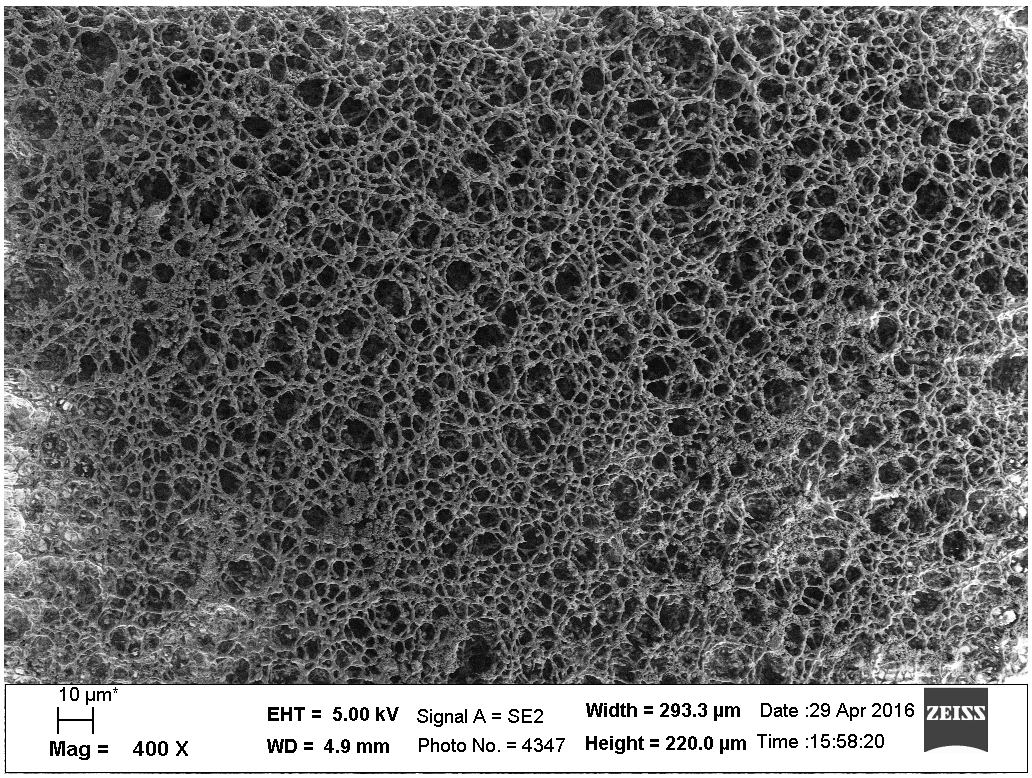
10 µm*
Mag = 400 X
EHT = 5.00 kV
WD = 4.9 mm
Signal A = SE2
Photo No. = 4347
Width = 293.3 µm
Height = 220.0 µm
Date :29 Apr 2016
Time :15:58:20
ZEISS

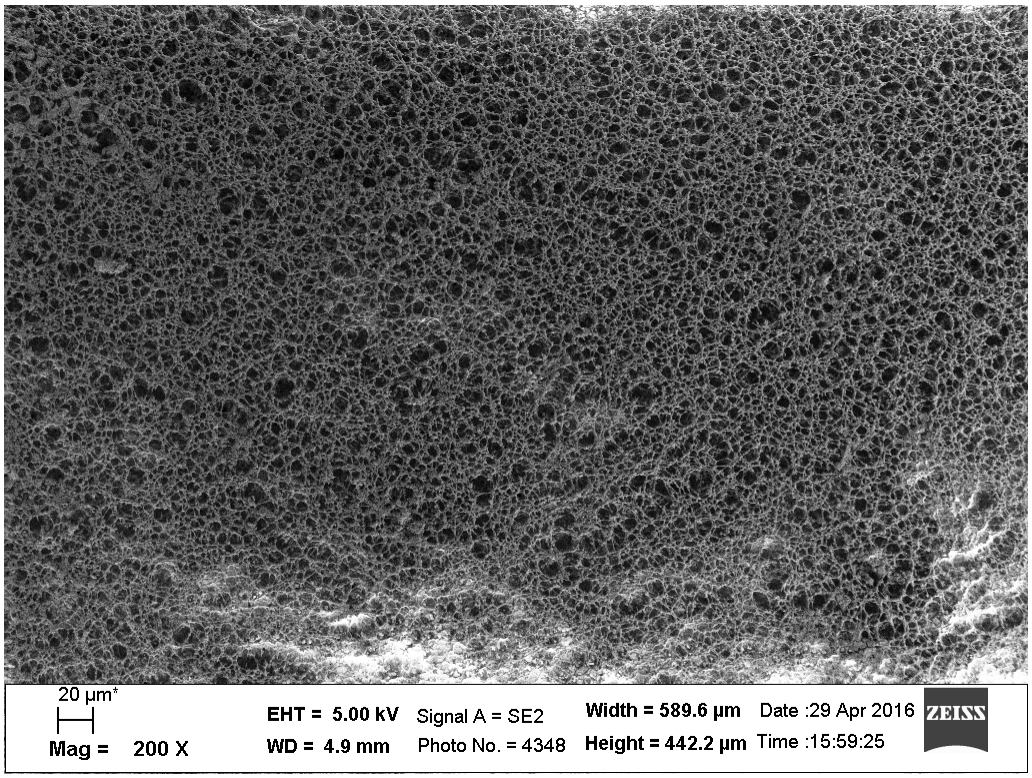
20 µm*
Mag = 200 X
EHT = 5.00 kV
WD = 4.9 mm
Signal A = SE2
Photo No. = 4348
Width = 589.6 µm
Height = 442.2 µm
Date :29 Apr 2016
Time :15:59:25
ZEISS

5.2.4 Dehydrated PEG regions on fiberglass paper

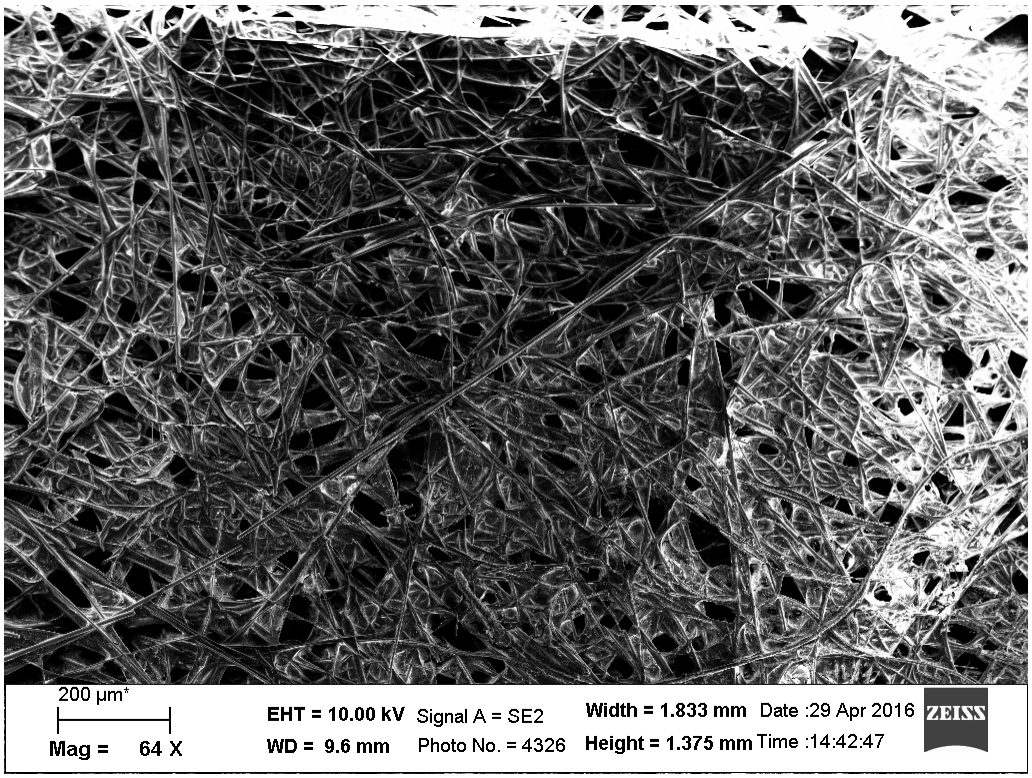

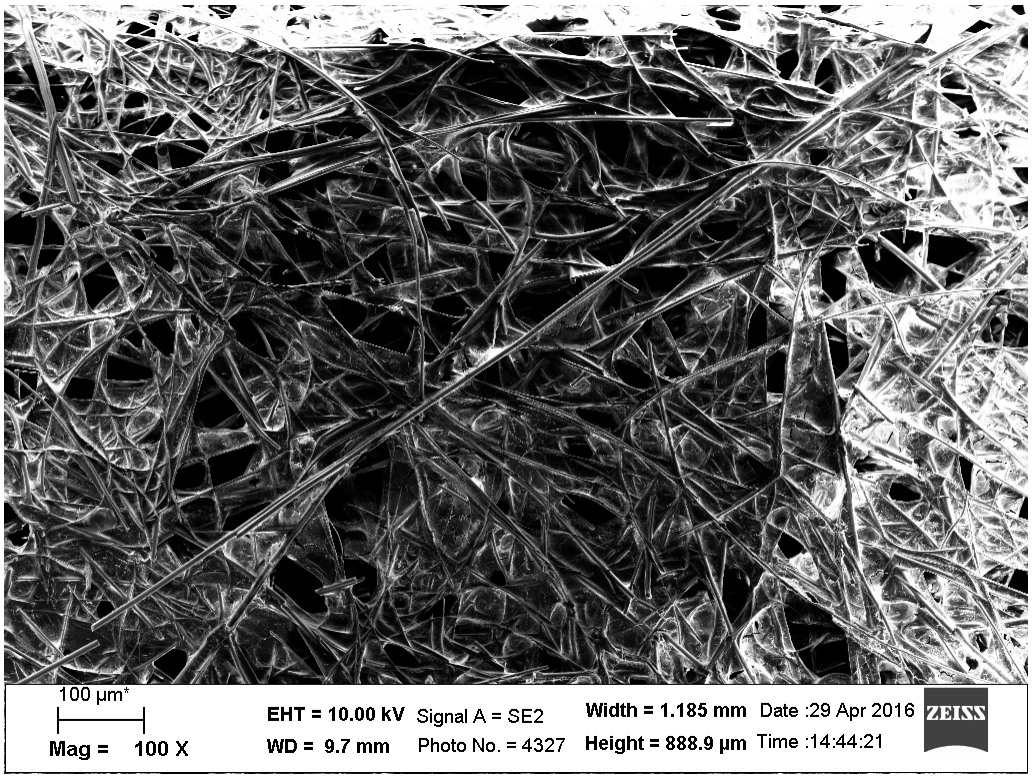

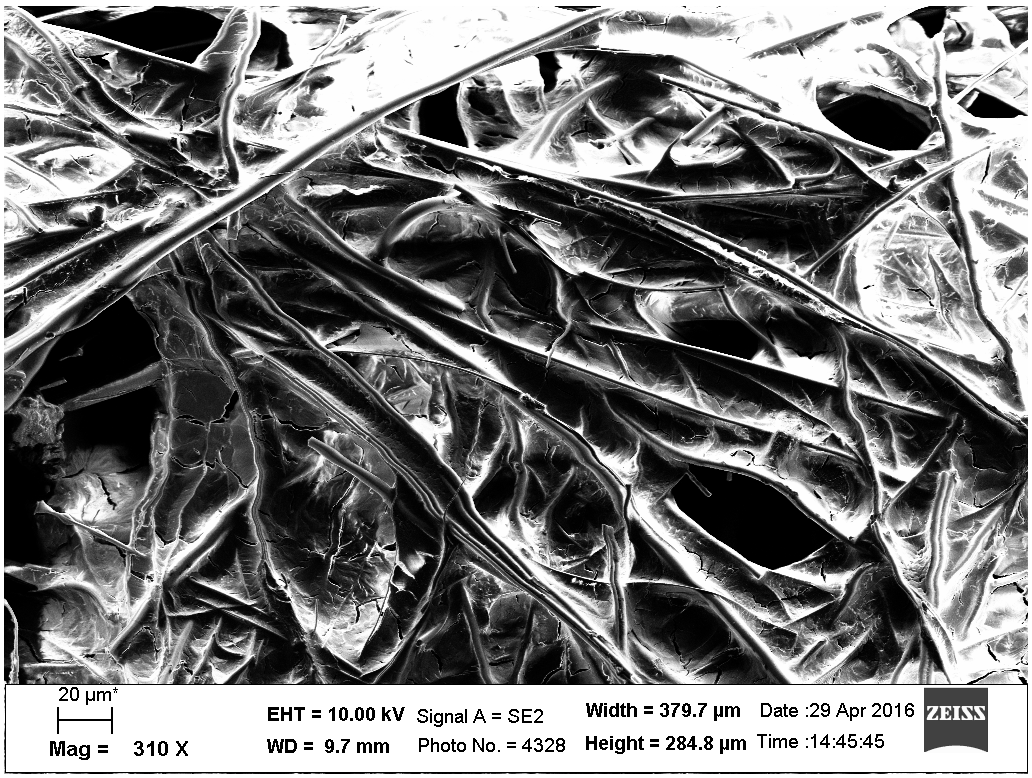
20 µm*
Mag = 310 X
EHT = 10.00 kV
WD = 9.7 mm
Signal A = SE2
Photo No. = 4328
Width = 379.7 µm
Height = 284.8 µm
Date :29 Apr 2016
Time :14:45:45
ZEISS

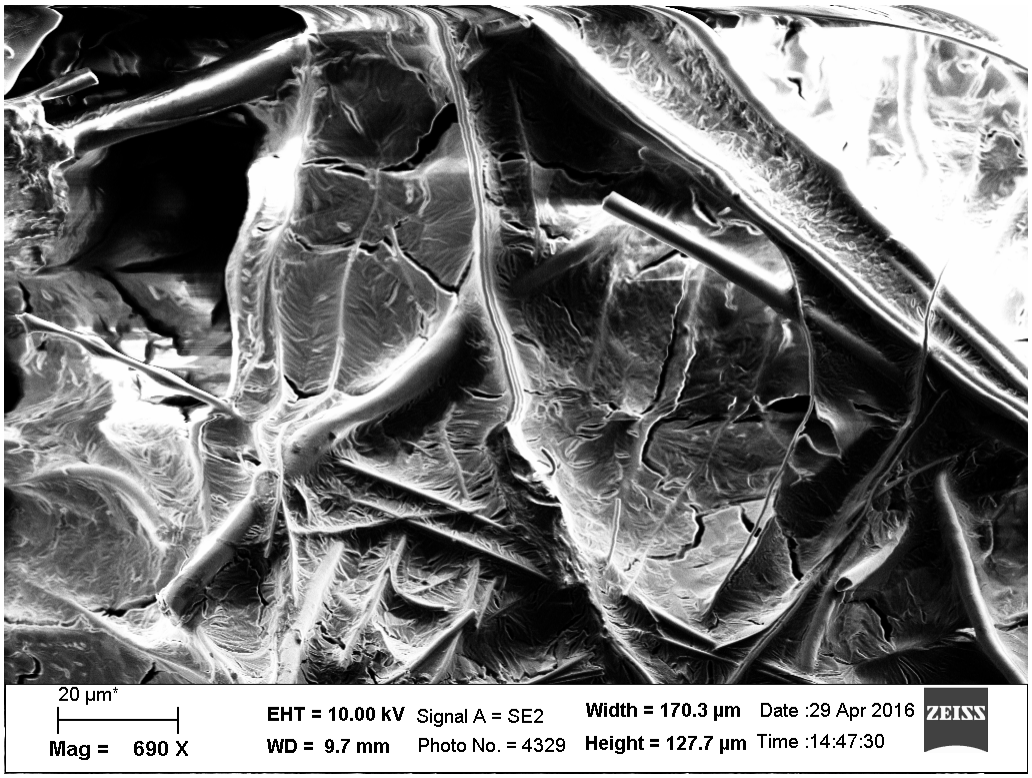
20 µm*
Mag = 690 X
EHT = 10.00 kV
WD = 9.7 mm
Signal A = SE2
Photo No. = 4329
Width = 170.3 µm
Height = 127.7 µm
Date :29 Apr 2016
Time :14:47:30
ZEISS

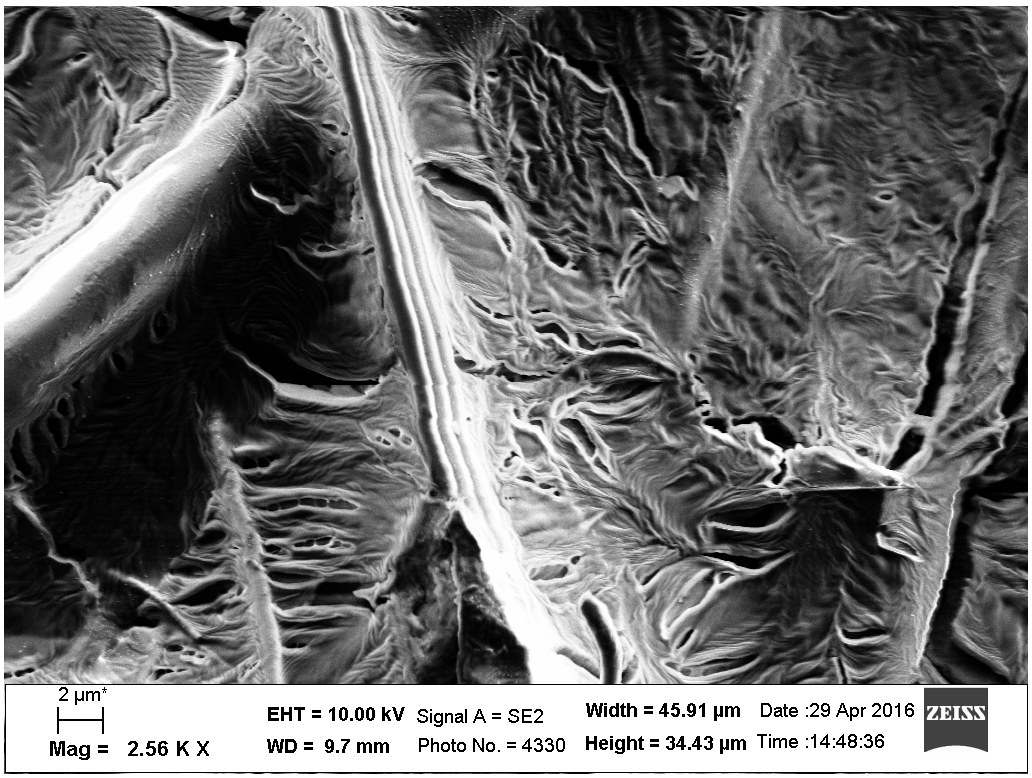
2 µm*
Mag = 2.56 K X
EHT = 10.00 kV
WD = 9.7 mm
Signal A = SE2
Photo No. = 4330
Width = 45.91 µm
Height = 34.43 µm
Date :29 Apr 2016
Time :14:48:36
ZEISS

5.2.5 Dehydrated potassium phosphate region on fiberglass paper

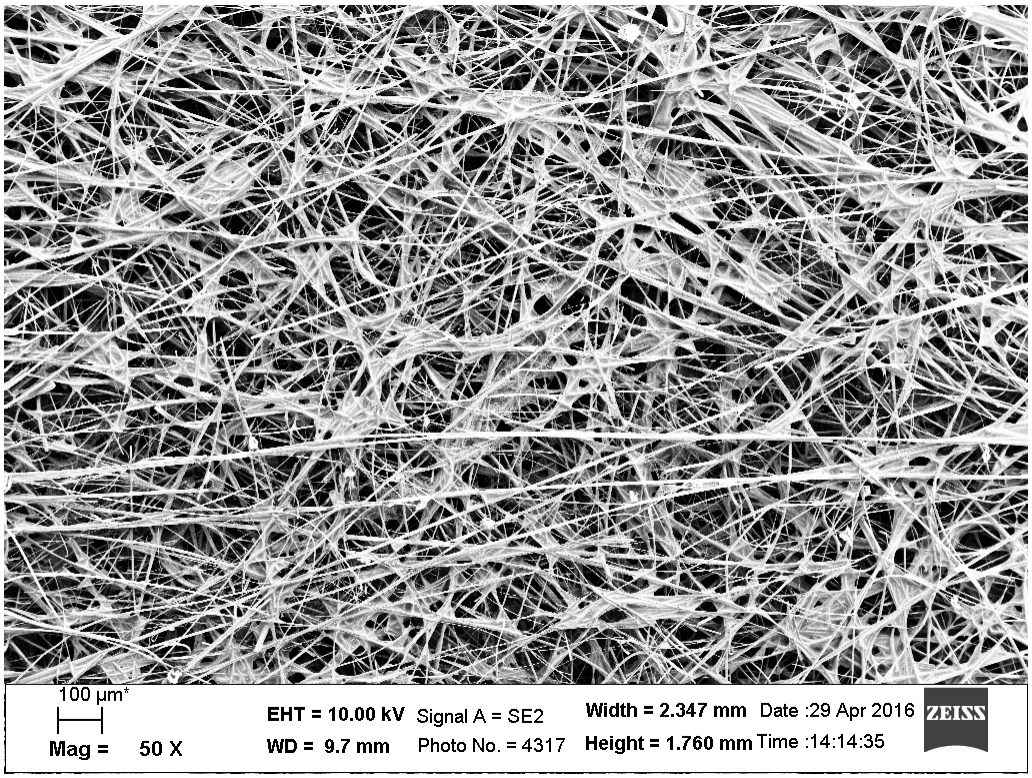

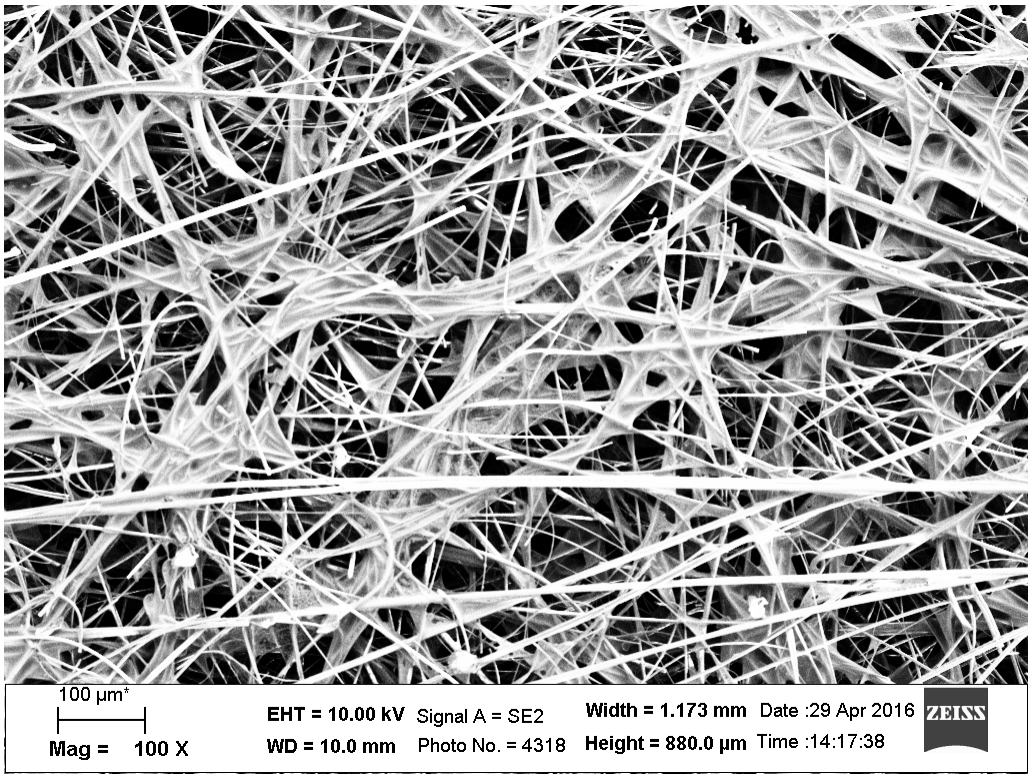

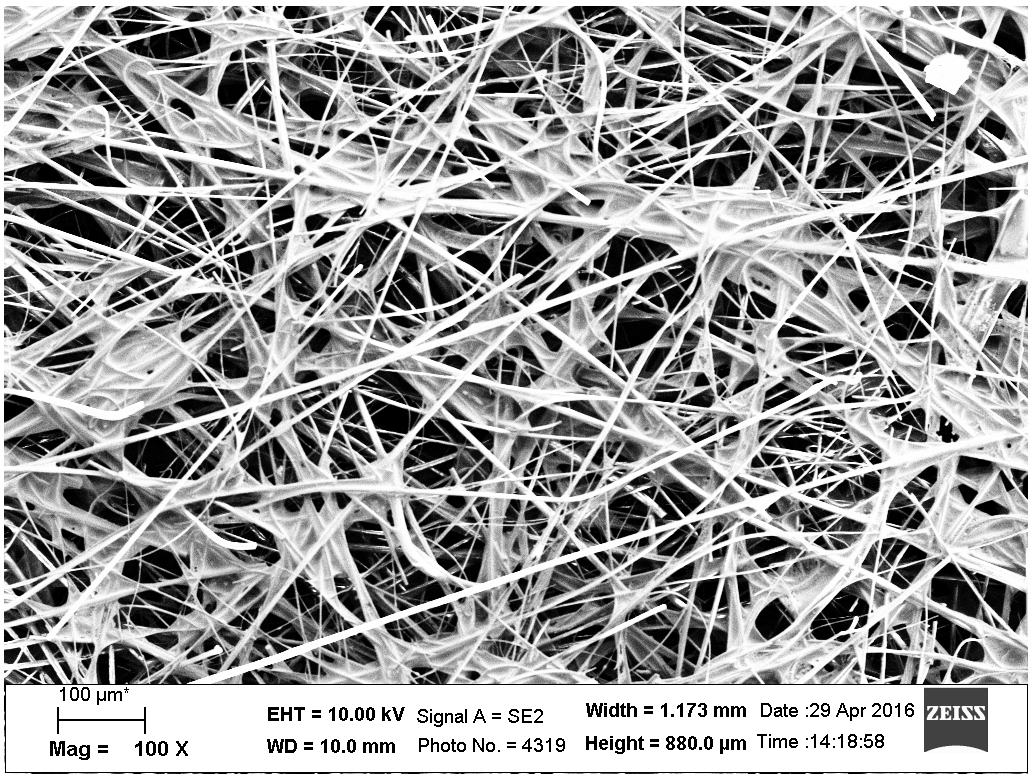
100 µm*
Mag = 100 X
EHT = 10.00 kV Signal A = SE2
WD = 10.0 mm Photo No. = 4319
Width = 1.173 mm Date :29 Apr 2016
Height = 880.0 µm Time :14:18:58
ZEISS

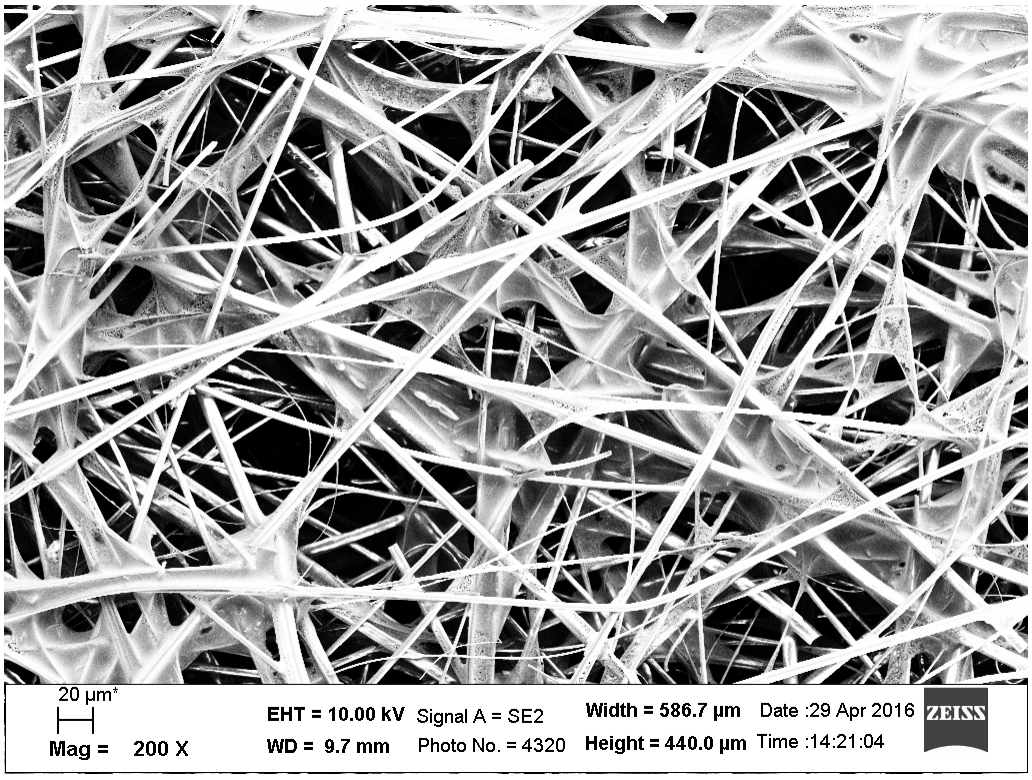
20 µm*
Mag = 200 X
EHT = 10.00 kV Signal A = SE2
WD = 9.7 mm Photo No. = 4320
Width = 586.7 µm Date :29 Apr 2016
Height = 440.0 µm Time :14:21:04
ZEISS

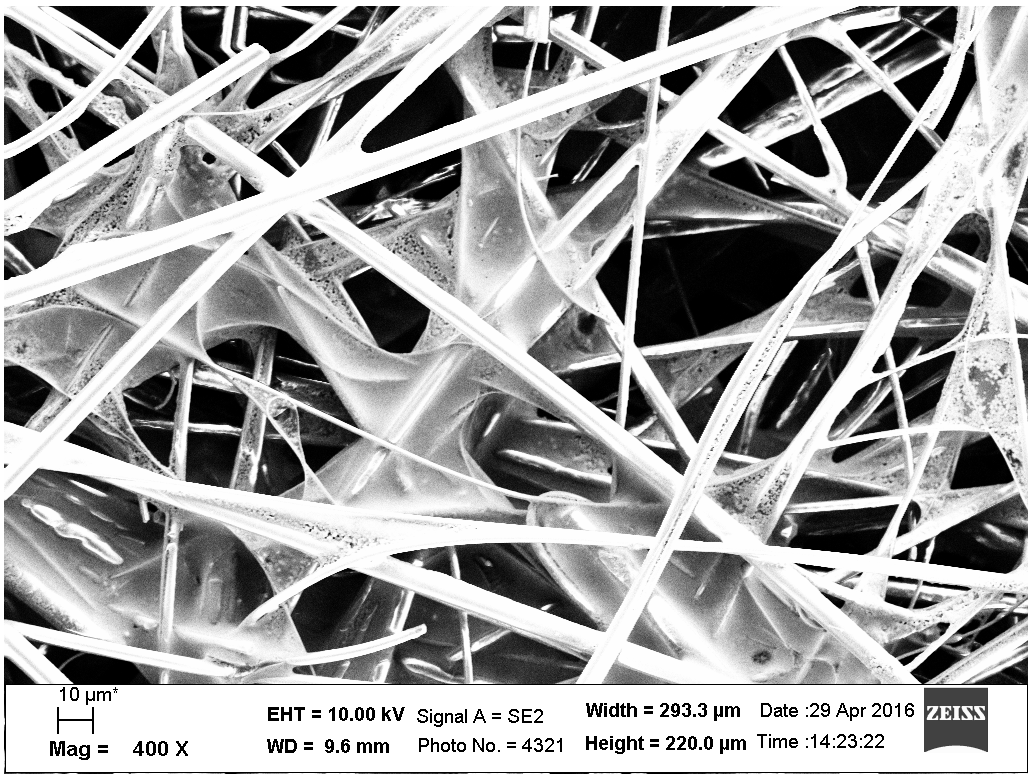
10 µm*
Mag = 400 X
EHT = 10.00 kV
WD = 9.6 mm
Signal A = SE2
Photo No. = 4321
Width = 293.3 µm
Height = 220.0 µm
Date :29 Apr 2016
Time :14:23:22
ZEISS

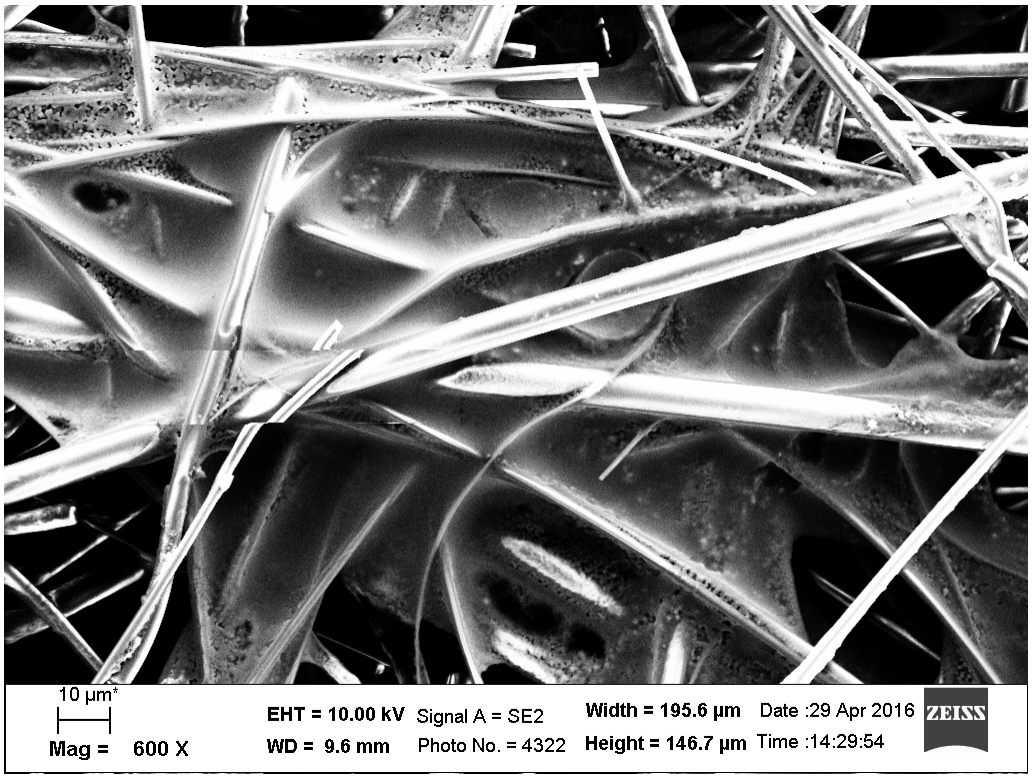
10 µm*
Mag = 600 X
EHT = 10.00 kV
WD = 9.6 mm
Signal A = SE2
Photo No. = 4322
Width = 195.6 µm
Height = 146.7 µm
Date :29 Apr 2016
Time :14:29:54
ZEISS

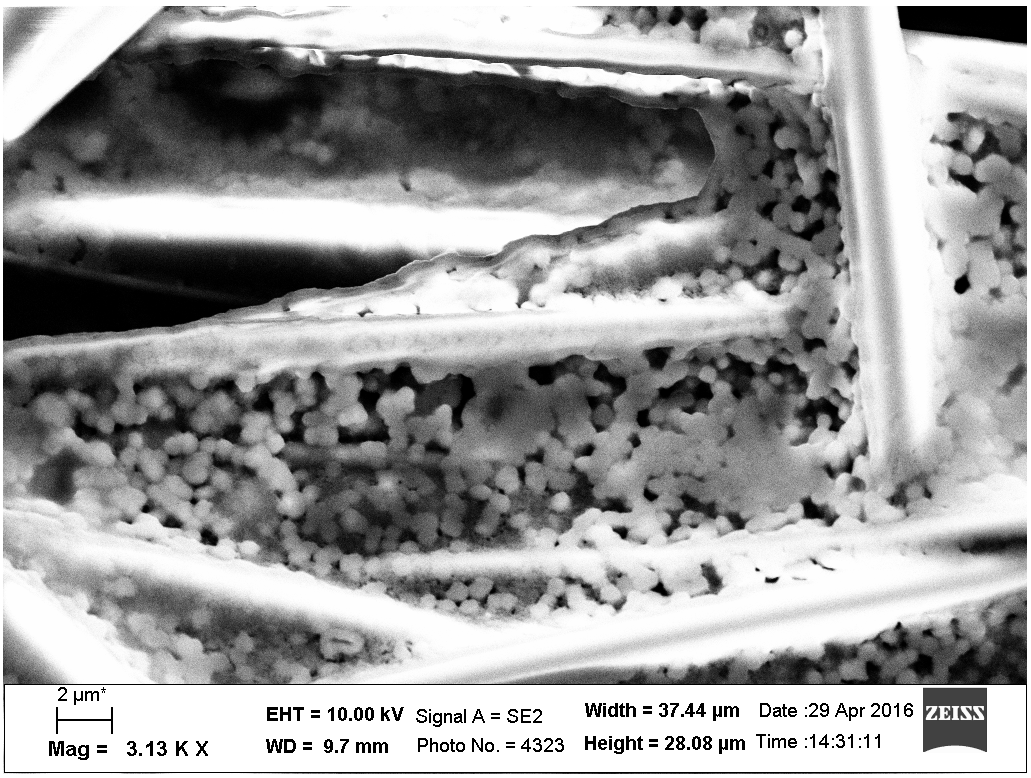
2 µm*
Mag = 3.13 K X
EHT = 10.00 kV
WD = 9.7 mm
Signal A = SE2
Photo No. = 4323
Width = 37.44 µm
Height = 28.08 µm
Date :29 Apr 2016
Time :14:31:11
ZEISS

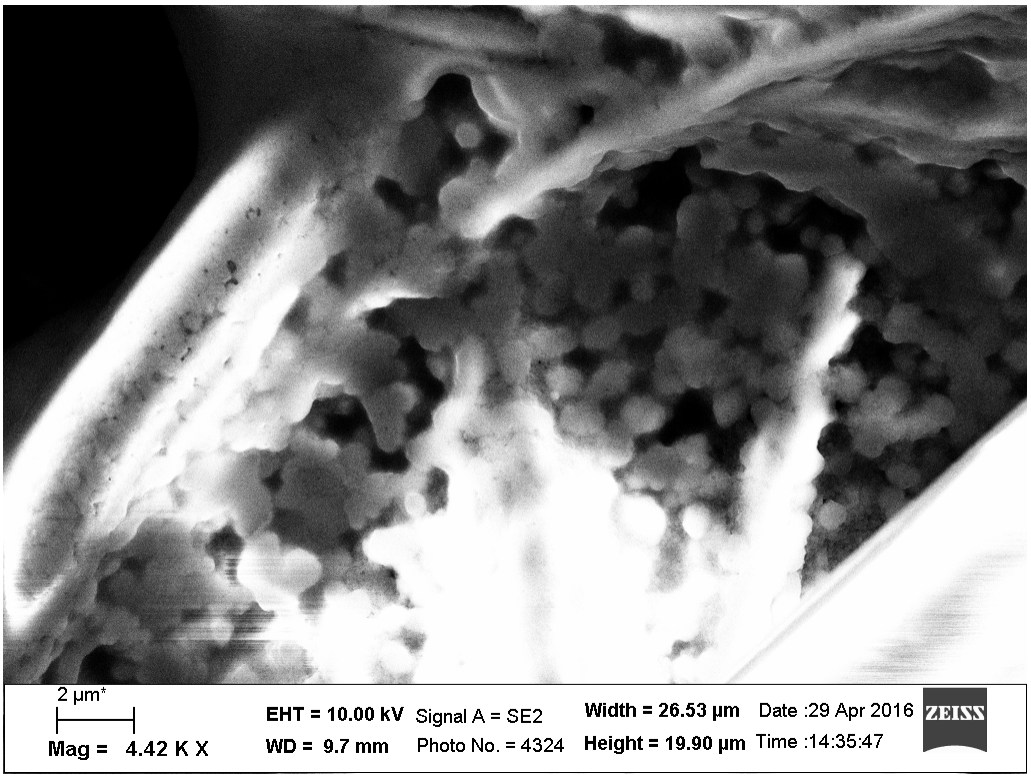
2 µm*
Mag = 4.42 K X
EHT = 10.00 kV
WD = 9.7 mm
Signal A = SE2
Photo No. = 4324
Width = 26.53 µm
Height = 19.90 µm
Date :29 Apr 2016
Time :14:35:47
ZEISS

6. References

(1) Morens, D. M.; Folkers, G. K.; Fauci, A. S. **2004**, *430* (July).

(2) Gubala, V.; Harris, L. F.; Ricco, A. J.; Tan, M. X.; Williams, D. E. *Anal. Chem.* **2012**, *84* (2), 487–515.

(3) Yager, P.; Domingo, G. J.; Gerdes, J. *Annu. Rev. Biomed. Eng.* **2008**, *10*, 107–144.

(4) Schubert-Ullrich, P.; Rudolf, J.; Ansari, P.; Galler, B.; Führer, M.; Molinelli, A.; Baumgartner, S. *Anal. Bioanal. Chem.* **2009**, *395* (1), 69–81.

(5) Land, J. A.; Van Bergen, J. E. A. M.; Morre, S. A.; Postma, M. J. *Hum. Reprod. Update* **2009**, *16* (2), 189–204.

(6) Aslan, K.; Lakowicz, J. R.; Geddes, C. D. *Anal. Biochem.* **2004**, *330* (1), 145–155.

(7) Elghanian, R.; Storhoff, J. J.; Mucic, R. C.; Letsinger, R. L.; Mirkin, C. a. *Science* **1997**, *277* (5329), 1078–1081.

(8) Sayed, I.; Huang, X.; El-Sayed, M. *Nano Lett.* **2005**, *5* (5), 829–834.

(9) Turkevich, J.; Stevenson, P. C.; Hillier, J. *Discuss. Faraday Soc.* **1951**, *11* (c), 55–75.

(10) Frens, G. *Kolloid-Zeitschrift Zeitschrift f??r Polym.* **1972**, *250* (7), 736–741.

(11) Brust, M.; Walker, M.; Bethell, D.; Schiffrin, D. J.; Whyman, R. **2000**, 801–802.

(12) Giersig, M.; Mulvaney, P. *Langmuir* **1993**, *9* (12), 3408–3413.

(13) Templeton, A. C.; Wuelfing, M. P.; Murray, R. W. **2000**, 27–36.

(14) Nakamura, K.; Kawabata, T.; Mori, Y. *Powder Technol.* **2003**, *131* (2-3), 120–128.

(15) Haiss, W.; Thanh, N. T. K.; Aveyard, J.; Fernig, D. G. **2007**, *79* (13), 4215–4221.

(16) Jans, H.; Liu, X.; Austin, L.; Maes, G.; Huo, Q. *Anal. Chem.* **2009**, *81* (22), 9425–9432.

(17) Jue, E.; Yamanishi, C. D.; Chiu, R. Y. T.; Wu, B. M.; Kamei, D. T. *Biotechnol. Bioeng.* **2014**, *111* (12), 2499–2507.

(18) Mashayekhi, F.; Meyer, A. S.; Shiigi, S. A.; Nguyen, V.; Kamei, D. T. *Biotechnol. Bioeng.* **2009**, *102* (6), 1613–1623.

(19) Mashayekhi, F.; Le, A. M.; Nafisi, P. M.; Wu, B. M.; Kamei, D. T. *Anal. Bioanal. Chem.* **2012**, *404* (6-7), 2057–2066.

(20) Chiu, R. Y. T.; Nguyen, P. T.; Wang, J.; Jue, E.; Wu, B. M.; Kamei, D. T. *Ann. Biomed. Eng.* **2014**, *42* (11), 2322–2332.

(21) Chiu, R. Y. T.; Jue, E.; Yip, A. T.; Berg, A. R.; Wang, S. J.; Kivnick, A. R.; Nguyen, P. T.; Kamei, D. T. *Lab Chip* **2014**, *14* (16), 3021–3028.

(22) Pereira, D. Y.; Chiu, R. Y. T.; Zhang, S. C. L.; Wu, B. M.; Kamei, D. T. *Anal.*

Chim. Acta **2015**, *882*, 83–89.

(23) Hatti-kaul, R. **2001**, *19*.

(24) Asenjo, J. a.; Andrews, B. a. *J. Chromatogr. A* **2012**, *1238* (September 2011), 1–10.

(25) Asenjo, J. a.; Andrews, B. a. *J. Chromatogr. A* **2011**, *1218* (49), 8826–8835.

(26) Diamond, a D.; Hsu, J. T. *Biotechnol. Bioeng.* **1989**, *34* (7), 1000–1014.

(27) Johansson, H. O.; Karlström, G.; Tjerneld, F.; Haynes, C. a. *J. Chromatogr. B. Biomed. Sci. Appl.* **1998**, *711* (1-2), 3–17.

(28) Berthod, a.; Carda-Broch, S. *J. Chromatogr. A* **2004**, *1037* (1-2), 3–14.

(29) Ananthapadmanabhan, K. P.; Goddard, E. D. *Langmuir* **1987**, *3* (1), 25–31.

(30) Walter, H.; Johansson, G. *Methods in Enzymology: Aqueous Two-Phase Systems*; Elsevier, 1994.

(31) Wong, R.; Tse, H. *Lateral Flow Immunoassay*, 1st ed.; Springer: New York, 2009.

(32) Macfarlane, I.; Davis, F. *IVD Technol.* **2002**, No. 27.

(33) Roxas-Duncan, V. I.; Leonard, A. S. *J Bioterr Biodef S* **2012**, *7* (2).

(34) Yoon, J. Y.; Kim, B. *Sensors (Switzerland)* **2012**, *12* (8), 10713–10741.

(35) Then, W. L.; Garnier, G. *Rev. Anal. Chem.* **2013**, *32* (4), 269–294.

(36) Fu, E.; Kauffman, P.; Lutz, B.; Yager, P. *Sensors Actuators, B Chem.* **2010**, *149* (1), 325–328.

(37) Fu, E.; Lutz, B.; Kauffman, P.; Yager, P. *Lab Chip* **2010**, *10* (7), 918–920.

(38) Osborn, J. L.; Lutz, B.; Fu, E.; Kauffman, P.; Stevens, D. Y.; Yager, P. *Lab Chip* **2010**, *10* (20), 2659–2665.

(39) Fu, E.; Ramsey, S. a.; Kauffman, P.; Lutz, B.; Yager, P. *Microfluid. Nanofluidics* **2011**, *10* (1), 29–35.

(40) Kauffman, P.; Fu, E.; Lutz, B.; Yager, P. *Lab Chip* **2010**, *10* (19), 2614–2617.

(41) Lutz, B. R.; Trinh, P.; Ball, C.; Fu, E.; Yager, P. *Lab Chip* **2011**, *11* (24), 4274.

(42) Fridley, G. E.; Le, H. Q.; Fu, E.; Yager, P. *Lab Chip* **2012**, *12* (21), 4321.

(43) Fu, E.; Liang, T.; Spicar-Mihalic, P.; Houghtaling, J.; Ramachandran, S.; Yager, P. *Anal. Chem.* **2012**, *84* (10), 4574–4579.

(44) Lutz, B.; Liang, T.; Fu, E.; Ramachandran, S.; Kauffman, P.; Yager, P. *Lab Chip* **2013**, *13* (14), 2840–2847.

(45) Mosadegh, B.; Lockett, M. R.; Minn, K. T.; Simon, K. a.; Gilbert, K.; Hillier, S.; Newsome, D.; Li, H.; Hall, A. B.; Boucher, D. M.; Eustace, B. K.; Whitesides, G. M. *Biomaterials* **2015**, *52*, 262–271.

(46) Thuo, M. M.; Martinez, R. V.; Lan, W. J.; Liu, X.; Barber, J.; Atkinson, M. B. J.; Bandarage, D.; Bloch, J. F.; Whitesides, G. M. *Chem. Mater.* **2014**, *26* (14), 4230–4237.

(47) Kumar, A. a.; Hennek, J. W.; Smith, B. S.; Kumar, S.; Beattie, P.; Jain, S.; Rolland, J. P.; Stossel, T. P.; Chunda-Liyoka, C.; Whitesides, G. M. *Angew. Chemie Int. Ed.* **2015**, n/a – n/a.

(48) Lan, W.; Zou, X. U.; Hamedi, M. M.; Hu, J.; Parolo, C.; Maxwell, E. J.; Bu, P.; Whitesides, G. M. *Anal. Chem.* **2014**, *86*, 9548–9553.

(49) Badu-Tawiah, A. K.; Lathwal, S.; Kaastrup, K.; Al-Sayah, M.; Christodouleas, D. C.; Smith, B. S.; Whitesides, G. M.; Sikes, H. D. *Lab Chip* **2014**, *15*, 655–659.

(50) Mashayekhi, F.; Chiu, R. Y. T.; Le, A. M.; Chao, F. C.; Wu, B. M.; Kamei, D. T. *Anal. Bioanal. Chem.* **2010**, *398* (7-8), 2955–2961.

(51) Myszka, D. G.; Morton, T. A. *Methods Enzymol.* **1998**, *295*, 268–294.

(52) Schuck, P. *Curr. Opin. Biotechnol.* **1997**, *8* (4), 498–502.

(53) Shang, J.; Gao, X. *Chem. Soc. Rev.* **2014**, *43*, 7267–7278.

(54) Jang, H.; Ryoo, S. R.; Kostarelos, K.; Han, S. W.; Min, D. H. *Biomaterials* **2013**, *34* (13), 3503–3510.

(55) Zeng, N.; Li, Y.; Du, M. **2015**, 46–50.

(56) Qian, S.; Bau, H. H. *Anal. Biochem.* **2003**, *322* (1), 89–98.

(57) Qian, S.; Bau, H. H. *Anal. Biochem.* **2004**, *326* (2), 211–224.

(58) Zeng, N.; Wang, Z.; Li, Y.; Du, M.; Liu, X. **2012**, *9* (2), 321–329.

(59) Zeng, N.; Wang, Z.; Li, Y.; Du, M.; Liu, X. *IEEE Trans. Nanotechnol.* **2012**, *11* (2), 321–327.

(60) Nianyin Zeng; Zidong Wang; Yurong Li; Min Du; Xiaohui Liu. *IEEE Trans. Biomed. Eng.* **2011**, *58* (7), 1959–1966.

(61) Hafner, L. M. *Contraception* **2015**, *92* (2), 108–115.

(62) Centers for Disease Control and Prevention. **2014**, No. December, 1–176.

(63) Krupp, K.; Madhivanan, P. *Indian J. Sex. Transm. Dis.* **2015**, *36* (1), 3–8.

(64) Huang, W.; Gaydos, C.; Barnes, M.; Jett-Goheen, M.; Blake, D. R. *Sex Transm Infect* **2013**, *89*, 108–114.

(65) Miller, W. C. *Sex. Transm. Infect.* **1998**, *25* (4), 201–211.

(66) Mahilum-Tapay, L.; Laitila, V.; Wawrzyniak, J. J.; Lee, H. H.; Alexander, S.; Ison, C.; Swain, A.; Barber, P.; Ushiro-Lumb, I.; Goh, B. T. *BMJ* **2007**, *335* (7631), 1190–1194.

(67) Low, N.; Broutet, N.; Adu-Sarkodie, Y.; Barton, P.; Hossain, M.; Hawkes, S. *Lancet* **2006**, *368* (9551), 2001–2016.

(68) Coo, L. **2004**.

(69) Peter N. Njoki; I-Im S. Lim; Derrick Mott; Park, H.-Y.; Bilal Khan; Suprav Mishra; Ravishanker Sujakumar; Jin Luo, A.; Zhong, C.-J. **2007**, *111*, 14664–14669.

(70) Wooding, R. A.; Morel-Seytoux, H. J. *Annu. Rev. Fluid Mech.* **1976**, *8*, 233–274.